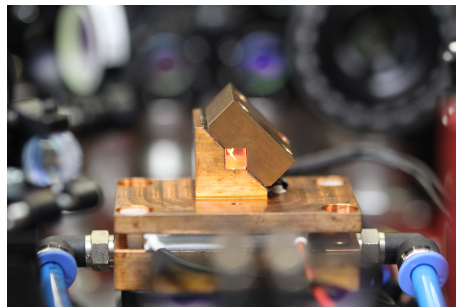


# Compact and efficient sub-10 ps pump sources at $2\ \mu\text{m}$ for the generation of coherent mid-infrared radiation



Von der Fakultät für Mathematik und Physik  
der Gottfried Wilhelm Leibniz Universität Hannover  
zur Erlangung des akademischen Grades

DOKTOR DER NATURWISSENSCHAFTEN  
– **Dr. rer. nat.** –

genehmigte Dissertation von

**M.Sc. Moritz Hinkelmann**  
geboren am 07.11.1990 in Lübeck

2020

Referent: Prof. Dr. Uwe Morgner  
Korreferenten: Prof. Dr. Detlev Ristau  
Prof. Dr. Ömer Ilday  
Tag der Promotion: 19.12.2019

## Kurzfassung

Moritz Hinkelmann

### Kompakte und effiziente sub-10 ps Pumpquelle bei 2 $\mu\text{m}$ für die kohärente Erzeugung mittlerer Infrarotstrahlung

Ultrakurzpuls-Lasersysteme im Spektralbereich um 2  $\mu\text{m}$  mit hohen Pulsenergien sind leistungsfähige Treiber für eine Vielzahl von verschiedenen Anwendungen in der Industrie, Medizin und den Fundamentalwissenschaften. Die Realisierung solcher Laserquellen bleibt herausfordernd und beruht üblicherweise auf der Verstärkung zeitlich gestreckter Pulse (CPA, engl. chirped-pulse amplification) in regenerativen Verstärkern. In dieser Arbeit wurde ein vereinfachtes Konzept verfolgt, welches auf CPA-freien Verstärkern mit Mehrfachdurchgang bei Raumtemperatur beruht. Es wird gezeigt, dass in Holmium-dotierten Kristallen optische Pulse mit Pulsdauern unterhalb von 10 ps bis zu Pulsenergien im mJ-Bereich verstärkt werden können, wobei nichtlineare Effekte vermieden werden. Das Lasersystem besteht aus einem faserbasierten und modengekoppelten Ultrakurzpuls-Oszillator mit nachgeschaltetem Leistungsverstärker, welche jeweils auf Holmium-dotierter Glasfaser basieren. Die Strahlung wurde spektral maßgeschneidert, um nachgeschaltete Verstärker auf Basis von Ho:YLF Kristallen effizient seeden zu können. In einem Verstärkerkonzept mit Kristall-Mehrfachdurchgang wurden die Seedpulse des Faseroszillators von wenigen nJ bis auf 100  $\mu\text{J}$  bei einer Pulswiederholrate von 50 kHz verstärkt. Die maximale Pulsenergie war einzig durch die Zerstörschwelle des Lasermaterials limitiert. Weitere Energieskalierung bis auf 1.2 mJ bei 1 kHz konnte in einer finalen Stufe mit Einfachdurchgang realisiert werden. Die Gesamtverstärkung in den Ho:YLF Kristallen summiert sich somit auf  $> 51$  dB. Unter Berücksichtigung der gemessenen Pulsdauer von 8.3 ps ergibt sich eine Pulsspitzenleistung von 136 MW. Diese Ergebnisse wurden von numerischen Simulationen unterstützt, welche auf einem modifizierten Frantz-Nodvik-Formalismus beruhen. Diese ermöglichen es, sowohl chromatische Effekte als auch eine detaillierte Beschreibung der Pulsenergiezunahme zu untersuchen. Bis zu 50  $\mu\text{J}$  bei 100 kHz des Verstärkersystems wurden genutzt, um eine Tandem-Konfiguration bestehend aus optisch parametrischem Generator und Verstärker zu pumpen. Zum Einsatz kamen hoch nichtlineare Nicht-oxid-Kristalle mit der chemischen Bezeichnung  $\text{ZnGeP}_2$ . Die Phasenanpassung wurde so gewählt, dass die Zentralwellenlängen für die Signal- und Idlerwelle bei 3  $\mu\text{m}$  und 6.5  $\mu\text{m}$  liegen. Eine maximale Signal- und Idlerwellen-Pulsenergie von 7.7  $\mu\text{J}$  und 2.5  $\mu\text{J}$  wurde erreicht. In Anbetracht einer gemessenen Pulsdauer von jeweils etwa 4 ps konnten Spitzenleistungen von 2 MW (Signal) und 0.5 MW (Idlerwelle) erzielt werden. Die im mittleren Infrarot kohärent emittierende Strahlquelle kann hinsichtlich der Wellenlänge im Bereich zwischen 2.5  $\mu\text{m}$  und 8  $\mu\text{m}$  entsprechend der Phasenanpassung betrieben werden und weist eine Langzeit-Leistungsstabilität von weniger als 1.25 %rms im Niederfrequenzbereich auf.

**Schlagwörter:** Laserverstärker, Faserlaser, Festkörperlaser, Ultrakurzpuls laser, modengekoppelte Laser, optisch parametrische Erzeugung, optisch parametrische Verstärkung

## Abstract

Moritz Hinkelmann

### Compact and efficient sub-10 ps pump sources at 2 $\mu\text{m}$ for the generation of coherent mid-infrared radiation

Ultrashort pulse laser systems in the 2  $\mu\text{m}$  wavelength region featuring high pulse energies are powerful tools for driving a multitude of different applications in industry, medicine, and fundamental science. The implementation of such laser sources remains challenging and usually relies on the chirped-pulse amplification (CPA) in regenerative amplifiers. Here, a much more simplified concept based on a CPA-free multipass amplification scheme operating at room temperature has been investigated. I show that optical pulses with moderate sub-10 ps duration can be amplified up to the millijoule energy level without the onset of nonlinear effects in holmium-doped crystals. The laser system consists of an ultrafast all-fiber mode-locked oscillator and power amplifier based on holmium-doped silica fiber. It has been spectrally tailored to efficiently seed subsequent amplifiers based on holmium-doped YLiF<sub>4</sub> crystals. A multipass amplification concept was used to amplify the nJ-level seed pulses from the fiber front-end up to 100  $\mu\text{J}$  of pulse energy at a pulse repetition frequency of 50 kHz. The maximum pulse energy was limited only by the laser-induced damage threshold of the amplifier crystals. Further pulse energy scaling has been achieved in a final single-pass booster amplifier generating 1.2 mJ at 1 kHz. The overall gain in the Ho:YLF crystals amount to  $> 51$  dB. Taking into account a measured pulse duration of 8.3 ps, this yields a pulse peak power of 136 MW. These results have been supported by numerical simulations based on a modified Frantz-Nodvik formalism, which is capable of modeling chromatic effects as well as a detailed description of the energy built-up in such amplifiers. Up to 50  $\mu\text{J}$  at 100 kHz from the multipass amplifier have been used to pump an optical parametric generator/amplifier tandem configuration based on the highly nonlinear non-oxide crystal ZnGeP<sub>2</sub>. The phase-matching condition has been set to achieve a signal and idler center wavelength of 3  $\mu\text{m}$  and 6.5  $\mu\text{m}$ , respectively. The maximum signal and idler pulse energy was 7.7  $\mu\text{J}$  and 2.5  $\mu\text{J}$ . Considering a measured pulse duration of 4 ps for both wavelengths, a peak intensity of about 2 MW (signal) and 0.5 MW (idler) was reached. The mid-IR coherent source is wavelength tunable covering the spectral range from 2.5  $\mu\text{m}$  to 8  $\mu\text{m}$  under appropriate phase-matching conditions and has shown long-term stability of less than 1.25 %rms low-frequency power noise.

**Key words:** laser amplifiers, fiber lasers, ultrafast lasers, mode-locked lasers, optical parametric generation, optical parametric amplification



---

## Contents

---

<b>1</b>	<b>Introduction</b>	<b>1</b>
<b>2</b>	<b>State of the art</b>	<b>5</b>
2.1	Intense ultrashort pulse lasers with emission around 2 $\mu\text{m}$ . . . . .	5
2.2	Mid-wave infrared generation in optical parametric conversion stages . . . . .	6
<b>3</b>	<b>All-fiber ultrashort pulse laser source with emission at 2 <math>\mu\text{m}</math></b>	<b>9</b>
3.1	Fundamentals of pulse propagation in fibers . . . . .	9
3.1.1	Chromatic dispersion . . . . .	9
3.1.2	Fiber nonlinearities . . . . .	11
3.1.3	Pulse propagation equation . . . . .	13
3.2	Generation of ultrashort pulses in fiber lasers . . . . .	14
3.2.1	Pulse regimes in fiber lasers . . . . .	14
3.2.2	Passive mode-locking techniques . . . . .	16
3.3	Properties of holmium-doped fibers . . . . .	17
3.4	All-fiber mode-locked oscillator . . . . .	19
3.5	Fiber-based pre-amplifier . . . . .	23
3.6	Summary and outlook . . . . .	27
<b>4</b>	<b>CPA-free amplification based on holmium-doped crystals</b>	<b>29</b>
4.1	CPA-free amplification schemes for ultrashort pulses . . . . .	29
4.2	Numerical simulation model for pulse amplification . . . . .	30
4.3	Properties of holmium-doped crystals . . . . .	33
4.4	CPA-free multipass amplification in Ho:YLF . . . . .	43
4.5	High-energy booster amplifier based on Ho:YLF . . . . .	49
4.6	Summary and outlook . . . . .	54
<b>5</b>	<b>Optical parametric conversion for mid-IR pulse generation</b>	<b>57</b>
5.1	Theory of optical parametric generation and amplification . . . . .	57
5.2	Properties of nonlinear crystals for mid-IR coherent sources . . . . .	64
5.3	Mid-IR generation via OPG . . . . .	66
5.4	High conversion efficiency mid-IR OPA . . . . .	70
5.5	Summary and outlook . . . . .	75
<b>6</b>	<b>Conclusion</b>	<b>77</b>
<b>7</b>	<b>Outlook</b>	<b>81</b>

<b>Bibliography</b>	<b>83</b>
<b>Appendix</b>	<b>111</b>
<b>A Numerical model for the fiber-based MOPA</b>	<b>111</b>
<b>B Nonlinear optical crystals for mid-infrared coherent sources</b>	<b>113</b>
<b>C Thulium-fiber MOPA-based pump source</b>	<b>117</b>
<b>Publications</b>	<b>119</b>
<b>Curriculum Vitae</b>	<b>121</b>

## Acronyms

---

<b>Notation</b>	<b>Description</b>
AGS	silver gallium sulfide
AGSe	silver gallium selenide
AOM	acousto-optic modulator
CPA	chirped-pulse amplification
CSP	cadmium silicon phosphide
DFG	difference-frequency generation
FOM	figure of merit
FWHM	full-width at half-maximum
GaSe	gallium selenide
GVD	group-velocity dispersion
Ho	holmium
Ho:YAG	holmium-doped $Y_3Al_5O_{12}$
Ho:YLF	holmium-doped $YLiF_4$
IR	infrared
LIDT	laser-induced damage threshold
LMA	large mode area
LuO	lutetium oxide
LWIR	long-wave infrared
MOPA	master oscillator power amplifier
MWIR	mid-wave infrared
NA	numerical aperture
NDF	normal dispersion fiber
NLSE	nonlinear Schrödinger equation
NPR	nonlinear polarization rotation
OP-GaAs	orientation-patterned gallium arsenide

---

---

<b>Notation</b>	<b>Description</b>
OP-GaP	orientation-patterned gallium phosphide
OPA	optical parametric amplification
OPCPA	optical parametric chirped-pulse amplification
OPG	optical parametric generation
OPO	optical parametric oscillator
PM	polarization maintaining
PPKTA	periodically poled potassium arsenate
PPKTP	periodically poled potassium triphosphate
PPLN	periodically poled lithium niobate
QPM	quasi-phase-matching
RA	regenerative amplifier
RIN	relative intensity noise
rms	root mean square
SESAM	semiconductor saturable absorber mirror
SFG	sum-frequency generation
SHG	second-harmonic generation
SPM	self-phase modulation
SWIR	short-wave infrared
Tm	thulium
TOD	third-order dispersion
UHNA	ultra-high numerical aperture
WDM	wavelength division multiplexer
XPM	cross-phase modulation
YAG	yttrium aluminum garnet
Yb	ytterbium

---

---

<b>Notation</b>	<b>Description</b>
YLF	yttrium lithium fluoride
YVO	yttrium orthovanadate
ZGP	zinc germanium phosphide

---



# CHAPTER 1

## Introduction

Since its first demonstration in 1960 by MAIMAN [Mai60], light amplification by stimulated emission of radiation (laser) has evolved into one of the key technologies of the last and current century. Nowadays, laser systems are indispensable in wide fields of industry, medicine, and science as they enable a huge bandwidth of applications. Many of these applications require ultrashort laser pulses, which can provide intense radiation. Today, ultrashort pulse laser systems, which typically operate in the visible to near-infrared (IR) wavelength region, are well-developed and readily available. However, there has been a strong application-driven demand for ultrashort pulse lasers with emission in the mid-IR spectrum shifting the research efforts towards the wavelength range spanning from 2 up to 8  $\mu\text{m}$  and beyond (see Figure 1.1). The development of such systems has the potential to improve established technology or even enable a variety of applications which cannot be addressed by the conventional visible to near-IR laser sources.

The mid-IR hosts a multitude of characteristic rotational and vibrational transitions of molecules. On the one hand, there are numerous applications based on linear absorption such as medical diagnostics [Pet11], minimally invasive neurosurgery [Edw03; Joo00], and

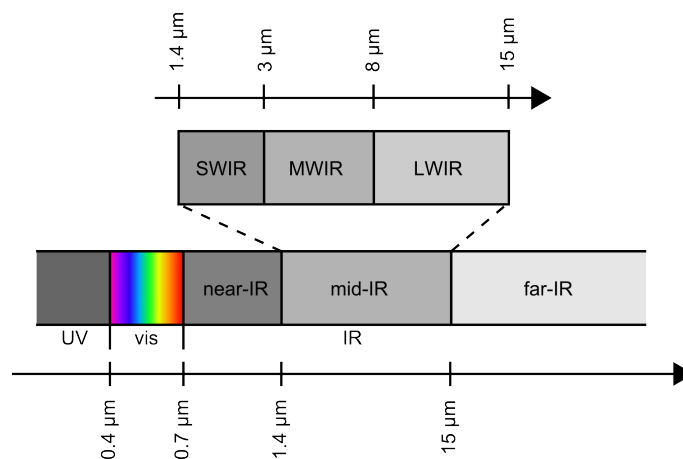


**Figure 1.1:** Part of the electromagnetic spectrum ranging from the ultraviolet (UV) to the infrared (IR) radiation. Nowadays, conventional laser sources emitting in the visible to near-IR spectral region are more and more replaced by mid-IR laser sources. The short-wave infrared (SWIR) and, especially, the mid-wave (MWIR) and long-wave infrared (LWIR) radiation is interesting for a multitude of recently emerging applications.

the detection of biologically hazardous or explosive materials. Since the mid-IR radiation is considered to be eye-safe [Sch10], spectroscopic applications can be applied even via long-range free-space detection like atmospheric metrology [Kad11; Tit03]. On the other hand, laser sources with intense radiation are required to drive nonlinear spectroscopy methods like vibrational sum-frequency generation spectroscopy [Ric02] or multi-dimensional infrared spectroscopy [Gar09; Zan01]. In the wide field of industrial applications, the mid-IR laser sources can be used to directly process polymers due to the increased absorption in comparison to near-IR laser irradiation [Min12; Sch10]. Taking advantage of their transparency range at  $2\ \mu\text{m}$ , trans-wafer processing [Geh14; Min16] or even in-volume semiconductor material processing [Hur07] can be realized with ultrashort pulse lasers. In addition, selective micromachining of organic solar cells becomes very efficient due to distinct absorption features in the vicinity of  $3\ \mu\text{m}$  [Nai14; Nai13]. Fundamental science applications in strong-field experiments demand for even more pretentious laser characteristics: Femtosecond laser sources with sufficiently high peak power are able to drive high-harmonic generation on a gaseous target. As the high-order harmonic cutoff energy scales with the driving wavelength [Sha01], coherent mid-IR sources provide access to the high-energy X-ray radiation [Pop12].

The short-wave infrared (SWIR) spectral region is traditionally accessed by nonlinear frequency conversion stages based on commercial near-IR pump laser systems. Even longer wavelengths in the mid-wave infrared (MWIR) or long-wave infrared (LWIR) are in turn accessible via cascaded schemes, which use intermediate wavelengths in the SWIR to pump final frequency down-conversion stages. The latter are commonly based on optical parametric conversion in non-oxide crystals such as orientation-patterned gallium arsenide (OP-GaAs) or zinc germanium phosphide (ZGP) [Sch16]. These crystals require pump sources with an emission wavelength of  $> 1.9\ \mu\text{m}$  in order to approach their transparency window reaching far into the mid-IR and considerably intense pulses for efficiently driving the nonlinear frequency conversion process. However, the overall optical-to-optical efficiency of cascaded nonlinear frequency conversion is rather low. In addition, the complexity and footprint is comparably high increasing the cost and maintenance.

An alternative approach for the generation of intense radiation suitable to pump these highly nonlinear non-oxide crystals is the direct emission in fibers and crystals doped with thulium (Tm) or holmium (Ho). The gain bandwidth of Tm- and Ho-doped fibers is sufficient to generate pulses with a duration of less than 100 fs. In terms of high pulse energy levels, the amplification in Tm- and Ho-doped crystals has resulted in hundreds of  $\mu\text{J}$  or even mJ pulse energy maintaining excellent beam quality and sub-ps pulse duration. However, the emission in Tm-doped materials in the vicinity around  $1.9\ \mu\text{m}$  is strongly affected by atmospheric absorption of the molecular water content [Geb15b]. In contrast, Ho-based laser systems remain nearly unaffected as they exhibit longer emission wavelengths depending on the host lattice between 2 and  $2.2\ \mu\text{m}$ . In addition, Ho-doped crystals offer comparably higher emission cross sections [Wal98], which is beneficial for the efficient generation of high-energy laser pulses [Wie16].



---

So far, sub-10 ps pulses with energies up to the mJ-level have been generated by the chirped-pulse amplification (CPA) scheme only. The most widespread concept is an ultrashort pulse generation at 2  $\mu\text{m}$  by nonlinear frequency conversion stages (e.g. difference-frequency generation (DFG) in combination with optical parametric amplification (OPA) or supercontinuum generation) pumped with near-IR ultrashort pulses and the amplification in regenerative amplifiers (RAs). However, the latter are mainly driven by high-voltage Pockels cells, which are usually limited to pulse repetition frequencies  $\leq 10$  kHz. In combination with the CPA scheme they are increasingly complex requiring the precise alignment of expensive grating-based stretchers and compressors. In contrast, CPA-free multipass amplifier systems based on Ho-doped materials can pave the way to cost effective industrial applications as they are less space consuming, highly efficient, and easy to align.

The aim of this thesis was therefore to develop fiber-based ultrashort pulse oscillators with direct emission at 2  $\mu\text{m}$  in combination with CPA-free amplifiers based on Ho-doped fibers and crystals. At the same time, pulse repetition rates of  $\geq 100$  kHz represent a unique feature, which is beneficial for enhancing the signal-to-noise ratio for spectroscopic measurements or increasing the processing speed in the case of industrial applications. In a second step, an optical parametric conversion stage, which was pumped by the novel 2  $\mu\text{m}$  laser system, was developed and investigated to approach the deep mid-IR spectral range. For the first time, the direct generation of mJ-level pulses at 2  $\mu\text{m}$  in a compact and efficient CPA-free laser system was shown. In addition, the first MW-level laser with emission covering the full MWIR spectral region is presented, which is operating at high pulse repetition frequencies of 100 kHz maintaining a simplified nonlinear frequency down-conversion based on parametric processes.

The thesis is divided into the following chapters: Chapter 2 provides an overview of the state-of-the-art laser systems capable of generating intense laser pulses in the 2  $\mu\text{m}$  wavelength range. In particular, in this chapter the generation of sub-10 ps pulses with pulse energies up to the mJ-level in Ho-doped materials is described. In addition, the state-of-the-art mid-IR laser sources based on non-oxide nonlinear crystals pumped at  $> 1.9$   $\mu\text{m}$  are summarized. In Chapter 3 methods concerning the generation and amplification of ultrashort pulses based on Ho-doped fibers are presented. First, the fundamentals of pulse generation and propagation in optical waveguides are briefly introduced followed by the basic properties of Ho-doped silica fibers. An all-fiber laser system is described, which was used as seed for subsequent crystal-based amplifiers. Its spectral and temporal properties were investigated and tailored to efficiently seed holmium-doped  $\text{YLiF}_4$  (Ho:YLF) crystals for efficient high-power amplification. The CPA-free amplification in Ho:YLF crystals up to the mJ-level is presented in Chapter 4. Major challenges considering the CPA-free amplification of intense pulses are addressed by numerical simulations and experimental investigations. The general properties of Ho-doped crystals are given followed by the detailed description of the developed high-gain multipass and booster amplifiers. In order to extend the CPA-free scheme to subsequent parametric conversions stages, a tandem configuration consisting of an optical parametric generator and an optical parametric amplifier based on ZGP crystals was developed. The experimental results, which are presented in Chapter 5, are supported

by the theoretical background of parametric generation and amplification and a summary of the most important nonlinear optical materials with transparency in the mid-IR spectral region. Finally, Chapter 6 summarizes the results of this thesis, while Chapter 7 provides an outlook concerning potential scaling capabilities and further investigations to push this technology.

# CHAPTER 2

---

## State of the art

---

Within the last few years the development of high-energy, ultrashort pulse laser systems in the  $2\ \mu\text{m}$  spectral range simultaneously promoted progress in the field of MWIR coherent sources towards intense radiation via nonlinear frequency conversion processes. The following chapter addresses both domains separately, summarizing the state of the art.

### 2.1 Intense ultrashort pulse lasers with emission around $2\ \mu\text{m}$

The generation of ultrashort  $2\ \mu\text{m}$  laser pulses relies mainly on three different approaches: On the one hand, the well-developed near-IR laser sources based on titanium:sapphire or ytterbium (Yb)-doped fibers have been used to drive DFG/OPA schemes [Hon14; Liu19]. These systems offer broad spectral tunability to address manifold applications, which comes at the expense of a low overall efficiency due to the (cascaded) nonlinear frequency down-conversion mechanism. On the other hand, ultrafast laser sources emitting at the telecommunication wavelength around  $1.5\ \mu\text{m}$  have been converted towards the  $2\ \mu\text{m}$  spectral region by means of Raman-induced soliton self-frequency shift [Nis01; Sob18]. In contrast to these nonlinear concepts, the direct  $2\text{-}\mu\text{m}$  emission in Tm- and Ho-doped materials offers a comparably higher efficiency in a simplified laser architecture. To achieve ultrashort pulses with energies exceeding 1 mJ, chirped-pulse regenerative amplification schemes have been typically applied up to now.

In 2013, DERGACHEV [Der13] demonstrated first regenerative amplification with emission at  $2.05\ \mu\text{m}$  based on a Ho:YLF crystal. A pulse energy of 1.7 mJ at a pulse repetition frequency of 1 kHz was achieved. However, the pulse duration was rather long with 300 ps. The first femtosecond laser system with mJ-level pulse energy has been presented by MALEVICH et al. [Mal13] in the same year. An OPA-based front-end has been used to generate the broadband  $2\ \mu\text{m}$  seed, which was amplified in a holmium-doped  $\text{Y}_3\text{Al}_5\text{O}_{12}$  (Ho:YAG) RA utilizing a CPA scheme. After temporal compression, 530-fs pulses with pulse energies of about 1 mJ have been obtained. Highest pulse energy of about 10 mJ at kHz repetition rate directly from a CPA RA system based on Ho-doped crystals has been generated by GRAFENSTEIN et al. [Gra15]. In order to reach such high energies, the RA was operated in the bistable regime of the second operation point.

Alternatively, high pulse energies can be achieved by using single-pass or multipass amplification in Ho-doped crystals. In 2013, DERGACHEV [Der13] demonstrated a single-pass amplifier based on two 70 mm Ho:YLF crystals generating a pulse energy of 11 mJ with

comparably long pulse durations of 300 ps resulting in a peak power of 1 MW. Much higher pulse energies maintaining ultrashort pulse durations have been shown by HEMMER et al. [Hem15], who presented an 8-fold single-pass amplification in a 50 mm long 1 %-doped cryogenically cooled Ho:YLF crystal up to 39 mJ. The compressed pulse duration was 11 ps with an energy of about 33 mJ at 100 Hz. Just recently, KANAI et al. [Kan18] showed an updated system consisting of a triple-pass cryogenic Ho:YLF amplifier with up to 260 mJ. The pulses were compressible towards 19 ps at 200 mJ. It is worth noting that the aforementioned amplifier systems used a CPA-based RA front-end to seed the single-pass or multipass booster stages.

Much shorter pulses in the 2  $\mu\text{m}$  wavelength region have been achieved in Tm-doped fiber amplifiers, however, at the expense of a reduced pulse energy in the  $\mu\text{J}$  range. In 2017, GEBHARDT et al. [Geb17] published nonlinear pulse compression of a Tm-fiber chirped-pulse amplifier towards a pulse duration of 13 fs corresponding to 2.1 optical cycles. The average power was as high as 43 W with a pulse energy of 34.4  $\mu\text{J}$ . The intense ultrashort optical pulses with a peak power of 1.4 GW were limited by the pulse breakup. As the broadband emission centered at 1820 nm is prone to water vapor absorption, the high power section is restricted to its propagation in vacuum chambers, which resulted in rather complex and expensive architectures.

CPA-free amplification of 2- $\mu\text{m}$  ultrashort pulses up to the mJ-level pulse energy has not been shown so far. This very simplified amplification scheme has only been pursued by COLUCCELLI et al. [Col11] in 2011, who amplified the long wavelength tail of a supercontinuum comb source to about 16 nJ at a pulse duration of 508 fs. An average output power of 1.6 W has been achieved at 2053 nm with a 5-pass amplification scheme in a 50 mm long 0.8 %-doped Ho:YLF crystal.

## 2.2 Mid-wave infrared generation in optical parametric conversion stages

Within the last decade, there has been an application-driven demand to extend the accessible wavelength range even beyond 2  $\mu\text{m}$ . Only few laser systems exist, which exhibit direct emission in this MWIR or even LWIR, such as transition metal-doped chalcogenides [Mir18; Sor05; Vas19; Wan17], quantum cascade lasers [Kol12; Rau15], or CO<sub>2</sub> lasers [Toc12]. These mid-IR sources are limited in terms of the achievable pulse energy, ultrashort pulse duration, or broadband wavelength tunability. Hence, nonlinear frequency down-conversion is the predominant technique to expand the accessible laser frequency range with sufficient prospect of generating intense radiation. Typically, high-energy ultrashort pulse mid-IR systems with emission beyond 2  $\mu\text{m}$  can be roughly divided into two concepts: OPA/DFG schemes driven by titanium:sapphire or near-IR lasers and OPA or optical parametric chirped-pulse amplification (OPCPA) approaches exploiting 2  $\mu\text{m}$  pump sources.

Cascaded parametric frequency down-conversion via OPA and DFG processes driven by amplified titanium:sapphire laser systems or by DFG mixing between the outputs of two temporally synchronized near-IR lasers is well-established. Typically, the overall

conversion efficiency is rather low and the use of oxide crystals limits the achievable output wavelength to below  $5\ \mu\text{m}$ . The second approach exploits the non-oxide nonlinear crystals with their transparency windows reaching far into the mid-IR or even far-IR spectral region. Among these, ZGP is the most widespread material [Pet15], however,  $2\text{-}\mu\text{m}$  pump sources are required due to the transparency cut-off below this wavelength [Sch16] induced by two-photon absorption. The development of such long-wavelength sources has accelerated with the emergence of high-quality crystals just recently. However, it remains challenging and only a few systems have been reported worldwide.

A  $2\text{-}\mu\text{m}$ -pumped OPA based on ZGP has been shown in 2017 by KANAI et al. [Kan17] generating 100-fs pulses at a wavelength of  $5.2\ \mu\text{m}$ . A pulse energy of  $40\ \mu\text{J}$  at a pulse repetition frequency of 1 kHz was achieved. A  $2\ \mu\text{m}$  few-mJ femtosecond pump source based on several OPA stages has been used by KROGEN et al. [Kro16b] to achieve  $30\text{-}\mu\text{J}$  pulses at  $6.5\ \mu\text{m}$  with a duration of 30 fs. A similar pumping scheme is used by WANDEL et al. [Wan14] to generate  $50\ \mu\text{J}$  of pulse energy at a repetition rate of 10 Hz. The temporally compressed idler pulses with a duration of 450 fs were centered at a wavelength of  $5\ \mu\text{m}$ . First mid-IR OPCPA with GW-level peak powers at a wavelength of  $7\ \mu\text{m}$  has been presented by SANCHEZ et al. [San16], who achieved 0.55 mJ of pulse energy in a chain of three consecutive noncollinear ZGP-based stages. Temporal compression of the mid-IR pulses resulted in a duration of 180 fs with a pulse energy of  $200\ \mu\text{J}$  at 100 Hz repetition rate. In 2017, even higher pulse peak power of 7.7 GW has been shown by GRAFENSTEIN et al. [Gra17] at kHz pulse repetition rate. A three-stage ZGP-based OPCPA concept generated pulses, which were compressible towards a pulse duration of 75 fs maintaining mJ-level pulse energies around 1.3 mJ at a wavelength of  $5\ \mu\text{m}$ . Just recently, ELU et al. [Elu19] used the 100 Hz Ho:YLF-based laser source from [Kan18] to pump an OPCPA system to generate 0.7-mJ pulses at  $7\ \mu\text{m}$ . Only 10% of the available 200 mJ of pulse energy at  $2.05\ \mu\text{m}$  have been used so far, thus, further energy scaling can be expected towards the multi-mJ range.

However, the aforementioned mid-IR laser sources have in common that they rely on complex CPA architectures with pulse repetition frequencies limited to 1 kHz. Scaling the average output power by increasing the pulse repetition frequency is beneficial for many applications. In addition, several cascaded nonlinear stages are required to approach long wavelengths far beyond  $4\ \mu\text{m}$  or to generate picosecond pump pulses for OPA stages. This thesis provides a solution to these current limitations for the first time by introducing a simple and reliable laser source with direct emission at  $2\ \mu\text{m}$  capable of pumping nonlinear frequency-down conversion stages to access the wavelength range covering the full MWIR from 3 to  $8\ \mu\text{m}$ .



# CHAPTER 3

---

## All-fiber ultrashort pulse laser source with emission at 2 $\mu\text{m}$

---

This chapter covers the generation and amplification of ultrashort pulses in holmium-doped fibers in the 2  $\mu\text{m}$  wavelength region. First, the fundamentals of ultrashort pulse propagation in silica fibers are introduced in Section 3.1. Particularly, chromatic effects and fiber nonlinearities induced by broadband laser pulses will be described. These effects are also important to understand the pulse formation in fiber lasers. Section 3.2 addresses the different pulse regimes, which are important in the context of this thesis, and passive mode-locking techniques for the generation of ultrashort laser pulses. In Section 3.3 the general properties of holmium-doped fibers are summarized. A detailed description of the all-fiber Ho-based ultrashort pulse oscillator in Section 3.4 is followed by the corresponding fiber-amplifier in Section 3.5. The presented laser system has been spectrally and temporally tailored such that it can be used to efficiently seed CPA-free multipass amplifiers based on Ho:YLF crystals. Finally, Section 3.6 provides a summary and outlook of this chapter.

### 3.1 Fundamentals of pulse propagation in fibers

When an ultrashort pulse propagates through an optical fiber, it undergoes several linear and nonlinear effects. In particular, the focus of this chapter is set to the dispersive effects such as chromatic dispersion and fiber nonlinearities based on the intensity-dependent Kerr effect. The following introduction into fundamentals of laser pulse propagation through optical fibers will provide a brief overview in the context of this thesis. A more detailed description of the underlying physics can be found in textbooks such as [Agr12].

#### 3.1.1 Chromatic dispersion

When an optical pulse propagates through a transparent medium, the electromagnetic waves interact with the bound electrons. Generally, the response of the medium is dependent on the optical frequency  $\omega$ , which manifests itself through the frequency-dependent refractive index  $n(\omega)$ . This effect is called chromatic dispersion. In the context of ultrashort pulses, which naturally exhibit a broadband spectrum, the frequency components propagate with different velocities resulting in temporal pulse broadening, which is also denoted chirping. The impact of a linear chirp to an initially transform-limited pulse with its spatio-temporal distribution of the instantaneous frequency is shown in Figure 3.1. In this specific case the electric field is strongly up-chirped leading to a growing instantaneous frequency with time (Figure 3.1(b)). In order to characterize dispersive elements one can decompose the phase

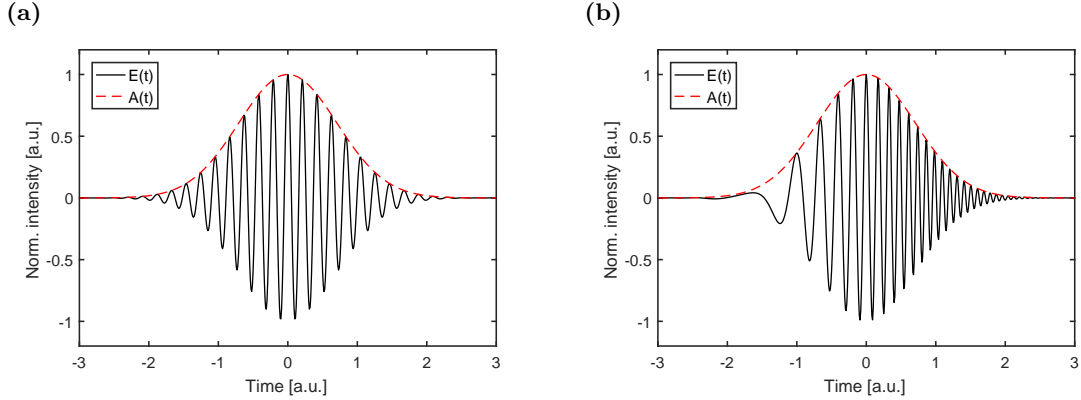


**Figure 3.1:** (a) Electrical field  $E(t)$  of an optical pulse with Gauss-shaped envelope  $A(t)$  based on Equation (3.7) and (b) linear up-chirp on an optical pulse, which manifests itself in a linear variation of the instantaneous frequency.

constant  $\beta(\omega)$  in a Taylor series around a center frequency  $\omega_0$ , which yields

$$\beta(\omega) = n(\omega) \frac{\omega}{c} = \sum_{j=0}^{\infty} \frac{\beta_j}{j!} (\omega - \omega_0)^j \quad (3.1)$$

with the coefficient

$$\beta_j = \left. \frac{d^j \beta}{d\omega^j} \right|_{(\omega=\omega_0)} \quad (j = 0, 1, 2, \dots). \quad (3.2)$$

$\beta_0$  describes a constant phase shift and  $\beta_1$  is the inverse group velocity representing a temporal shift of the pulse envelope. While these two coefficients do not contribute to a change of the pulse shape in time domain, all coefficients  $j \geq 2$  with  $\beta_j \neq 0$  contribute to a temporal pulse broadening. Typically, the second-order term has the highest impact. The phenomenon of pulse broadening due to  $\beta_2$  is called group-velocity dispersion (GVD) with  $\beta_2$  the GVD parameter, given in  $\text{s}^2/\text{m}$ . The impact of the third-order term  $\beta_3$  is called third-order dispersion (TOD). For pulse durations of more than 100 fs and when  $\beta_2 \neq 0$ , TOD and higher orders can be neglected.

In every optical waveguide, including standard step-index single-mode optical fibers, the chromatic dispersion is a superposition of the material and waveguide dispersion. This is shown in Figure 3.2(a) for a standard passive fiber of type SMF-28e+. The material dispersion only depends on the properties of the transparent medium, whereas the waveguide dispersion is a consequence of a deviation from a plane wave assumption, which becomes most prominent with small effective mode areas. Thus, it can be tailored by the waveguide properties, particularly via the core radius and the numerical aperture (NA) [Mit05]. Standard single-mode fused silica fibers in the 2  $\mu\text{m}$  wavelength range exhibit



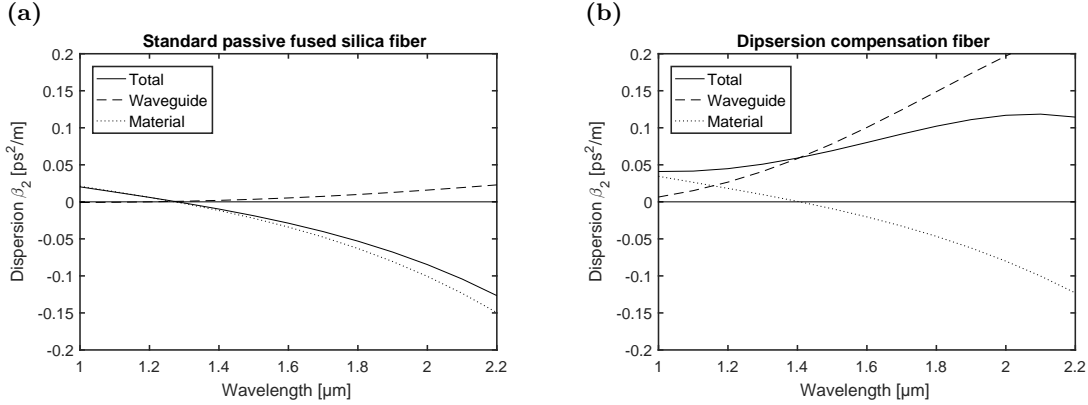


**Figure 3.2:** Simulated dispersion of (a) standard passive fiber (similar to SMF-28e+:  $d_{\text{core}} = 8.2 \mu\text{m}$ , NA 0.14) and (b) dispersion compensating fiber (similar to UHNA4:  $d_{\text{core}} = 2.2 \mu\text{m}$ , NA 0.35).

negative (so called anomalous) material and positive (normal) waveguide dispersion (see Figure 3.2(a)). In this way, a large amount of pulse broadening induced by  $\beta_2$  can be compensated by the same value with opposite sign in two fibers based on the same material, but with different waveguide geometries (see Figure 3.2(b)).

### 3.1.2 Fiber nonlinearities

If the intensity of laser radiation is sufficiently high, various nonlinearities can become relevant in addition to the aforementioned linear effects. As the second-order susceptibility tensor  $\chi^{(2)}$  vanishes in isotropic media (e.g. fused silica fibers), nonlinear effects related to the third-order susceptibility  $\chi^{(3)}$  dominate fiber nonlinearities. A more detailed mathematical description of the nonlinear light-matter interaction is given in Section 5.1. The most prominent nonlinear phenomenon in fiber lasers is the intensity-dependent nonlinear refractive index, which is defined by the linear superposition of the frequency-dependent refractive index  $n(\omega)$  and its intensity-induced modification  $n_2 I$ :

$$\tilde{n}(\omega, I) = n(\omega) + n_2 I. \quad (3.3)$$

This quasi-instantaneous change of the refractive index is called optical Kerr effect. The quantity  $n_2$  is the nonlinear index coefficient, given in  $\text{m}^2/\text{W}$ . It is related to the third-order susceptibility  $\chi^{(3)}$  by  $n_2 = 3\chi^{(3)}/(4\epsilon_0 c n_0^2)$  with the permittivity of vacuum  $\epsilon_0$ . An ultrashort pulse with high peak intensity propagating in an optical fiber with length  $l$  experiences an intensity-dependent nonlinear phase delay due to the Kerr effect, which is described by [Agr12]

$$\phi_{\text{NL}} = n_2 \frac{2\pi}{\lambda} l I(t). \quad (3.4)$$

It is called self-phase modulation (SPM), if it is induced by the pulse itself, and cross-phase modulation (XPM), if another pulse is involved. The derivative of Equation (3.4) yields the change of the instantaneous frequency generated by the SPM:

$$\delta\omega(t) = -\frac{\partial\phi_{\text{NL}}(t)}{\partial t} = -\frac{2\pi l}{\lambda} n_2 \frac{\partial I(t)}{\partial t}. \quad (3.5)$$

The instantaneous frequency changes proportionally with the negative derivative of the temporal pulse shape. It decreases at the leading edge of the pulse and increases at its trailing edge, respectively. As a consequence, new spectral components are generated for an initially transform-limited or positively chirped pulse, while a negative chirp leads to spectral narrowing.

Note that this effect is related to a temporal dependence of the phase shift. In contrast, a transverse dependence in the presence of some spatial beam profile leads to the phenomenon of self-focusing. For an optical pulse with its peak intensity  $I(z)$  propagating in  $z$ -direction through an optic medium with characteristic nonlinear refractive index  $n_2$ , the accumulated on-axis nonlinear phase shift is defined by

$$B = \frac{2\pi}{\lambda} \int n_2 I(z) dz, \quad (3.6)$$

which is denoted B-integral and will be important in Section 4.2 in terms of self-focussing in crystal-based ultrashort pulse amplifiers. Another effect, which is associated with the Kerr nonlinearity, is the nonlinear polarization rotation (NPR). After the propagation of an intense pulse in a Kerr medium (e.g. fiber), the polarization state has not only changed due to some (uncontrolled) birefringence of the material, but due to an intensity-dependent change as well. As a consequence, the polarization evolution of the high-intensity peak of the pulse differs from the low-intensity wings.

Further nonlinear effects are Raman scattering and self-steepening. The latter is a consequence of the Kerr effect. The intensity-dependent change of the refractive index  $\Delta n(t) = n_2 I(t)$  results in different group velocities within the optical pulse (see Equation (3.2)) causing the high-intensity peak of the pulse to propagate at lower speed in comparison to its low intensity wings. This effect results in an asymmetric pulse shape with a longer leading edge. As the trailing edge approaches an infinite slope, a so called shock wave can be formed, which favors wave breaking [Rot89]. At the same time, the prevailing SPM affects the optical spectrum leading to an asymmetry in the frequency domain as well. On the other hand, Raman scattering is a consequence of the non-instantaneous response of a transparent optical medium caused by vibrations of the glass matrix. This process leads to a spectral red-shift as part of the photon energy is converted to an optical phonon during an inelastic scattering process [Agr12].

### 3.1.3 Pulse propagation equation

Linear and nonlinear effects are now considered to derive a mathematical description, which is capable of modeling the pulse propagation in optical fibers. Analogous to the electromagnetic oscillation of a monochromatic plane wave with its electric amplitude  $E_0$  and the frequency  $\omega_0$  as described by

$$E(t) = E_0 e^{-i\omega_0 t} + \text{c.c.}, \quad (3.7)$$

an optical pulse propagating through a fiber can be defined as

$$E(t) = A(t) e^{-i\omega_0 t} + \text{c.c.} \quad (3.8)$$

with the pulse envelope function  $A(t)$  determining the time depending amplitude. Here, several assumptions are made to simplify the expression in Equation (3.8):  $A(t)$  is normalized such that its squared absolute value yields the average optical power  $P = |A|^2$ . Furthermore, the polarization of the optical field is considered to be invariant during propagation through the fiber, which allows a scalar approach. The typical pulse durations in this thesis are in the range of 1 to 10 ps. On this time scale it is sufficient to consider chromatic dispersion through  $\beta_1$  and  $\beta_2$  as well as fiber nonlinearities through the Kerr effect. Additionally, any change of the pulse envelope  $A(t)$  can be considered to happen on a much slower scale than the variation of the electric field  $E(t)$  (see also Figure 3.1(a)), which is denoted the slowly-varying envelope approximation. The simplified description of pulse propagation in an optical fiber is then given by the nonlinear pulse propagation equation [Agr12]

$$\frac{\partial A}{\partial z} + \beta_1 \frac{\partial A}{\partial t} + \frac{i\beta_2}{2} \frac{\partial^2 A}{\partial t^2} + \frac{\alpha}{2} A = i\gamma(\omega_0) |A|^2 A, \quad (3.9)$$

with the loss coefficient  $\alpha$ , the velocity of light in vacuum  $c_0$ , dispersive terms  $\beta_{1,2}$  as explained in Section 3.1.1, and the nonlinear parameter  $\gamma$

$$\gamma(\omega_0) = \frac{n_2 \omega_0}{c A_{\text{eff}}}. \quad (3.10)$$

Following Equation (3.10), the nonlinearities in an optical fiber are dependent on the effective mode area  $A_{\text{eff}}$  and the nonlinear refractive index  $n_2$ , which is characteristic for a specific material (e.g. silica fiber). Under appropriate transformation of Equation (3.9) into the reference frame of the propagating pulse  $T \rightarrow t - z/v_G$  (with  $v_G$  the group velocity of the pulse envelope) traveling in  $z$ -direction the following simplified equation can be

obtained [Agr12]:

$$i\frac{\partial A}{\partial z} + i\frac{\alpha}{2}A + \frac{\beta_2}{2}\frac{\partial^2 A}{\partial T^2} + \gamma|A|^2 A = 0, \quad (3.11)$$

which in the special case of  $\alpha = 0$  is denoted the nonlinear Schrödinger equation (NLSE). The analytical solution of this differential equation assuming  $n_2 > 0$  and  $\beta_2 < 0$  is an optical soliton with the temporal shape described by an unchirped  $\text{sech}^2$  pulse.

### 3.2 Generation of ultrashort pulses in fiber lasers

The gain bandwidth in rare-earth-doped fibers is large, which makes them attractive for ultrashort pulse generation. However, in comparison to their bulk counterparts, fiber lasers experience much stronger dispersive and nonlinear effects due to the long interaction length in the glass in combination with the small mode areas resulting in high optical intensities. As a consequence, the cavity boundary condition in many mode-locked fiber lasers is typically satisfied only for an operation at comparably low pulse energies and peak powers.

#### 3.2.1 Pulse regimes in fiber lasers

In the following, pulse regimes fulfilling the cavity boundary condition are described. We will see that the various dispersive and nonlinear effects in optical fibers can balance each other, resulting in a circulating pulse, which is able to reproduce itself after one resonator round-trip. Particularly, GVD and the accumulation of a nonlinear phase by SPM are the physical processes with highest impact. When the accumulated nonlinear phase of a pulse approaches  $\phi_{\text{NL}} \sim \pi$ , it will experience its distortion, which manifests itself through pulse-splitting, wave-breaking, or continuous-wave breakthrough [Fu18]. The operation regimes in ultrafast fiber lasers can be divided into three schemes, which depend on the cavity dispersion properties [Gre12]: The propagation of fundamental solitons in all-anomalous dispersion fiber lasers, stretched-pulse operation with a net cavity dispersion close to zero, and the regime with positively chirped pulses such as parabolic pulses in a similariton fiber laser [Ild04] or the wider class of all-normal-dispersion fiber lasers [Cho08]. Only the first two regimes are relevant for this thesis and will be introduced.

#### Fundamental solitons

The combination of anomalous dispersion and self-phase modulation in optical fibers has led to the development of ultrashort pulse lasers operating in the fundamental soliton regime. An optical soliton is defined as a short pulse, which does not change in the spectral and temporal domain over a long propagation distance. This can happen under certain circumstances, when the effects of dispersion and Kerr nonlinearity are balanced such that they exactly cancel each other [Mol80]. Mathematically, the soliton is a possible solution of the nonlinear Schrödinger Equation (3.11) considering anomalous dispersion ( $\beta_2 < 0$ ) and no gain ( $\alpha = 0$ ). It yields a temporal  $\text{sech}^2$ -shaped pulse, which propagates chirp-free

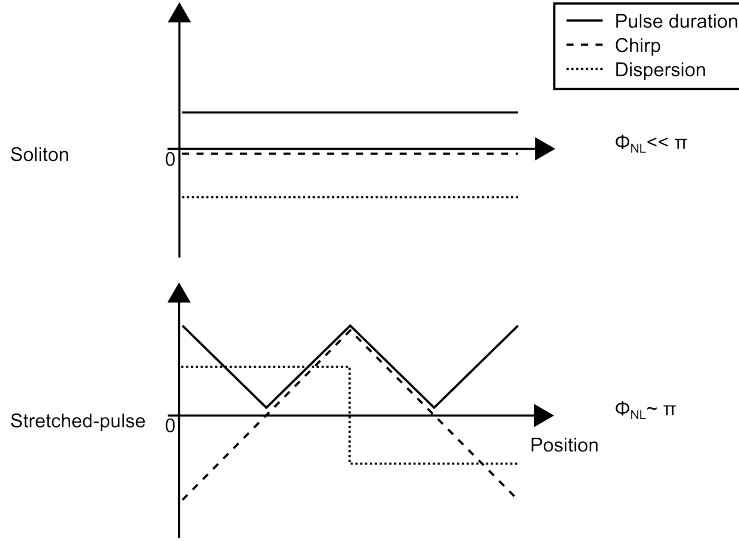


**Figure 3.3:** Schematic evolution of the pulse duration, chirp, and dispersion during cavity propagation for different pulse regimes [Wis08].

and with constant duration (see Figure 3.3). The relationship between pulse duration  $\tau$  and the corresponding pulse energy  $E_p$  of a soliton is defined by the soliton area theorem [Agr12]

$$E_p \cdot \tau = 2 \cdot \frac{|\beta_2|}{\gamma}. \quad (3.12)$$

In fiber-based ultrashort pulse oscillators, however, the propagation parameters are not constant and strong perturbations are introduced due to periodically emerging gain or losses. In fact, an optical soliton is very stable as some of its energy is exchanged with a copropagating background, which is called dispersive wave, in order to evolve towards a pulse, whose properties meet the conditions described in Equation (3.12). For some optical frequencies of the soliton and dispersive wave a kind of resonant coupling occurs, which results in the formation of narrowband peaks superimposed on the soliton spectrum. These side-peaks, which are located symmetrically around the center frequency, are called Kelly-sidebands and are a measure of the phase-matching conditions between dispersive wave and soliton [Kel92].

Drawbacks of soliton lasers are the limited pulse duration and thus achievable pulse energy, which is typically below 1 nJ [Hin17; Paw17; Sot16]. The reason is that a solitary pulse propagates always close to its Fourier-limit, thus, the destabilization threshold is rather low ( $\phi_{NL} \ll \pi$ ) [Wis08]. The pulse duration is connected to the spectral bandwidth  $\Delta\nu$  via the time-bandwidth product  $\tau \cdot \Delta\nu \geq c_B$  (with  $c_B \approx 0.315$  for  $\text{sech}^2$ -shaped pulses). Note that the equality sign in the time-bandwidth product holds for Fourier-limited pulses as in the case of a fundamental soliton. As a consequence, solitary pulses are spectrally limited as well.

### Stretched-pulse operation

The drawbacks of soliton oscillators can be overcome in the stretched-pulse concept. In this operation regime part of the anomalous dispersion is balanced with normal dispersion in the cavity, which results in a net cavity dispersion close to zero (see Figure 3.3) [Tam93]. Due to the alternating dispersion segments, intracavity temporal breathing dynamics are introduced. In comparison to the fundamental soliton, the pulse in dispersion-managed oscillators is chirped during most of its propagation. As the round-trip integrated nonlinear phase is reduced for a given pulse energy, the destabilization threshold is higher ( $\phi_{\text{NL}} \sim \pi$ ), which allows to increase the pulse energy [Nel97].

In stretched-pulse lasers with fiber-based dispersion management, the achievable pulse energies are in the range of  $\sim 1$  nJ [Li14; Paw18; Tol16], while the pulse shape is based on a Gaussian distribution [Hof92]. The main limitation arises from the point of minimal pulse duration ( $\ll 100$  fs) during the propagation inside the cavity. Alternatively, dispersion management based on bulk optics such as gratings or prisms can be applied [Hax08; Ild03]. However, these laser systems are comparably complex.

### 3.2.2 Passive mode-locking techniques

With the advent of passive mode-locking techniques ultrashort pulses with pulse durations in the ps or even fs regime have been generated in ultrafast fiber lasers [Fer13]. In combination with the CPA scheme, an ever-growing amount of applications exploiting intense radiation emerged. Mode-locking is defined as the constructive interference of longitudinal modes, which are resonant in the laser cavity. Next to the cavity boundary condition as introduced in the previous section, some mode-locking device is needed to induce a fixed phase between these oscillating modes. Here, only passive mode-locking is considered, which exploits the nonlinearity of a saturable absorption to promote the formation of short pulses from noise. Saturable absorbers have been used since the early development of solid-state lasers [DeM66; Moc65; Smi70]. Generally, there exist two types of saturable absorbers: real and artificial. In the context of this thesis, the semiconductor saturable absorber mirror (SESAM) representing a real saturable absorber and NPR representing an artificial saturable absorption mechanism are introduced.

#### Real saturable absorbers - SESAM

SESAMs have initially been used in solid-state lasers by the group of KELLER et al. from the beginning of 1990 in nonlinear coupled cavities [Hau91; Kel91; Kel90]. The saturable absorption can be described by an interband transition in a semiconductor material with quantum well structure: Photons from the leading edge of a light pulse promote electrons from the valence to the conduction band. As the pulse penetrates further into the saturable absorber, the intensity increases, which enhances the electronic excitation until the ground-state and excited-state populations are equalized. As a consequence, the absorption reduces. With the lower intensities of the trailing edge of the short pulse, the absorption recovers. While the absorption is almost instantaneous, the recovery time shows some

rapid intraband thermalization within the first  $\sim 100$  fs followed by carrier recombinations, which can be rather long up to several tens of ps [Jun97; Kno88]. In principle, semiconductor saturable absorbers can be used either in transmission or in reflection with a Bragg mirror. The latter case is also often called saturable Bragg reflector and can be implemented as end mirror in a linear resonator or in a ring cavity via  $\sigma$ -arm. The device properties need to be tailored carefully [Hai04; Kel96]. Some of them are the absorption wavelength, the modulation depth, the reflection bandwidth, the saturation energy, non-saturable losses, the laser-induced damage threshold, and the aforementioned recovery time.

#### Artificial saturable absorbers - NPR

Artificial saturable absorbers are often based on the Kerr nonlinearity. In an optical non-polarization maintaining (PM) fiber an intense pulse will exhibit a nonlinear change of its arbitrary polarization state due to SPM and XPM in combination with some uncontrolled birefringence (see Section 3.1.2). This phenomenon is known as nonlinear polarization rotation and has been initially shown by MAKER et al. [Mak64] in liquids. It results in an intensity-dependent transmission through a combination of a fiber and a polarizing element. Under a certain input polarization state the low-intensity temporal pulse wings of an optical pulse can be discriminated against the high-intensity pulse central part. The phenomenon of NPR is used in fiber lasers for passive mode-locking since 1992 [Fer93; Hof92; Mat93; Tam92]. In contrast to the rather slow saturable absorption mechanisms in real saturable absorbers, NPR is denoted to be a fast saturable absorber due to the quasi-instantaneous Kerr effect [Ipp94]. While this behavior is beneficial for the formation of sub-100 fs pulses, it suffers from drawbacks in terms of self-starting capabilities. Typically, continuous-wave mode-locking is initiated at an increased pump power level in the multi-pulse regime. Stable single-pulse operation is achieved after reducing the pump power.

### 3.3 Properties of holmium-doped fibers

As other laser-active elements such as erbium (Er), ytterbium (Yb), neodymium (Nd), or thulium (Tm), holmium (Ho) is one of the lanthanides that are a sub-group of the rare-earth elements. The trivalent Ho ion can be doped into a multitude of host materials like crystals or amorphous silica fibers. The broad spectral bandwidth of Ho in silica fibers represented by the emission cross section in Figure 3.4(b) is suitable for the generation of sub-ps pulses. Efficient in-band pumping with lowest quantum defect corresponds to the same  $^5I_8 \rightarrow ^5I_7$  transition, which is depicted in the schematic energy level diagram in Figure 3.4(a). The energy scheme indicates a quasi-three-level nature of the Ho with a strong overlap of the emission and absorption band. Thus, Ho-doped fiber lasers suffer from re-absorption effects. The strongest absorption is located in a broad wavelength band around 1950 nm [Kur10; Sim13], which can be addressed by Tm-doped fiber lasers with tens or even hundreds of Watts of output power [Pho19].

Additionally, Figure 3.4(a) indicates an excitation into the  $^5I_6$  band corresponding to a wavelength of 1120-1160 nm. The spectral region can be addressed by Yb-based fiber lasers

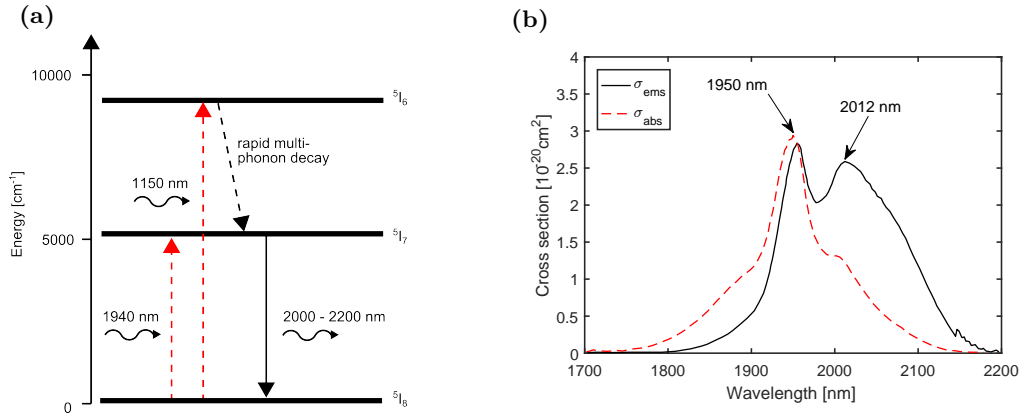


**Figure 3.4:** (a) Schematic energy level diagram with the most important transitions and (b) corresponding emission and absorption cross sections of holmium-doped silica fiber (digitized from [Sim13]).

or laser diodes. Especially the latter pumping concept with single-mode fiber-coupled laser diodes allows for low-cost and compact setups, however, at the expense of efficiency due to the increased quantum defect. Particularly for high-power applications, 1950-nm pumping benefits from the remarkably low quantum defect of  $\sim 5\%$ . As a consequence, the thermal population of the lower laser level induced by the heat load in such pumping schemes is less pronounced than that for 1140-nm pumped systems ( $> 40\%$  quantum defect). In all cases core-pumping is typically used in ultrashort pulse oscillators in order to reduce the fiber nonlinearities, whose impact depend on the fiber length.

Figure 3.5 shows the calculated effective gain cross section based on the data presented in Figure 3.4(b). Note that the corresponding Equation (4.3) will be introduced in the next Chapter 4. With increasing inverted fraction not only the center wavelength exhibits a blue shift from 2150 nm to  $< 2050$  nm, but also the full-width at half-maximum (FWHM) gain bandwidth broadens to more than 80 nm. The shortest possible pulse duration directly

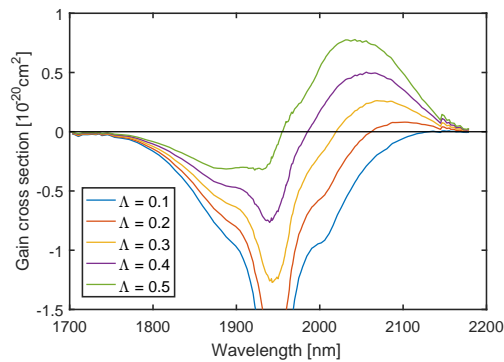


**Figure 3.5:** Effective gain cross section of holmium-doped silica fiber at different inverted fractions  $\Lambda$  as introduced in Equation (4.4).



from a Ho-doped silica fiber oscillator was 160 fs with a pulse spectral FWHM of 37 nm [Li14]. Laser pulses with even broader optical spectrum of 53.5 nm FWHM have been shown by PAWLISZEWSKA et al. [Paw18], which were compressible towards a pulse duration of 190 fs. The corresponding Fourier-limited pulse duration, however, was 116 fs.

### 3.4 All-fiber mode-locked oscillator

In the last few years, passive mode-locking in Ho-doped fiber lasers has been achieved by means of saturable absorbers based on semiconductor [Cha12a; Hin17; Tol16], graphene [Dvo15; Sot16], carbon nanotubes [Cha12b], or black phosphorus materials [Paw17]. Alternatively, artificial saturable absorbers such as NPR [Fil16; Kam16; Li14] have been successfully demonstrated. While the fast response time of the NPR mode-locking scheme provides stable and efficient ultrashort pulse formation, it exhibits a higher self-starting threshold compared to the conventional saturable absorbers with slow response time [Kär98; Obe93]. A hybrid mode-locking configuration based on NPR and a saturable absorber mirror has been presented by Li et al. [Li16] with improved self-starting capabilities compared to mode-locking, which was initiated solely by NPR. The generated solitonic pulses could be spectrally tailored such that they meet the spectral requirements to efficiently seed amplifiers based on Ho:YLF crystals. However, the laser resonator consisted of a free-space part, which was prone to environmental influences. In this context, an all-fiber ultrashort pulse oscillator based on hybrid mode-locking mechanism has the potential to offer stable pulse generation in a turn-key system as will be presented in the following. Standard single-mode fibers exhibit anomalous dispersion in the 2  $\mu\text{m}$  wavelength range. Pulse propagation in such fibers leads to spectral narrowing due to the SPM effect. In particular, subsequent fiber-based pre-amplifiers will suffer from this fact. In order to maintain sufficient bandwidth for subsequent crystal-based amplifiers, at least 10 nm FWHM needs to be achieved. Therefore, an ultrashort pulse oscillator in the stretched-pulse regime will be presented. In addition, if the laser is properly designed, the out-coupled pulses are temporally stretched to  $> 1$  ps, thus, no temporal stretching is required prior to the pulse amplification in fiber-based pre-amplifiers.

In this work, the generation of ultrashort pulses in a hybrid mode-locked all-fiber oscillator based on Ho-doped silica fiber is presented. Figure 3.6 depicts the experimental setup. The laser cavity consisted of 0.85 m Ho-doped fiber (iXblue, IXF-HDF-8-125) with a core diameter of 8  $\mu\text{m}$  and a numerical aperture of 0.16. The fiber absorption is  $> 15$  dB/m at the pump wavelength of 1150 nm as specified by the fiber manufacturer. If not stated otherwise, the dispersion values of the different fibers used in this setup were calculated based on the mode-field diameter at the target wavelength of 2050 nm, which is defined by the fiber geometry such as the NA and core radius [Mar77]. Both the material and waveguide dispersion were considered. The anomalous dispersion per length of the Ho-doped fiber amounts to  $\beta_{2,\text{HDF}} = -95.7 \text{ fs}^2/\text{mm}$ . It was core-pumped by a 300 mW fiber-coupled diode laser at a wavelength of 1150 nm via a wavelength division multiplexer (WDM). The latter was designed to combine the pump and signal wavelengths of 1150 nm and 2050 nm, respectively. The active fiber was followed by a

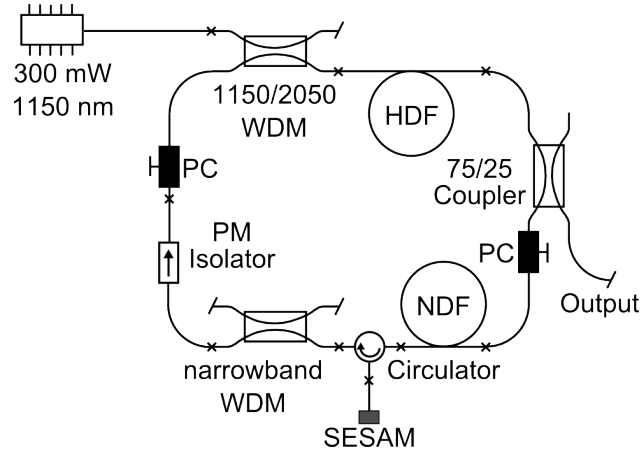


**Figure 3.6:** Experimental setup of the holmium-doped fiber oscillator. SESAM: semiconductor saturable absorber mirror, PC: polarization controller, WDM: wavelength division multiplexer, PM: polarization maintaining, HDF: holmium-doped fiber, NDF: normal dispersive fiber.

75/25-coupler (0.78 m SM2000 fiber, Thorlabs), which provides 25% output coupling. The dispersion management was achieved by using about 4.8 m of passive normal dispersion fiber (NDF), which exhibits an ultra-high numerical aperture (UHNA) (Nufern, UHNA4). The corresponding fiber properties are a 2.2  $\mu\text{m}$  core diameter and a NA of 0.35, which results in a calculated mode-field diameter of 6.6  $\mu\text{m}$  at a wavelength of 2050 nm. The normal dispersion per length at this specific wavelength is about  $\beta_{2,\text{NDF}} = 90 \text{ fs}^2/\text{mm}$  [Paw18]. A sigma arm configuration was applied by means of a fiber-based circulator (SMF-28, AFR Ltd.) to implement a commercially available SESAM (Batop GmbH, SAM-2000-30-10ps). It exhibits a modulation depth of 12% and a saturation fluence of  $70 \mu\text{J}/\text{cm}^2$ . Another in-house built WDM (0.6 m SM2000 fiber) with narrow transmission bandwidth around 2050 nm was used to force the laser emission to the desired wavelength. Finally, a fiber-based isolator (0.5 m PM1550, AFR Ltd.) provided unidirectional pulse propagation in the ring cavity. It simultaneously acts as a polarizer (fast axis blocked). The passive single-mode fiber originating from the pigtails of the components sums up to a total length of about 4.3 m, from which 0.3 m can be attributed to the sigma arm formed by the circulator (SMF-28 pigtails). The calculated net cavity dispersion is about  $-0.12 \text{ ps}^2$ .

Hybrid mode-locking was achieved by NPR in the unidirectional ring cavity and the SESAM. The NPR mode-locking was formed by the careful adjustment of two polarization controllers and the polarizers of the isolator. In order to keep the polarization properties of the non-PM fiber constant to ensure stable mode-locking even when the environmental temperature changes, the complete laser resonator and all-fiber-based components were secured on a temperature stabilized metal plate. Furthermore, the ultrashort pulse oscillator was simulated by means of a commercially available software (fiberdesk, version 4.0) in order to verify the experimental results. The numerical simulation solves the extended NLSE by the split-step Fourier method [Sch19]. The fiber and operation parameters presented above were considered as well as the assumptions given in the Appendix A.

At a pump power of 250 mW the mode-locking operation was self-starting in the single-pulse regime. The average output power was about 2 mW, which corresponds to a pulse energy of 105 pJ at a fundamental repetition rate of 20 MHz. The measured pulse energy is consistent with the simulation results. Higher pump power resulted in multi-pulsing due to the overdriven NPR without any onset of continuous wave peaks. The corresponding optical spectrum is shown in Figure 3.7(a) (black solid line), which yields a FWHM spectral bandwidth of 10.8 nm around the center wavelength of 2050 nm. Due to the dispersion management, Kelly sidebands, which are characteristic for the fundamental soliton regime, are not visible. In comparison, the result obtained from the numerical model as shown in Figure 3.7(a) for the power spectrum (red dashed line) is in line with the experimental result. In the same figure, the spectral transmission of the narrowband filter WDM is depicted. It is showing that the emission of the ultrashort pulse oscillator is almost perfectly following the WDM's transmission properties, which proves its spectral stabilization to the desired center wavelength. Figure 3.7(b) shows the simulated autocorrelation (red dashed line) as well as the calculated Fourier-limited pulse duration (black solid line) based on the measured optical spectrum from Figure 3.7(a). The latter yields 582 fs, while the uncompressed pulse duration based on numerical simulations is 1.55 ps assuming a Gauss-shaped pulse. It is worth mentioning that the pulse duration at the output coupling of the oscillator could not be measured due to the insufficient average optical power generated by the fiber oscillator. The discrepancy between the pulse duration and the Fourier-limit can be explained by the stretched-pulse regime, in which the pulse duration is not constant during the propagation of the pulse in the cavity. Thus, the emitted pulses from the oscillator were temporally chirped. Temporal compression or further stretching of the pulses was not necessary, as the ps pulse duration was suited well for seeding a subsequent fiber-based pre-amplifier (Section 3.5).

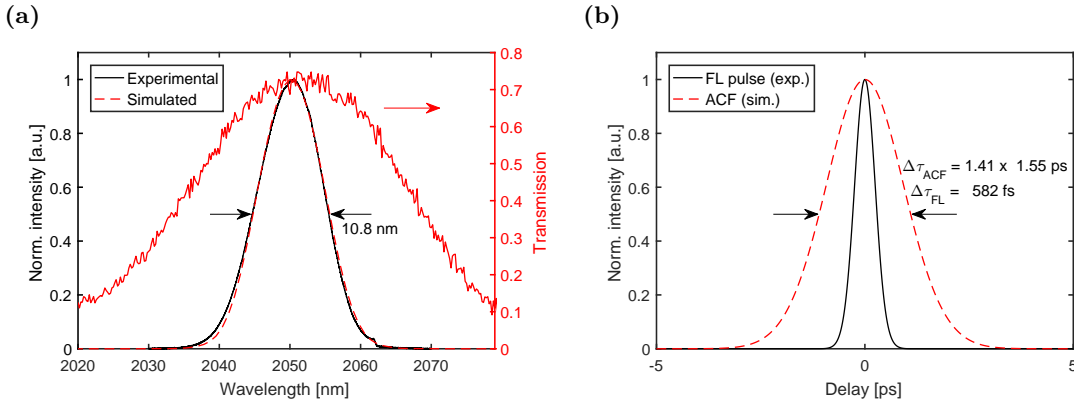


**Figure 3.7:** (a) Experimental (black solid line) and simulated (red dotted line) optical spectrum of the ultrashort pulse oscillator and transmission of the narrowband WDM measured with an optical spectrum analyzer with a resolution of  $\Delta\lambda_{res} = 0.05$  nm. (b) Fourier-limited pulse duration based on the measured optical spectrum (black solid line) and simulated autocorrelation (red dashed line).

By measuring the output pulse train with a 12.5 GHz photo diode in combination with a 26.5 GHz radio-frequency spectrum analyzer (Agilent E4440A) and a 6 GHz oscilloscope, single-pulse operation could be verified. The results are shown in Figure 3.8, indicating a pulse repetition frequency of 19.84 MHz. The measured fundamental beat note in Figure 3.8(a) coincides with the total cavity round-trip length of about 10.5 m. The signal-to-noise ratio with  $> 81$  dB is higher than those of previously reported passively mode-locked Ho-fiber lasers [Fil18; Paw17; Sot16]. The radio-frequency comb up to 1 GHz in Figure 3.8(b) shows no signs of q-switching instabilities. Figure 3.9(a) shows the oscilloscope trace of the measured pulse train. The pulse-to-pulse temporal distance of 50 ns is well-suited to apply pulse pickers based on an acousto-optic modulator (AOM), whose rise and fall time is typically in the range of a few 10 ns.

Oscillators which are used to seed subsequent amplifiers require low amplitude noise. An analysis of the relative intensity noise (RIN) of the mode-locked pulse train provides detailed information about the noise characteristics of the source and their origins. The output of the ultrashort pulse oscillator was sampled with a 25 MHz photo diode (Thorlabs, PDA10D2) with transimpedance amplifier. The power spectral density was recorded in the frequency range from 1 Hz to 100 kHz by means of a signal analyzer (Stanford Research Systems Model SR785) in combination with two 11 MHz low pass filters. The frequency range between 100 kHz and 10 MHz was detected by the radio-frequency spectrum analyzer instead due to the higher dynamic range. Above 200 kHz the measurement was limited by the technical noise floor. The experimental results of the corresponding RIN are shown in Figure 3.9(b). In general, there are no signs of acoustic or vibrational noise. This proves the stability of this laser system against environmental influences due to its all-fiber nature. The root mean square (rms) integrated RIN from 1 Hz to 10 MHz is shown in Figure 3.9(b) in the upper diagram. It is about 0.013 %rms for the oscillator in the complete frequency window. In comparison to similar mode-locked Ho-doped fiber lasers, the integrated RIN is an order of magnitude lower [Li14]. This improved operation stability can be attributed

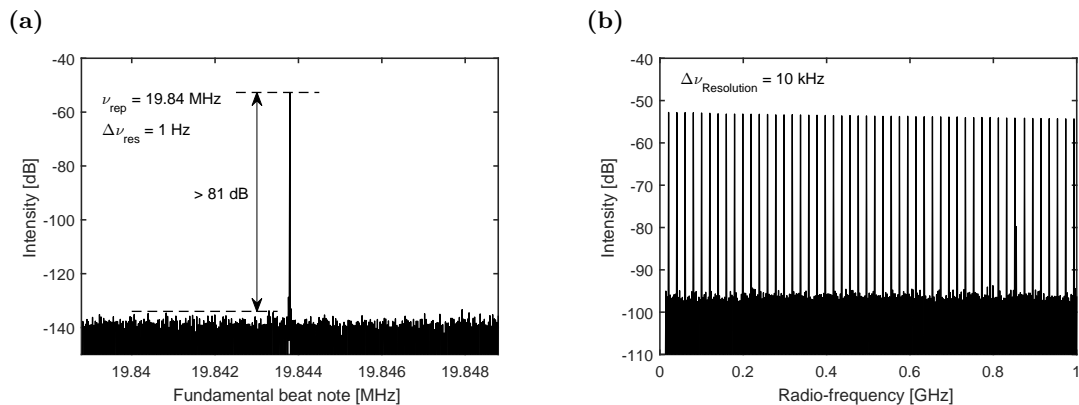


**Figure 3.8:** (a) Measured fundamental beat note and (b) radio-frequency comb up to 1 GHz measured with a RF spectrum analyzer.

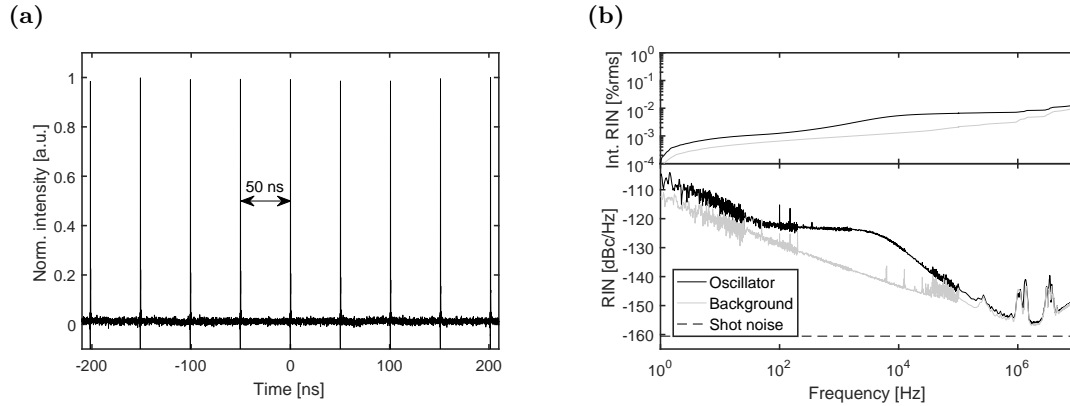


**Figure 3.9:** (a) Oscilloscope trace of the measured pulse train emitted by the ultrashort pulse laser source. (b) RIN measurement of the Ho-doped fiber oscillator (black solid line), technical background noise (grey solid line), and shot noise limit (black dashed line).

to the low-noise pump source and an all-fiber setup design in combination with the hybrid mode-locking stability.

### 3.5 Fiber-based pre-amplifier

The amplification of ultrashort pulses in single-mode fiber-based amplifiers is challenging: Due to the rather long interaction length of the pulse in the glass material and the small mode-field areas resulting in high peak intensities, strong linear (e.g. dispersion) and nonlinear (e.g. SPM) effects occur, which affect the pulse in the time as well as in the frequency domain. Some of these effects are unwanted, especially, when a pulse with certain spectral and temporal properties for seeding crystal-based amplifiers is required. However, some of the detrimental fiber nonlinearities scale with the inverse of the driving wavelength  $\lambda$  such as stimulated Raman scattering, self-phase modulation (see Equation (3.4)), or four-wave mixing [Agr12]. The self-focusing limit even depends on the inverse  $\lambda^2$  (see Equation (4.10)). Additionally, the core diameter of standard single-mode fibers scales linearly if the NA is kept constant [Sny83]. At the same time, the mode-field diameter of the propagating beam is enlarged reducing the on-axis peak power while maintaining the single-mode waveguide properties. In consequence, the longer wavelength at  $2\mu\text{m}$  in comparison to the well-established near-IR sources benefits from reduced impact of nonlinear effects during pulse propagation in the fiber [Stu14], hence, the achievable pulse energy in CPA-free fiber-based ultrashort pulse amplifiers can be considerably higher. This fact is beneficial, as seeding crystal-based amplifiers with increased pulse energies enhances gain saturation effects. Particularly in the case of multipass amplification schemes, this results in a reduced amount of passes through the crystal required for high extraction efficiencies, which in turn simplifies the overall system design and handling.

The developed pre-amplifier consisted of two amplifier stages based on Ho-doped fibers as sketched in Figure 3.10. Prior to the first one, a 99/1-coupler was used in order to monitor

the oscillator's output. The first amplifier was core-pumped by a 350 mW single-mode diode laser at a wavelength of 1150 nm via a WDM. The active fiber was a 1.5 m long Ho-doped fiber similar to the one used in the oscillator. In a subsequent piece of standard passive single-mode fiber the polarization was tuned by means of a polarization controller such that the transmission through a PM isolator (fast axis blocked, polarization maintaining fiber pigtails) is maximized. The second amplifier was based on a 1.4 m long PM Ho-doped fiber (iXblue, IXF-HDF-PM-8-125) with same core size of 8  $\mu\text{m}$  and NA of 0.16, but a Panda-type PM structure. The active fiber was core-pumped by a Tm-doped fiber amplifier system with emission at 1950 nm and an output power > 5 W. Pump and signal were combined via a WDM, which was PM as well.

The amplifier was seeded with 2 mW of average output power of the oscillator. The 1150 nm-pumped first amplifier stage generated an amplified signal with an average output power of 20.5 mW measured behind the polarizing isolator. The pulse duration of 5.3 ps based on a Gauss-shaped pulse was measured with an autocorrelator and was slightly longer than the one of the oscillator output. This can be explained by some negative dispersion ( $\beta_2 < 0$ ), which is accumulated in the anomalous dispersion fiber. Due to the polarizing nature of the isolator, the output of the second amplifier stage was linearly polarized. Figure 3.11(a) shows the optical output power in dependence on the pump power. The slope efficiency (red dotted line) is about 67%. The optical-to-optical efficiency based on the absorbed and emitted average optical pump and signal power, respectively, amounts to  $\sim 50\%$  at maximum pulse energy of  $\sim 39$  nJ.

As the main intention of this laser system is seeding Ho:YLF amplifiers, some more investigations concerning the operation stability were conducted. First, the average optical output power was measured behind a polarizer over a period of 3 h. At a power level of about 500 mW the root mean square noise amounts to less than 0.1% (see inset of Figure 3.11(a)),

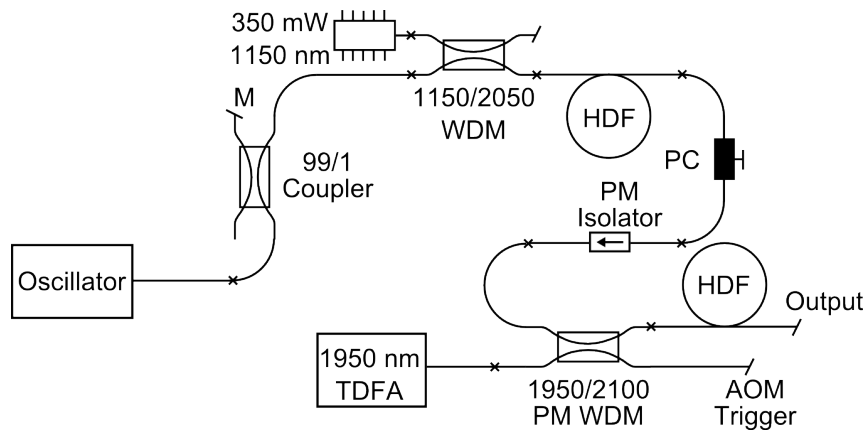


**Figure 3.10:** Experimental Ho-doped fiber pre-amplifier setup. M: monitoring port, HDF: Ho-doped fiber, PC: polarization controller, PM: polarization maintaining, TDFA: Tm-doped fiber amplifier, WDM: wavelength division multiplexer, AOM: acousto-optic modulator.

which is in the range of the accuracy of the used power meter head. Note that due to the polarizer any change of the polarization state will directly influence the measured power signal. A more detailed analysis in terms of the intensity noise was done by measuring the RIN (see Figure 3.11(b)) as explained in Section 3.4. The noise spikes between 10 Hz and 10 kHz can be attributed to acoustic and vibrational influences. Measuring the power spectral density of the Tm-based pump source reveals that these noise contributions were induced by the pump laser. Nevertheless, the integrated RIN of the oscillator in the complete frequency range is only slightly higher at 0.015 %rms than that of the oscillator with 0.013 %rms. It is dominated by the pump source in the low-frequency range while the high-frequency contributions are not transferred to the amplified signal. In contrast, the integrated RIN over the aforementioned frequency range for the pump source is 0.065 %rms.

The maximum pulse energy was limited by the onset of nonlinear effects, particularly SPM. The latter manifests itself through spectral modulations that scale with the generated pulse energies as can be seen in Figure 3.12(a) (black solid lines). Due to the combination of anomalous dispersion and SPM, the FWHM of the optical spectrum is reduced from initially 10.8 nm measured at the oscillator monitoring port (see Figure 3.10) to 2.3 nm for amplified pulses with a pulse energy of 34.3 nJ. Nevertheless, the measured autocorrelation traces up to the highest pulse energy (Figure 3.12(b), black solid lines) show no signs of temporal perturbations. Note that similar results with pulse energies up to 75 nJ have been published in [Hin17], however, with strong SPM-induced spectral distortions. The measured pulse duration is nearly constant for all amplification factors ( $1.54 \times 5.7$  ps autocorrelation FWHM). The corresponding Fourier-limited pulse FWHM at a pulse energy of 34.3 nJ is 660 fs. During the experiments no amplified spontaneous emission was detected.

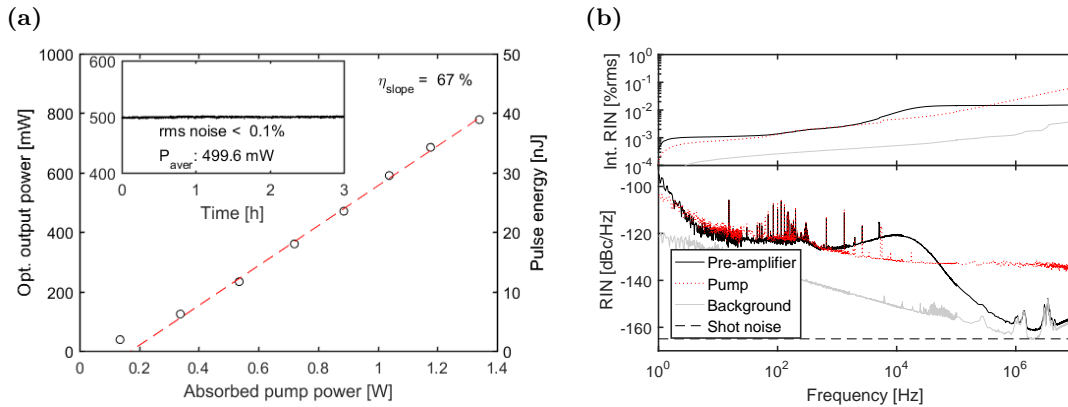


**Figure 3.11:** (a) Average output power and corresponding pulse energy vs. the absorbed pump power (black circles). The linear fit (red dashed line) indicates a slope efficiency of 67%. Inset: Long-term measurement at a fixed output power of 500 mW over a time period of 3 h. (b) RIN measurement of the pre-amplifier (black solid line), technical background noise (grey solid line), and shot noise limit (black dashed line).



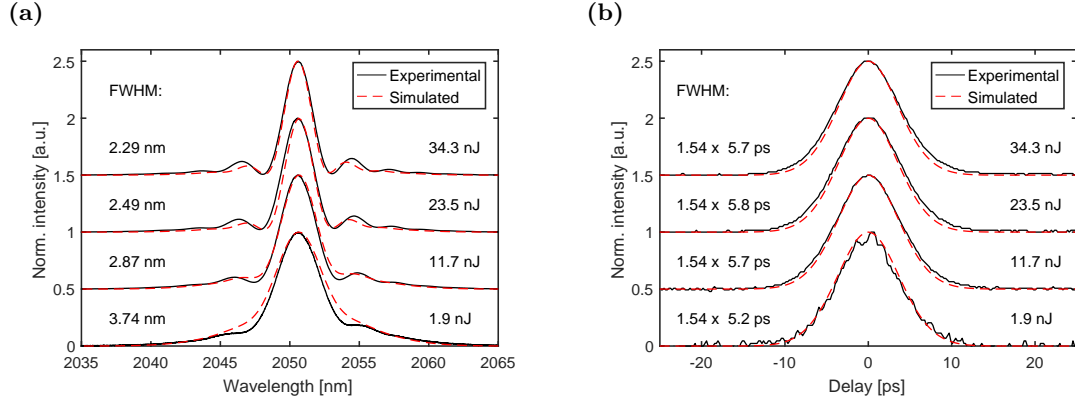


**Figure 3.12:** (a) Experimental (black solid lines) and simulated (red dashed lines) optical spectrum at different pulse energies and (b) corresponding autocorrelation traces.

The fiber-based pre-amplifier was modeled similarly to the ultrashort pulse oscillator. Every single component as depicted in Figure 3.10 was considered and the pulse energy was adapted to the measured values. The results shown in Figure 3.12(a) and (b) are consistent with the experimental data. Some deviations occur for the power spectrum, which yields a less pronounced SPM effect for all different output energy levels. This can be explained by the MFD, which can only be roughly estimated for the given fiber parameters. However, the mode area has a major impact on the fiber nonlinearities. Additionally, the experimental results exhibit a slightly asymmetric distribution of the spectral intensity. This could only be modeled by assuming a gain bandwidth of 40 nm centered at 2060 nm. This implies that the amplification of 2050 nm occurred at the rather short wavelength edge of the gain profile in the Ho-doped fiber under given conditions.

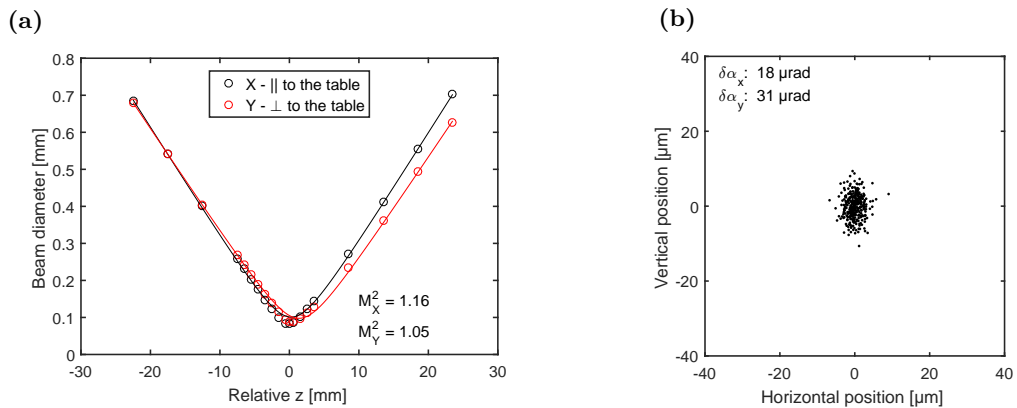


**Figure 3.13:** (a)  $M^2$  measurement at an average output power level of 500 mW: measured data (circles) and fitted caustic (solid lines) according to Equation (3.13). (b) Pointing stability measurement over a period of 5 min.



The output beam quality is another important parameter, which determines the suitability for crystal-based amplifiers. The spatial beam profile was measured with a scanning slit beam profiler (NanoScan from Ophir Optronics Solutions Ltd.). The evolution of the beam radius at  $1/e^2$  along the propagation axis behind a focusing lens yields the beam quality factor  $M^2$  by fitting the caustic to the evolving beam width of Gaussian-like beams:

$$w(z, w_0, z_0, M^2) = w_0 \sqrt{1 + \frac{\lambda^2}{\pi^2} \left( \frac{M^2(z - z_0)}{w_0^2} \right)^2}, \quad (3.13)$$

with  $w$  being the  $1/e^2$  beam radius at the position  $z$  in propagation direction,  $w_0$  the beam waist radius at position  $z_0$ , and  $\lambda$  the center wavelength. Figure 3.13(a) shows the measurement of the beam propagation parameter  $M^2$  at the power level of 500 mW. The calculated values for the direction parallel and perpendicular to the optical table are 1.16 and 1.05, respectively.

In addition, the pointing stability was recorded. Any beam angular instability  $\delta\alpha$  strongly correlates into pulse energy fluctuations in subsequent crystal-based amplifiers. The following equation describes the relationship between the standard deviation  $s$  of the beam center position  $x_i$  and  $\delta\alpha$  [ISO05]:

$$\delta\alpha = \frac{2}{f} \cdot s = \frac{2}{f} \sqrt{\frac{1}{N-1} \sum_{i=1}^N (x_i - \bar{x})^2}, \quad (3.14)$$

where  $f$  is the focal length of the used focusing optical element. Here, a lens with focal length of 200 mm was used to focus the output beam of the fiber-based pre-amplifier with an average power set to 500 mW to the automatized scanning slit beam profiler with a sampling rate of 5 Hz. The collected data over a period of 5 min is shown in Figure 3.13(b). The standard deviation  $s$  of the beam center position amounts to 1.9  $\mu\text{m}$  and 3.3  $\mu\text{m}$  in horizontal and vertical direction, respectively. Considering an average focal beam waist of 191  $\mu\text{m}$  (horizontal) and 204  $\mu\text{m}$  (vertical), this corresponds to less than 1.7%. According to Equation (3.14), the obtained angular stability is 18  $\mu\text{rad}$  in horizontal and 31  $\mu\text{rad}$  in vertical direction. Note that the beam pointing can be considered as one of the contributing noise sources in the RIN measurement presented above.

### 3.6 Summary and outlook

In this chapter an all-fiber laser source for Ho:YLF amplifier seeding was presented. It consisted of a turn-key, ultrashort pulse oscillator, which generates sub-10 ps pulses by means of hybrid mode-locking at a wavelength of 2.05  $\mu\text{m}$ . The oscillator was core-pumped by a fiber-coupled laser diode with emission at 1150 nm, which is beneficial regarding compactness, cost efficiency, and simplicity of such laser systems in comparison to conventional pump schemes based on thulium-fiber master oscillator power amplifier (MOPA)

architectures with emission around 1950 nm. The system operated environmentally stable with less than 0.013 %rms in the frequency range between 1 Hz up to 10 MHz limited by technical noise.

The pulses were amplified in a fiber-based amplifier up to tens of nJ in a CPA-free scheme. The output parameters fit the spectral requirements to efficiently seed amplifiers based on Ho:YLF crystals. Though the spectral bandwidth was reduced due to the SPM effect, it was sufficient to support sub-10 ps pulses. Additionally, the pulse-to-pulse temporal distance was sufficiently long, which allows pulse picking with acousto-optic modulators for more freedom in terms of the pulse repetition frequency compared to conventional pulse picking with Pockels cells.

Scaling the mode-field diameter in subsequent fiber-based amplifiers by means of large mode area (LMA) fibers could further boost the achievable pulse energy while maintaining a CPA-free concept and sub-10 ps pulse duration. Ho-doped LMA fibers with a core diameter of up to 40  $\mu\text{m}$  are commercially available [Nuf19], but still rather expensive. Nevertheless, the calculated mode-field area in this case scales by a factor of 10 in comparison to the one calculated from the Ho-doped fibers used in this work, which in turn would theoretically allow to increase the achievable pulse energy by an order of magnitude. The energy scaling potential in LMA fibers usually comes at the expense of a reduced beam quality as higher-order modes can propagate in such waveguides. However, under certain circumstances, it may be possible to discriminate higher-order against the fundamental mode, which results in an operation close to the diffraction-limit [Fer98; Kop00].

A different concept of scaling the pulse energy in a CPA-free approach is the multipass amplification in holmium-doped crystals, which will be demonstrated in the following chapter. In comparison to the pulse propagation in fibers, free-space propagation in bulk optical components benefits from a large design freedom. This allows to carefully tailor the beam properties in order to mitigate nonlinear effects or laser-induced damage.

# CHAPTER 4

---

## CPA-free amplification based on holmium-doped crystals

---

In this chapter, the amplification of sub-10 ps pulses up to the mJ-level pulse energies in Ho-doped yttrium lithium fluoride (YLF) crystals is presented. Section 4.1 introduces the different amplification schemes, which can be used in combination with CPA-free systems. In Section 4.2 a numerical model will be introduced, which is capable of simulating pulse energy growth in crystal-based amplifiers with pulse durations well below the excited-state lifetime. At the same time, chromatic effects can be studied such that a proper amplifier design can be found. The properties of Ho-doped crystals are summarized in the following Section 4.3. The developed Ho:YLF amplifier system can be divided into two parts: a high-gain multipass amplifier, which will be described in detail in Section 4.4 and a booster amplifier presented in Section 4.5. Finally, this chapter will be summarized in Section 4.6.

### 4.1 CPA-free amplification schemes for ultrashort pulses

Today, mode-locked lasers are used to generate ultrashort pulses, but in fiber-based oscillators, the achievable pulse energy is typically limited to the pJ- or nJ-level as has been shown in the previous Chapter 3. Scaling the pulse energies up to the  $\mu$ J- or even mJ-level requires subsequent amplification. In order to mitigate nonlinear effects in ultrashort pulse amplifiers, which can lead to pulse shape distortions or even the destruction of the gain material, chirped-pulse amplification is the most common technique if the generation of intense laser pulses is desired [Str85]. Here, the pulse duration of the seed pulse is temporally stretched prior to its amplification. After amplification at highly reduced peak power, the pulse is compressed to the shortest possible duration. As this method paved the way towards the production of enormously intense optical pulses, the CPA technique has been awarded with the Nobel Prize in 2018. However, CPA has the disadvantage of being relative complex requiring very precise alignment of efficient, cost intensive stretchers and compressors. Alternatively, the CPA-free amplification represents the most promising technique to truly enter the field of low-cost and efficient industrial micromachining.

Due to the comparably long propagation length in fiber-based amplifiers, the single-pass gain can be high ( $> 35$  dB) as most of the stored energy is extracted [Fil15]. In contrast, amplifiers based on bulk gain medium usually have low gain per pass whereas multiple passes provide a high overall gain. Two different concepts are established using amplification of low-energy seed pulses. The first approach is regenerative amplification, which is based on coupling the seed pulse into an optical resonator containing the gain material. An optical switch is used in order to trap the pulse inside the cavity by means of the polarization,

diffraction, or simple reflections. After a certain amount of intra-cavity round-trips, thus several passes through the gain medium, the same optical switch releases the amplified pulse from the cavity. Commonly, a Pockels cell is used in regenerative amplifiers as optical switch. It consists of one or multiple electro-optic crystals, which simply define the number of intra-cavity round-trips via their electronic switching configurations set by a computer leading to a very high overall gain ( $> 40$  dB). However, they are not capable of handling MW-level pulse peak power as their comparably strong nonlinear impact scales with the same amount of passes. As a result, regenerative amplifiers are typically applied hand in hand with the CPA. Additionally, the combination of high switching rates ( $> 10$  kHz) and a high voltage leads to adverse effects such as piezoelectric ringing or resonance effects [Ber15]. These switching constraints together with bifurcation effects [Dör04; Gri07] limit the achievable pulse repetition frequency. The second approach is a multipass amplifier where the seed pulse is geometrically folded several times through the gain medium using different angles of incidence. In comparison to regenerative amplifiers, multipass amplifiers contain only the gain medium itself. This is beneficial for mitigation strategies in terms of nonlinear effects, when a CPA-free amplification scheme is desired. The major drawback of the multipass amplification scheme is the fixed amount of passes through the gain medium, whose design and alignment can be rather sophisticated if the amount becomes considerably large. In the following I will show that studying how the pulse intensity and fluence evolve during the amplification process allows to find an appropriate CPA-free amplifier design with gain factors similar to the ones of regenerative amplifiers while mitigating nonlinear effects or laser-induced damage to the optical components. Reasonable setup parameters such as doping concentration of the crystal, beam size, length of the gain medium, and number of passes can be found by means of preliminary simulations.

## 4.2 Numerical simulation model for pulse amplification

A common approach to simulate the amplification of monochromatic pulses with pulse durations well below the excited-state lifetime is the classical Frantz-Nodvik formalism [Fra63]:

$$J_{\text{out}} = J_{\text{sat}} \cdot \ln \left[ 1 + e^{g_0} \left( e^{J_{\text{in}}/J_{\text{sat}}} - 1 \right) \right], \quad (4.1)$$

with  $J_{\text{in,out}}$  the input and output fluence of the pulse and  $J_{\text{sat}}$  the saturation fluence. In 2005, this numerical approach has been extended into a chromatic version, which is based on the definition of a spectral variation of the stored fluence  $J_{\text{stor}}(\lambda)$  [Ray05]. However, as the energy conservation is not directly fulfilled, a calibration with monochromatic values of the saturation fluence and the small-signal gain at the central wavelength of the initial input pulse was necessary. Just recently, the classical Frantz-Nodvik equations have been reformulated from updating the gain to equivalent expressions that update the inverted fraction instead [Kro16a]. In this approach the energy is conserved owing to the direct relation between the inverted fraction of the gain medium  $A$  and the extracted fluence  $\Delta J$ . Homogeneous broadening has been simulated by temporally slicing the pump and seed

fluence, which are consecutively simulated by updating the inverted fraction after each slice propagating through the gain medium. A similar approach to numerically simulate regenerative amplification with homogeneous broadening has been pursued by reallocating the residual fluence after each pass [Gra16]. Additionally, the evolution of the pump field and the inverted fraction is iterated along the propagation axis inside the gain medium by splitting it into slices.

In the following, the numerical model used in this thesis will be introduced. The wavelength-dependent single-pass gain or single-pass absorption in a medium with length  $l$  is defined as

$$G(\lambda) = \exp(\sigma_g(\lambda)Nl), \quad (4.2)$$

with  $\sigma_g(\lambda)$  the spectral gain cross section, which is dependent on the characteristic emission and absorption cross section  $\sigma_{ems}(\lambda)$  and  $\sigma_{abs}(\lambda)$  of the gain medium. It is defined as

$$\sigma_g(\lambda) = A(\sigma_{ems}(\lambda) + \sigma_{abs}(\lambda)) - \sigma_{abs}(\lambda) \quad (4.3)$$

with the inverted fraction  $A$  as a measure of the population inversion level. It is dependent on the dopant ion density in the gain medium  $N$  and its excited fraction  $n_e$  by

$$A = \frac{n_e}{N}. \quad (4.4)$$

Considering an initial fluence  $J_{i-1}$  propagating through the gain medium, the amplified or attenuated spectral fluence  $J_i$  can be calculated as [Kro16a]

$$J_i(\lambda) = J_{sat}(\lambda)T(\lambda) \ln \left( 1 + G(\lambda) \left( \exp \left( \frac{J_{i-1}(\lambda)}{J_{sat}(\lambda)} \right) - 1 \right) \right) \quad (4.5)$$

with the saturation fluence

$$J_{sat}(\lambda) = \frac{hc}{\lambda(\sigma_{abs}(\lambda) + \sigma_{ems}(\lambda))}. \quad (4.6)$$

Equation (4.5) considers a spectrally dependent transmission loss  $T(\lambda)$ ,  $h$  is Planck's constant and  $c$  represents the vacuum speed of light. Note that in multipass amplifiers the saturation energy, which is characteristic for the gain medium, is an important parameter strongly affecting the system design as it represents the seed energy required to reduce the gain from its initial value to  $1/e$  ( $\sim 37\%$ ). Instead of updating the gain as can be found in

the classical expressions, we update the inverted fraction  $A$  as follows:

$$A_i = A_{i-1} - \frac{\int \left[ \lambda \left( \frac{J_i(\lambda)}{T(\lambda)} - J_{i-1}(\lambda) \right) \right] d\lambda}{hclN}. \quad (4.7)$$

For kHz repetition rates, thus, long continuous wave pumping processes, we need to consider a correction term for the excited-state decay losses. KROETZ et al. [Kro16a] added a correction factor that is based on the inversion decay law [Sie86] after each pass of sliced pump fluence with

$$A_i^* = A_i \exp\left(-\frac{\Delta t}{\tau_f}\right), \quad (4.8)$$

where  $\tau_f$  is the upper laser level lifetime of the gain medium and  $\Delta t$  represents the duration of the pump interval. As the amplification process happens at much faster time scales, this correction can be neglected for the simulation of amplification. As proposed by GRAFENSTEIN et al. [Gra16], the crystal needs to be split into a number of  $m$  slices with thickness  $\delta z = l/m$  in order to consider the pump intensity depletion during its propagation through the gain medium. The inverted fraction is solved for every crystal slice independently which accounts for an inhomogeneous distribution of absorbed pump power and, in turn, steady-state gain. Here, the pump and signal beam diameter are additionally adapted for every slice corresponding to their beam properties. In this way, a detailed analysis of the beam sizes and their impact to the amplification process can be realized as increasing the pulse fluences is beneficial for the saturation of the gain in the amplifier. Furthermore, it is possible to determine the on-axis pulse peak intensity  $I_n$  seen by each slice  $n = 1 \dots m$ . Approximating the accumulated nonlinear phase shift (B-integral) in the gain medium is then straightforward according to Equation (3.6):

$$B = \frac{2\pi}{\lambda_0} \sum_{i=1}^m n_2 I_i \delta z. \quad (4.9)$$

B-integral values as high as  $\pi$ - $2\pi$  are considered to be critical for self-focusing, which potentially leads to a severely reduced beam quality, spectral broadening, or even the destruction of the amplifier gain medium [Bey04]. Note that the threshold for self-focusing in terms of the B-integral can only be a rough estimate as it actually depends on the conditions in which the accumulated nonlinear phase is collected by the pulse. The power level that exactly compensates spreading of the beam due to diffraction is called critical power  $P_{\text{crit}}$  [Koe06]:

$$P_{\text{crit}} = \frac{0.148 \cdot \lambda^2}{n \cdot n_2}. \quad (4.10)$$

Any power level in excess of  $P_{\text{crit}}$  may lead to catastrophic self-focusing if the length of the medium is greater than the self-focusing length [Koe06]

$$z_f = \frac{A_0}{\lambda} \left( \frac{P}{P_{\text{crit}}} - 1 \right)^{-1/2} \approx w_0 (2nn_2I_0)^{-1/2} \quad (4.11)$$

with  $A_0 = \pi w_0^2$  the beam area and  $I_0$  the intensity at the entrance of the Kerr-lens medium, respectively. Note that Equation (4.11) is only valid for an initially collimated beam with planar wavefront. The critical power  $P_{\text{crit}}$  and the self-focusing length  $z_f$  have a major impact on the design of crystal-based multipass amplifiers as these strongly limit the crystal length and the achievable pulse peak power. At a fixed wavelength the latter depends only on the crystal properties, in particular the linear and nonlinear refractive indices  $n$  and  $n_2$ , respectively. Hence, potential Ho-doped crystals with appropriate mechanical and optical properties need to be found.

### 4.3 Properties of holmium-doped crystals

Besides Tm-doped crystals [Wal98] and some transition metal-doped materials such as chromium-doped zinc sulfide [Sor02] or zinc selenide [Mir15; Sor10], Ho-doped crystals have established for direct emission in the 2  $\mu\text{m}$  wavelength range. While Tm-based laser sources with spectral emission around 1.9  $\mu\text{m}$  are prone to water vapor absorption in the atmospheric propagation [Geb15b], the lasing wavelengths of Ho-doped crystals are slightly red-shifted towards 2.1  $\mu\text{m}$  depending on the host material. The choice of appropriate laser crystal is critical as the effective gain bandwidth has to fit the specific lasing wavelength of the Ho-doped fiber-based ultrashort pulse oscillator at 2.05  $\mu\text{m}$ .

Figure 4.1 summarizes the emission cross section versus wavelength of Ho-doped crystals with different host materials. While Ho-doped yttrium aluminum garnet (YAG) and lutetium oxide (LuO) are isotropic crystals, Ho-doped YLF and yttrium orthovanadate (YVO) are uniaxial, with the emission and absorption cross sections dependent on the polarization orientation with respect to the crystallographic axes. In terms of the spectral combinability, Ho:YLF (polarized  $\vec{E} \parallel c$ ) and Ho:YVO (polarized  $\vec{E} \parallel c$ ) seem to be best suited for the amplification of 2.05  $\mu\text{m}$  wavelength. Ho:YAG and Ho:LuO have their strongest emission at 2.09  $\mu\text{m}$  and 2.12  $\mu\text{m}$ , respectively.

A more detailed summary of the most important physical properties of the different host materials is given in Table 4.1. For high-power applications, isotropic crystals are prone to depolarization losses originating from thermally induced birefringence. Intrinsically birefringent crystals such as Ho:YLF or Ho:YVO are advantageous in comparison to Ho:YAG and Ho:LuO. In addition, in the case of Ho:YLF the thermal coefficient of the refractive index  $dn/dT$  is rather low and negative counteracting the effect of self-focusing or stress-induced focusing. The nonlinear refractive index  $n_2$  is another critical parameter, which strongly influences the design of CPA-free amplifiers as mentioned before. Ho:YLF exhibits

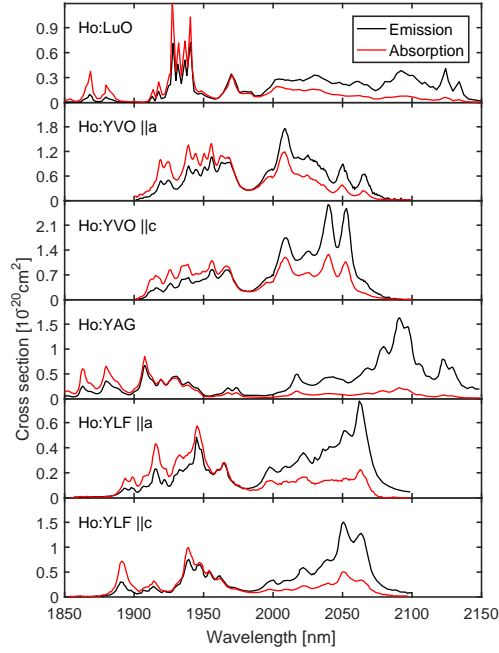


**Figure 4.1:** Emission (black) and absorption (red) cross section of various holmium-doped crystals, which are commonly used in laser systems with emission around  $2\ \mu\text{m}$ , digitized from [Gol02; Koo12; Kwi09; Wal98]. Note that the ordinate is scaled according to the different cross section values.

the lowest value and is almost an order of magnitude lower compared to Ho:YVO. As a consequence, nonlinear effects such as self-focusing have a higher threshold as represented by the critical power. Based on the material properties of Ho:YLF, Equation (4.10) yields  $24.9\ \text{MW}$ , which is the highest value among all potential candidates. Another advantage of Ho:YLF is its long fluorescence lifetime in the range of 14 to 16.1 ms. Long storage times are necessary, especially, for the amplification towards high-energy pulses at low pulse repetition frequencies in the kHz regime. On the other hand, the saturation fluence is of major importance as a low value indicates potential to extract most of the stored energy in the gain medium with low seed pulse energy. In the case of multipass amplification, this results in less passes through the crystal until the amplifier is saturated. In terms of the saturation energy, Ho:YLF ( $\vec{E} \parallel c$ ) and Ho:YVO ( $\vec{E} \parallel c$ ) are the most suitable candidates. Based on this evaluation and the commercial availability, Ho:YLF crystals have been chosen for the amplification of ultrashort pulses in a linear amplifier design. Note that Ho:YVO is an alternative candidate for the amplification of ultrashort low-energy pulses, especially, due to the lowest saturation fluence and the possibility to use the same pump and seed sources when exploiting the emission peak around  $2050\ \text{nm}$  (see Figure 4.1). However, the threshold for catastrophic self-focusing is comparably low and the commercial availability is currently very limited.



**Table 4.1:** Mechanical and spectroscopic properties of different holmium-doped crystals [Ada89; Agg05; Bre89; Cas75; Koo12; Lag05; Li11; Mil77; Pay92; Sha69; Wal98; Web03; Zel10; Zel98]. The saturation fluence has been calculated based on Equation (4.6) with the data from Figure 4.1 at the specified main emission wavelength. Note that the literature values for the nonlinear refractive index  $n_2$  are only valid at the specified wavelength. However, for a rough comparison these values are sufficient as the dispersion of the refractive index from one frequency  $\omega$  to its second harmonic  $2\omega$  is barely 10% [Ada92].

Physical properties	Lu <sub>2</sub> O <sub>3</sub>	Y <sub>3</sub> Al <sub>5</sub> O <sub>12</sub>	YLiF <sub>4</sub>	YVO <sub>4</sub>
acronym	LuO	YAG	YLF	YVO
lattice	cubic	cubic	tetragonal	tetragonal
density [g/cm <sup>3</sup> ]	9.42	4.56	3.99	4.23
thermal conductivity [W/(m K)]	12.8	8.8–12.9	5.3   a 7.2   c	5.1   a 5.2   c
th. coeff. refractive index [10 <sup>-6</sup> /K]	9.1	7.8	-4.6   a -6.6   c	3.9   a 8.5   c
refractive index at 2 $\mu$ m	1.896	1.801	1.443   a 1.465   c	1.961   a 2.169   c
nonlinear refractive index [10 <sup>-16</sup> cm <sup>2</sup> /W]	8.5 at 0.53 $\mu$ m	6.2 at 1.06 $\mu$ m	1.72 at 1.06 $\mu$ m	15 at 1.08 $\mu$ m
transparency range [ $\mu$ m]	0.225–8	0.21–5.2	0.12–8	0.35–4.8
fluorescence lifetime [ms]	10	7.8–10.6	14–16.1	4.1
main emission wavelength [nm]	2124	2090	2063   a 2050   c	2007   a 2040   c
saturation fluence [J/cm <sup>2</sup> ]	19.7	5.1	9.7   a 4.8   c	3.4   a 2.5   c
critical power [MW]	4.1	5.8	24.9	2

In Figure 4.2(a) the energy level diagram of the Ho-ion doped in YLF is schematically depicted. Analogous to the efficient in-band pumping concept of Ho-doped silica fibers, Ho:YLF is commonly pumped by 1940 nm into the excited-state <sup>5</sup>I<sub>7</sub>. This transition can be addressed by high-power commercially available Tm-fiber lasers with linearly polarized output ( $\vec{E} \parallel c$ ). In addition, Ho:YLF exhibits a second, yet smaller absorption peak around 1890 nm. The cross section as shown in Figure 4.2(b) is more structured than the one of holmium-doped silica fibers, which in turn yields less gain bandwidth of only a few nm around the main emission wavelength at 2050 nm. Figure 4.3(a) shows the fluorescence spectrum of a 20 mm long Ho:YLF crystal with doping concentration of 1.5 at.% for the two principal polarization directions parallel to the crystallographic axes, respectively. The experimental results coincide with the data obtained from literature in Figure 4.1.

In Figure 4.3(b) the calculated effective gain cross section of Ho:YLF for different inverted fractions  $A$  is depicted. It is obvious that the maximum inverted fraction of about 55% for 1940-nm pumping can be achieved representing full gain saturation at the pump wavelength.

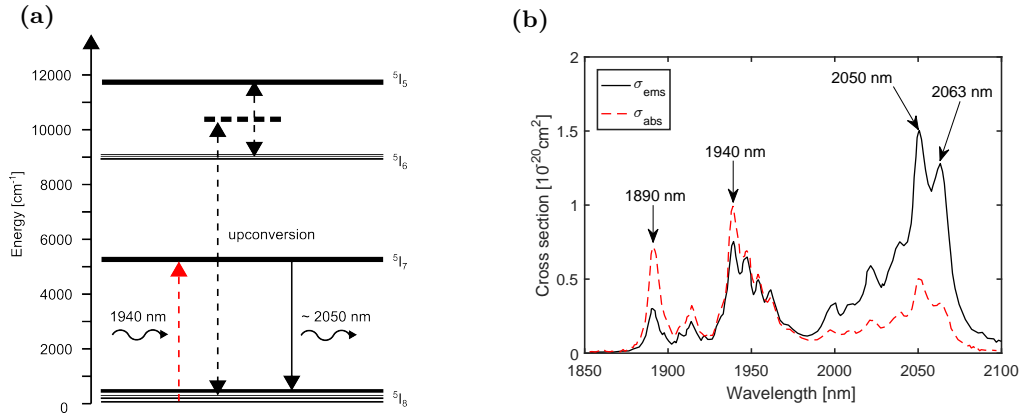


**Figure 4.2:** (a) Schematic energy level diagram with the most important transitions and (b) the corresponding emission and absorption cross sections of Ho:YLF for  $\vec{E} \parallel c$  (digitized from [Wal98]).

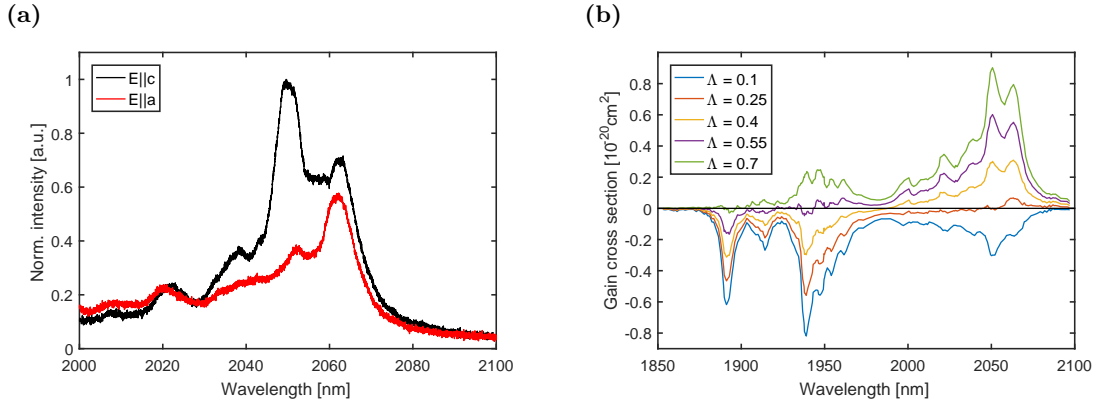


**Figure 4.3:** (a) Fluorescence spectrum of a 1.5 at. % doped Ho:YLF sample excited at a wavelength of 1940 nm and (b) effective gain cross section of Ho:YLF in the case of  $\vec{E} \parallel c$ .

Interestingly, even higher inverted fractions of up to about 60 % seem to be possible for 1890-nm pumping, which can offer a higher small-signal gain. The 1890 nm pump radiation can be realized either in Tm-fiber lasers or by means of the specific emission of Tm:YLF crystals ( $\vec{E} \parallel c$ ) [Str13].

For CPA-free ultrashort pulse amplifiers, one of the most important crystal parameters is the laser-induced damage threshold (LIDT). This value can either be related to a pulse fluence given in  $\text{J}/\text{cm}^2$ , or to the peak intensity given in  $\text{GW}/\text{cm}^2$ . While the applied pulse duration is already considered in the peak intensity ( $I_{\text{LIDT}} \propto E_p/\tau$ ), the fluence is only dependent on the pulse energy ( $J_{\text{LIDT}} \propto E_p$ ). Whether the LIDT is related to the peak intensity or the pulse fluence strongly depends on the applied pulse duration, the pulse repetition frequency, and the material properties such as crystal quality, additional doping, or dielectric coatings. This topic becomes even more complicated when considering

the damage mechanism (e.g. thermal and stress-induced damage or self-focussing and laser-induced breakdown) and its location, which can be in the bulk or at an interface of two different media (e.g. air to crystal). LIDT values in YLF crystals with ultrashort pulse irradiation at  $1 \text{ ps} < \tau_p < 10 \text{ ps}$  are not found in scientific literature and a detailed analysis of the LIDT is not part of this thesis, as well. Nevertheless, some crystal manufacturers specify the YLF LIDT to be around  $15 \text{ J/cm}^2$  at  $10 \text{ ns}$ . It is well-known that the breakdown threshold is dependent on the pulse duration. According to the empirical square-root scaling law  $J_{\text{LIDT}} \propto \sqrt{\tau_p}$  [Bet76], this yields a damage threshold of roughly  $0.34 \text{ J/cm}^2$  for a pulse duration of  $5 \text{ ps}$ . However, this relation might not hold for pulse durations of  $< 10 \text{ ps}$ , and different results have been shown from monotonically decreasing [Len98; Stu95; Tie99; Var96] to even increasing LIDTs [Du94] when approaching the femtosecond range. In fact, previous experiments with Ho:YLF revealed bulk damage as well as damage to the coatings at the threshold of roughly  $1.5 \text{ J/cm}^2$  ( $5 \text{ ps}$ ). In order to avoid the destruction of the material, a considerably lower pulse fluence should be applied.

Next to damage-related considerations, the gain material in ultrashort pulse CPA-free multipass amplifiers has to satisfy further requirements whose combination can be rather challenging. On the one hand, short crystals are advantageous leading to small interaction lengths between the intense radiation with the gain medium. In combination with a tailored beam radius inside the crystal, nonlinearities such as self-focusing can be mitigated. However, efficient energy extraction is achieved only for proper seed pulse fluences close to the saturation fluence of the particular laser material. Hence, small beam sizes are required, which is counteracting the aforementioned nonlinear issues. At the same time, a special attention has to be focused on the laser-induced damage threshold as the prevalent ultrashort pulses are amplified to high pulse peak intensities. In order to maintain high gain factors, appropriate doping levels can be applied. However, Ho-doped materials suffer from upconversion effects. This deleterious process sets an upper limit for the doping concentration in Ho-doped gain media, which is typically on the order of  $0.5 \text{ at.}\%$ , rarely up to  $1 \text{ at.}\%$ .

Figure 4.2(a) has already shown the non-resonant upconversion process, at which two closely located Ho ions in the  $^5\text{I}_7$  manifold interact to promote one of them to the  $^5\text{I}_5$  or  $^5\text{I}_6$  and to demote the other to the  $^5\text{I}_8$  manifold. This parasitic process is most prominent, when the doping concentrations and the excitation intensities are high leading to a high population density in the  $^5\text{I}_7$  upper-state laser level. The process manifests itself in a quenched fluorescence lifetime of the excited state and can be visualized by a non-exponential decay of the fluorescence intensity.

First attempts to quantify the Ho:Ho upconversion have been carried out by BARNES et al. [Bar03] in 2003 with a quantum-mechanical model. They investigated the Ho:Ho upconversion energy-transfer parameters in different host crystals including Ho-doped YLF. Due to difficulties to determine values for low concentrations, investigated doping levels started at  $1 \text{ at.}\%$  (even  $2 \text{ at.}\%$  in the case of Ho:YLF). As mentioned before, high doping concentrations are one of the prerequisites for ultrashort pulse CPA-free multipass amplifiers and it is of major importance to get a rough estimate for the impact of upconversion

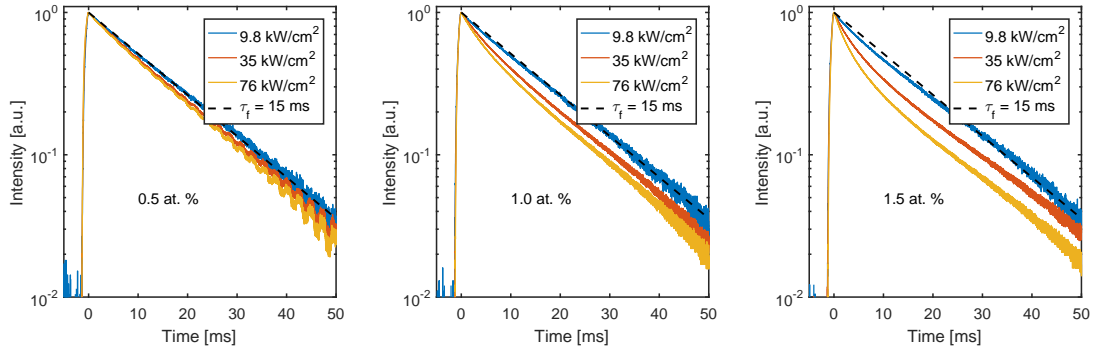


**Figure 4.4:** Normalized fluorescence decay in Ho:YLF at different excitation intensities. The black dotted line represents the literature value for the upper-state lifetime with 15 ms [Pay92; Wal98].

losses in the laser system. Thus, the excited-state fluorescence lifetime of the transition  ${}^5I_7 \rightarrow {}^5I_8$  was analyzed. The results are summarized in Figure 4.4 showing the normalized fluorescence decay after excitation with different intensities. Several a-cut Ho-doped YLF samples with lengths of 20 mm were investigated with doping concentrations between 0.5 and 1.5 at.%. Each sample was excited by a pump source at a wavelength of 1940 nm with linear polarization parallel to the c-axis. Its continuous emission was mechanically chopped. For comparison reasons, a fluorescence decay reference (black dotted line) with a literature value of 15 ms [Pay92; Wal98] is given.

The samples with 0.5 at.% doping concentration show an exponential decay, which exhibits only weak dependence on the excitation intensity. In contrast, the fluorescence at higher doping concentrations in combination with increased excitation intensities decays in a non-exponential form within the first few milliseconds. In order to roughly quantify the quenching effect, the upper-state lifetime  $\tau_f$  was obtained by fitting an exponential decay in the time period between 0 and 5 ms. In Table 4.2 the results are summarized. Note that an exponential fit is only valid for the rather weak excitation ( $9.8 \text{ kW/cm}^2$ ). Nevertheless, fitting the non-exponential curve within a small time frame of only 5 ms approximates with the experimental data and allows to properly compare the results.

**Table 4.2:** Measured excited-state fluorescence lifetime of different Ho-doped YLF crystal samples.

Excitation intensity [ $\text{kW/cm}^2$ ]	0.5 at. %	1.0 at. %	1.5 at. %
9.8	14.6 ms	13.6 ms	11.9 ms
35	12.8 ms	9.8 ms	7.6 ms
76	12.1 ms	8.4 ms	5.7 ms

As mentioned above, the calculated upper-state lifetime of 14.6 ms at low 0.5 at.% doping concentration and weak excitation intensity agrees with literature data found in [Pay92; Wal98]. At high excitation intensity ( $76 \text{ kW/cm}^2$ ) the lifetime is quenched to 12.1 ms, 8.4 ms, and 5.7 ms for doping concentrations of 0.5, 1.0, and 1.5 at.%, respectively. These results are considered in the numerical model introduced in Section 4.2 via Equation (4.8) in all following simulation results.

Another important design criterion for ultrashort pulse amplifiers is the absorption in the gain medium. Two different pump wavelengths were investigated: 1890 nm and 1940 nm. A maximum pump power of 4 W corresponds to an intensity of  $35 \text{ kW/cm}^2$ . The pump absorption in dependence on the launched pump power is presented in Figure 4.5 for the three Ho:YLF samples with doping concentrations from 0.5 up to 1.5 at.%. There is no significant difference between the two different pump wavelengths. One can clearly see a bleaching effect for all three doping concentrations resulting in a reduced pump absorption of about 10 %, 30 %, and 50 % for high excitation intensities, respectively.

These results show that, particularly in the small-signal gain regime with vanishing gain depletion, one pass through the gain medium is not sufficient to absorb most of the available pump power. By geometrically folding the beam several times through the gain medium the crystal length is virtually multiplied giving rise to the overall system efficiency. However, there will be a certain limit, at which the pump power is not sufficient to induce inversion over the full propagation length. In holmium-doped YLF crystals this will lead to re-absorption of the amplified signal, thus, a reduction of the achievable pulse energy and efficiency. The optimum amount of passes in a multipass amplifier especially depends both on the applied pump power and on the crystal parameters such as length and doping concentration.

As tens or even hundreds of passes through a crystal in a multipass amplifier are not practical, only few passes with sufficient gain per pass are required to achieve a high

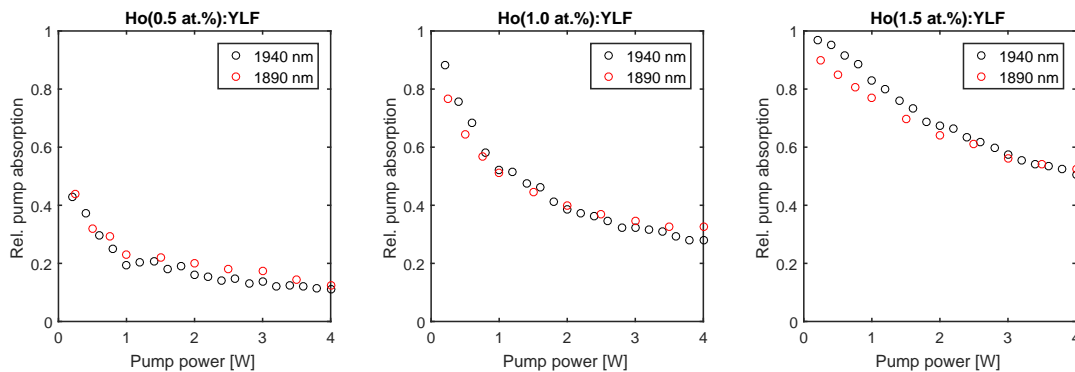


**Figure 4.5:** Continuous wave pump absorption in 20 mm long Ho:YLF crystals at different wavelengths of 1890 nm and 1940 nm. The linear polarization has been orientated along the c-axis. The maximum pump power of 4 W corresponds to an intensity of  $35 \text{ kW/cm}^2$ .

overall gain factor. In order to investigate the amplification potential of the Ho-doped YLF crystals, the small-signal single-pass gain was measured. In this amplification regime the energy storage is high, which additionally reveals the impact of negative effects such as upconversion losses. Three 20 mm long Ho:YLF samples with doping concentrations ranging from 0.5 to 1.5 at.% were investigated. These crystals were seeded by 5.8-ps pulses centered at a wavelength of 2051 nm. The seed pulse energy was set to 8.5 nJ at a pulse repetition frequency of 100 kHz. Different pump wavelengths of 1940 nm and 1890 nm were applied. The single-pass gain was measured with increasing pump power up to 4 W, which corresponds to a maximum pump intensity of  $35 \text{ kW/cm}^2$  in the focal area inside the investigated crystals.

The experimental results are shown in Figure 4.6 for different Ho doping concentrations (circles). In addition, the results of numerical simulations (dashed lines) are added, which agree well with the experimental data. At certain pump power levels the 1890-nm pumping scheme outperforms the conventional pump wavelength at 1940 nm. This specific pump level shifts towards higher power as the doping concentration is increased. This can be explained by the higher inversion level achieved as described earlier in this section. The maximum inversion level for 1940-nm pumping is about 55 % in Ho:YLF. In contrast, about 60 % inverted fraction can be achieved with pumping at 1890 nm. However, in order to reach such high inversion levels close to gain saturation along the full propagation length inside the amplifier medium, sufficient pump power is required. Up to the highest pump power the small-signal single-pass gain could be improved by a factor of 1.42, 1.39, and 1.29 for the doping concentrations of 0.5, 1.0, and 1.5 at.%, respectively. The experiment proves on the one hand that doping concentrations up to 1.5 at.% are still applicable in amplifiers based on holmium-doped crystals. On the other hand, the direct comparison of the two different pump wavelengths revealed that the non-classical 1890-nm pumping scheme shows beneficial characteristics, which might be interesting for high-gain multipass amplifiers.

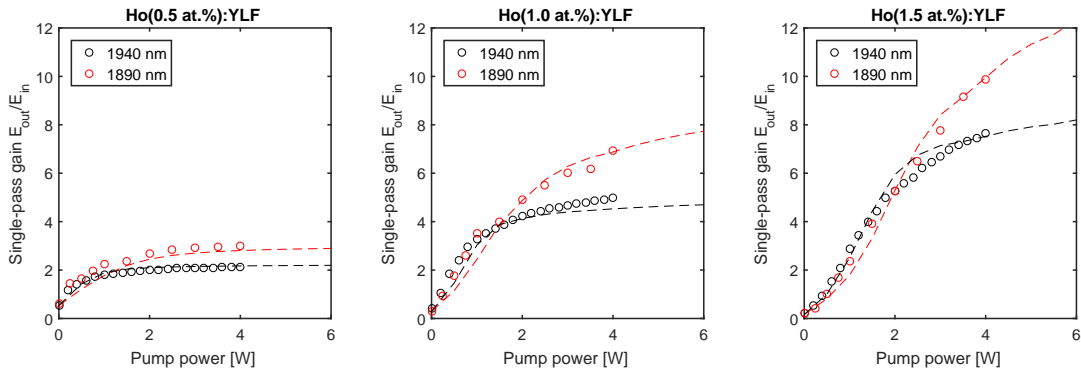


**Figure 4.6:** Single-pass small-signal gain in 20 mm long Ho:YLF crystals at different wavelengths of 1890 nm and 1940 nm: experimental data (circles) and numerical simulation (dotted lines).

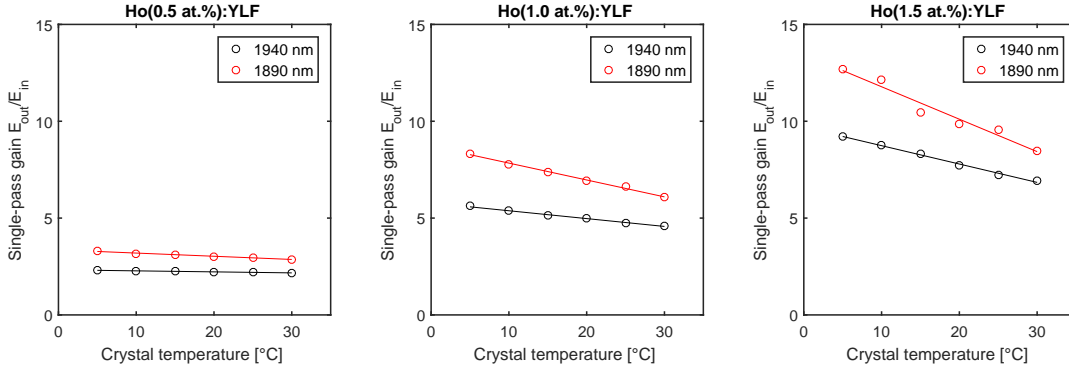


**Figure 4.7:** Single-pass small-signal gain in 20 mm long Ho:YLF crystals at different wavelengths of 1890 nm and 1940 nm versus the crystal temperature: experimental data (circles) and linear fit (solid lines).

It is well-known that in quasi-three-level gain media the thermal population of the lower laser level strongly influences the gain cross section, which results in some re-absorption loss in an unpumped gain medium. Reducing the degree of re-absorption at the lasing wavelength can be achieved by proper cooling of the laser crystal. In recent years, cryogenically-cooled booster amplifiers [Hem15] and Q-switched oscillators [Fon13] based on Ho:YLF have been used in the 2  $\mu\text{m}$  spectral region up to the mJ-level of pulse energy. Figure 4.7 shows the single-pass small-signal gain in dependence of the crystal temperature. It can be seen that rather low temperature differences can lead to significant improvements in terms of the gain factor. Additionally, the slope is the strongest for highest doping concentrations of 1.5 at.%. However, HEMMER et al. [Hem15] have shown that the re-absorption in Ho:YLF at the emission wavelength vanishes only at temperatures of liquid nitrogen. Under cryogenically cooling, Ho:YLF can be considered to feature a four-level behavior at the expense of an increased setup complexity due to the crystal mounted on a cold finger, which is placed in a vacuum chamber. Thus, cryogenic cooling was not considered for the system design.

However, there is another detrimental effect in high-power lasers, which is strongly related to the temperature distribution during operation. End-pumped amplifier architectures based on bulk gain media are prone to thermal lensing. The focal length of a thermal lens can be approximated by only considering the temperature-dependent change of the refractive index  $dn/dT$ . An analytical solution assuming a radial heat flow originating from a Gaussian pump beam has been derived by INNOCENZI et al. [Inn90]:

$$\frac{1}{f} = \frac{1}{2 \cdot \kappa} \cdot \frac{dn}{dT} \cdot \frac{P_{\text{heat}}}{A} = \frac{1}{2 \cdot \kappa} \cdot \frac{dn}{dT} \cdot \frac{P_p \cdot (1 - e^{-\alpha l})}{A}, \quad (4.12)$$

with the beam area in the focus  $A$ , the thermal conductivity  $\kappa$ , and the dissipated average power in the crystal  $P_{\text{heat}}$  depending on the incident pump power  $P_p$  and the intrinsic material absorption coefficient  $\alpha$ . In order to investigate the thermal lens in Ho:YLF



crystals, a simple pump-probe experiment was conducted. A 20 mm long Ho(1.5%):YLF crystal was pumped by a collimated beam at a wavelength of 1940 nm with up to 10 W of continuous wave power. The polarization of the pump laser was set to  $\vec{E} \parallel c$  according to the highest absorption efficiency. A collimated probe beam at a center wavelength of 976 nm was used to probe the generated thermal lens in the crystal, which was mounted in a temperature stabilized (20 °C) copper mount. The temperature distribution in the Ho:YLF crystal was measured with a thermal imaging camera. It is shown in Figure 4.8(a) at maximum pump power, indicating a temperature difference between the copper mount and the on-axis beam position of about 20 °C. The recorded probe beam waist deviation in dependence on the pump power level corresponds to a certain focal length of the thermal lens. Figure 4.8(b) shows the experimental results in comparison to the calculated values according to Equation (4.12) assuming that about 70 % of the absorbed pump power are transferred to heat in the crystal.

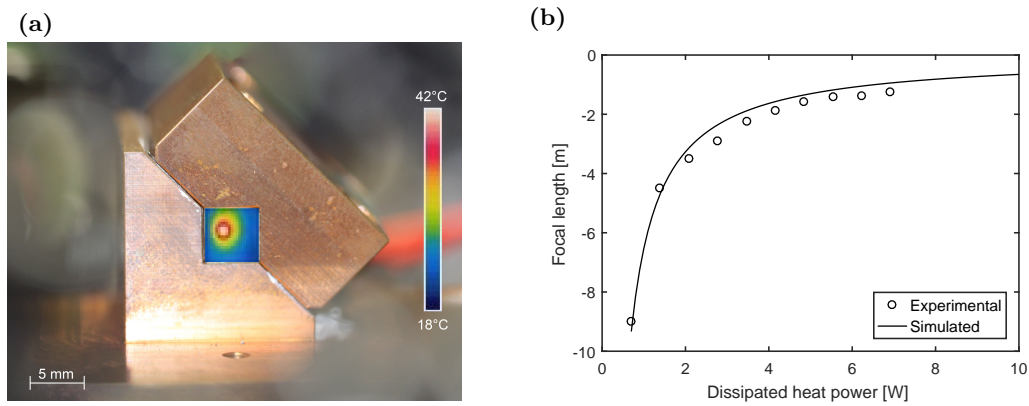


**Figure 4.8:** (a) Temperature profile of the pumped spot in the crystal at maximum pump power of 10 W with an on-axis maximum of about 40 °C. (b) Thermal lensing in an end-pumped Ho:YLF laser crystal depending on the absorbed pump power. The simulated values are based on the Ho:YLF thermo-mechanical properties as summarized in Table 4.1.

Equation (4.12) suggests that the focal length scales with  $1/w^2$ . However, a larger beam size is more sensitive to thermal lensing, which exactly compensates the advantage of a reduced focal length due to an enlarged beam. For an applied pump beam waist radius of 950  $\mu\text{m}$  the focal length is in the range of several meters. The thermal lens is concave indicating that the negative thermal coefficient of the refractive index is not overcompensated by stress-induced focusing effects. Typically, the low quantum defect in in-band pumped Ho:YLF crystals results in rather low dissipated power. However, it has been shown that at sufficient doping concentrations lifetime quenching and upconversion processes may occur. This leads to some uncertainty, since such effects can substantially contribute to the heating of the crystal. The experimental investigations into optical properties of (highly doped) Ho:YLF show that these crystals are well-suited for the amplification of ultrashort pulses towards high pulse energies not only in CPA-based RAs, but also in CPA-free multipass amplifiers as will be presented in the following sections.



#### 4.4 CPA-free multipass amplification in Ho:YLF

The previous investigations were incorporated into the design and construction of a MW-level peak power laser system with emission around  $2\ \mu\text{m}$ , which will be presented in this section. Furthermore, this section is supported by numerical simulations as introduced in Section 4.2. In all simulations the pre-amplifier characteristics (see Section 3.5) such as optical power spectrum, pulse energy, and pulse repetition frequency serve as parameter input. Due to the beneficial thermo-mechanical properties of Ho:YLF with a low negative thermally-induced change of the refractive index  $dn/dT$  and a low quantum defect of less than 7% between the pump and signal wavelength, thermal lensing has been neglected in developing the design. A vanishingly low thermal lensing effect in the 20 mm long Ho:YLF crystals was confirmed in previously presented experiments.

The experimental setup is shown in Figure 4.9. The stretched-pulse mode-locked fiber oscillator with subsequent fiber-based pre-amplifier was used for the seed pulse generation. A detailed characterization of this laser system has been presented in the previous Chapter 3 indicating operation parameters, which are perfectly suited to fit the spectral requirements of the Ho:YLF crystals. The output pulse energy was set to 25 nJ, which corresponds to an average power of 500 mW at a fundamental pulse repetition rate of 20 MHz. This power level was chosen according to the maximum input power handling of the subsequent AOM pulse picker (AA Opto-Electronic), which was specified by the manufacturer to

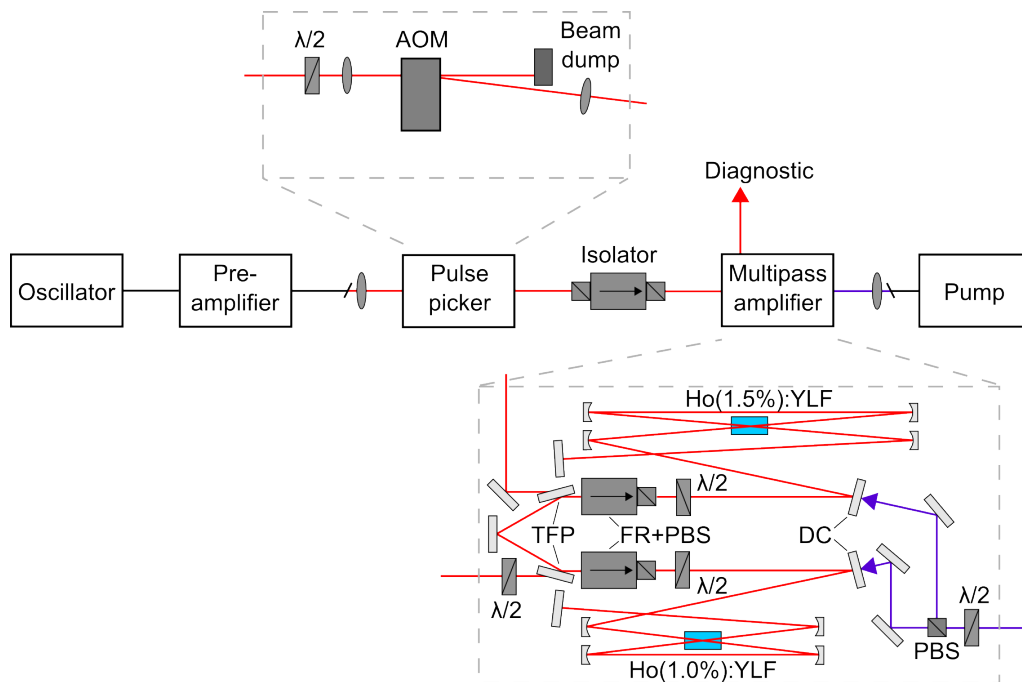


**Figure 4.9:** Experimental setup of the multipass amplifier system. AOM: acousto-optic modulator, TFP: thin-film polarizer, FR: Faraday rotator, PBS: polarization beam splitter, DC: dichroic mirror,  $\lambda/2$ : half-wave plate.

5 W/mm<sup>2</sup>. The trigger port of the pre-amplifier was used to detect the pulse train for proper electrical synchronization of the AOM pulse picker and the seed source. In order to achieve sufficient rise and fall time similar to the pulse-to-pulse temporal distance of 50 ns, the beam was focused into the commercial AOM module. It consisted of a TeO<sub>2</sub> crystal, in which an ultrasonic acoustic wave was excited with a frequency of 80 MHz. A half-wave plate was used to rotate the linear polarized beam to achieve highest diffraction efficiency into the first order, which amounts to about 55%. An optical isolator with about 90% transmission at 2050 nm was used to protect the fiber-based seed source from back reflections. Considering the pulse picker efficiency and the insertion losses of the following optical components, about 8.5 nJ of pulse energy were available for seeding the multipass amplifier. The latter can be split into two almost identical stages, each providing four passes through a 20 mm long a-cut Ho:YLF crystal with a quadratic aperture of 5x5 mm. This was achieved by geometrically folding the beam twice through the gain medium in each stage and back reflection such that another two passes sum up to an overall number of four. Both crystals were anti-reflexion coated for the pump and signal wavelength of 1940 nm and 2050 nm, respectively. They were wrapped in indium foil and mounted in a copper mount, which was thermally stabilized by a thermoelectric cooler to 18 °C. The first stage consisted of a Ho:YLF crystal which exhibited 1.0 at.% holmium doping concentration. The copropagating pump and signal beams were combined via a dichroic mirror and focused to a beam diameter inside the crystal of 180 μm 1/e<sup>2</sup> width. The collimation lens behind the AOM pulse picker was chosen such that the beam was mode-matched with the pump beam in the multipass amplifier.

The Ho:YLF crystal in the second stage exhibited the same geometrical dimension, but a higher doping concentration of 1.5 at.%, and a larger beam size of 220 μm was chosen. This was achieved by spherical mirrors with a longer surface radius of 300 mm compared to the radius of 250 mm in the first stage. The multipass amplifier was working in standard laboratory environmental conditions at a room temperature of 20 °C. All spherical and planar mirrors provided high reflexion of > 99.99% in a broad spectral range covering both the pump and signal wavelength. Additionally, the dual-stage setup offered some advantages: First, the amplification factor per stage is lowered, keeping an overall high value. Since the two stages were separated by an optical isolator, this strategy mitigates self-lasing of the multipass amplifier as presented in [Hin18b]. The amplifier was pumped by a self-developed polarization maintaining Tm-fiber MOPA system delivering up to 17.4 W of linearly polarized output power at a center wavelength of 1939 nm. The pump beam was split by means of a half-wave plate and a polarizing beam splitter to provide pump power for both stages. A more detailed description of the pump source is given in the Appendix C.

In Figure 4.10(a) the achieved pulse energies as a function of the launched pump power for different pulse repetition frequencies are shown. The highest energy is LIDT-limited to 100 μJ and was achieved at repetition rates of 10 kHz and 50 kHz for pump powers of 7.5 W and 13.4 W, respectively. For pulse repetition frequencies of ≥ 100 kHz the maximum pulse energy was limited by the available pump power of 17.4 W only. Pulse energies up to 68 μJ at 100 kHz were achieved. At highest pulse repetition rate of 20 MHz the pulse energy

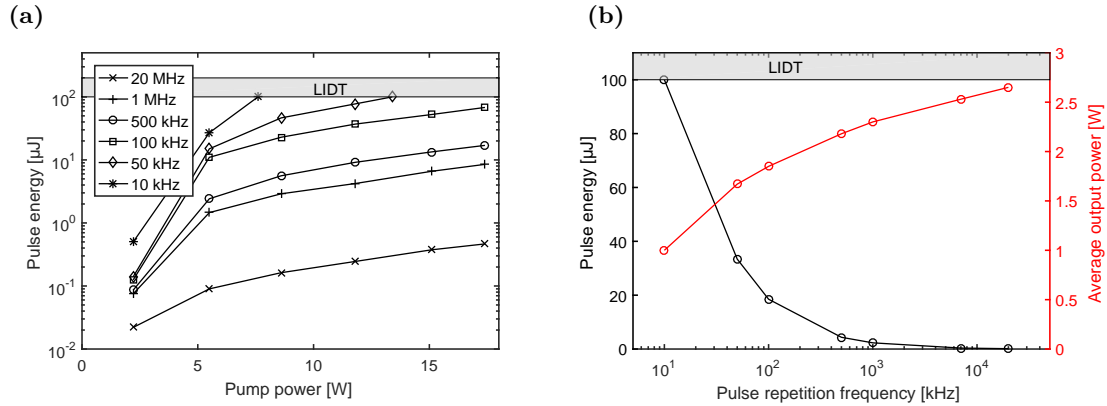


**Figure 4.10:** (a) Measured output pulse energy as a function of the launched pump power for different pulse repetition frequencies between 10 kHz up to 20 MHz and (b) at fixed pump power of 7.5 W limited by the damage threshold at the lowest pulse repetition frequency of 10 kHz.

was  $0.47 \mu\text{J}$ , which corresponds to an average output power of 9.3 W. In Figure 4.10(b) the evolution of the pulse energy and average output power as a function of the pulse repetition frequency at fixed pump power of level of about 7.5 W is presented. This pump power was chosen according to the LIDT-limited pulse energy at lowest repetition rate of 10 kHz. Highest optical output power was achieved at the maximum possible pulse repetition frequency of 20 MHz. In contrast, the pulse energy was strongly increasing for lower pulse repetition frequencies, which can be explained by the decreased gain depletion in steady-state.

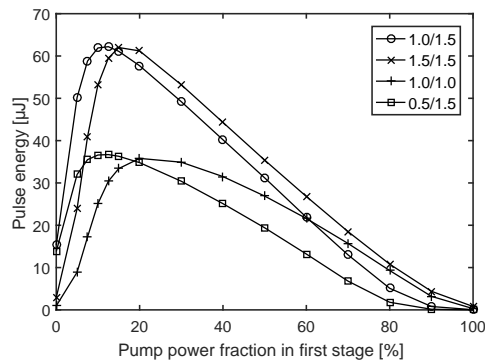


**Figure 4.11:** Simulation of different combinations of doping concentrations in a dual-stage amplifier (first stage/second stage) for a pulse repetition frequency of 100 kHz and a fixed maximum pump power of 18 W. The diagram shows the calculated pulse energy as a function of the used pump power in the first stage, while the remaining pump power is pumping the second stage. The numerical model is based on the final experimental setup considering the seed and pump properties as well as the Ho:YLF characteristics.

During all investigations the pump power splitting ratio between the two amplifier stages was kept constant at a value of 11 % launched into the first stage, which corresponded to an optimized operation at full pump power. This value coincides with the simulation results of the corresponding dual-crystal configuration of 1.0/1.5 at.%, which is shown in Figure 4.11 among additional doping combinations. In all cases the achievable pulse energy is maximized for a rather low pump power fraction used for the first amplifier stage of 5 to 20 %. This can be explained by the continuously increasing signal energy in the amplifier, which results in a higher seed energy in the second stage in comparison to the first stage. As more energy is extracted in the second stage, more pump power is required to store sufficient energy. Furthermore, the achievable pulse energy approaches 0 at 100 % launched into the first stage due to an entirely unpumped second stage re-absorbing the laser pulses. These numerical investigations verify that the chosen doping concentration combination in the dual-stage setup offers an optimized performance in terms of the achievable pulse energy in comparison to other configurations except for 1.5/1.5 at.%, which performs nearly similarly.

The pulse duration was measured with a commercial autocorrelator with a pulse width range of 50 ps. The autocorrelation traces at the maximum pulse energies for different pulse repetition frequencies are shown in Figure 4.12(a)-(d). The corresponding optical spectrum (inset) was measured with an optical spectrum analyzer with a resolution of 0.05 nm. For all pulse repetition frequencies and their maximum energies up to 100  $\mu$ J the pulse duration is smaller than that of the seed pulse. This beneficial pulse compression can be attributed to the spectral filtering effect of chirped pulses due to the finite gain bandwidth: The temporal intensity distribution of a highly chirped pulse follows its spectral shape. Gain narrowing therefore acts as an artificial compression as the temporal wings contain the spectral components which exhibit less gain than the central part of the pulse. In contrast, the Fourier-limited pulse duration increases due to the bandwidth loss. Note that this effect is most efficient, if the gain narrowing is symmetric, equally discriminating the spectral wings. The chirped-pulse spectral filtering scheme has been similarly proposed by MAMYSHEV [Mam98] for optical data regeneration.

To further compare the amplifier performance at different pulse repetition frequencies, the pulse energy was set to a constant value of 1  $\mu$ J and 10  $\mu$ J by proper selection of the pump power for each investigated repetition rate. Both the measured pulse duration and the Fourier-limited pulse width were nearly invariant. The (Fourier-limited) pulse duration for a 1- $\mu$ J pulse energy was about 3.6 ps (1.4 ps) and for a 10- $\mu$ J pulse it was about 3.5 ps (1.7 ps). These results verify the effect of temporal compression as introduced earlier. The higher pulse energies have the tendency of exhibiting slightly shorter pulse durations and at the same time a narrower FWHM spectral bandwidth, which can be attributed to the higher gain factors and in turn stronger gain narrowing of the chirped pulses in this case.

In order to confirm stable single-pulse operation without pre- or post-pulses, the amplified pulse train was measured with a 12.5 GHz photo diode in combination with a 6 GHz oscilloscope and a 26.5 GHz radio-frequency spectrum analyzer. Figure 4.13(a) shows the fundamental beat note in the radio-frequency spectrum for a pulse repetition frequency set

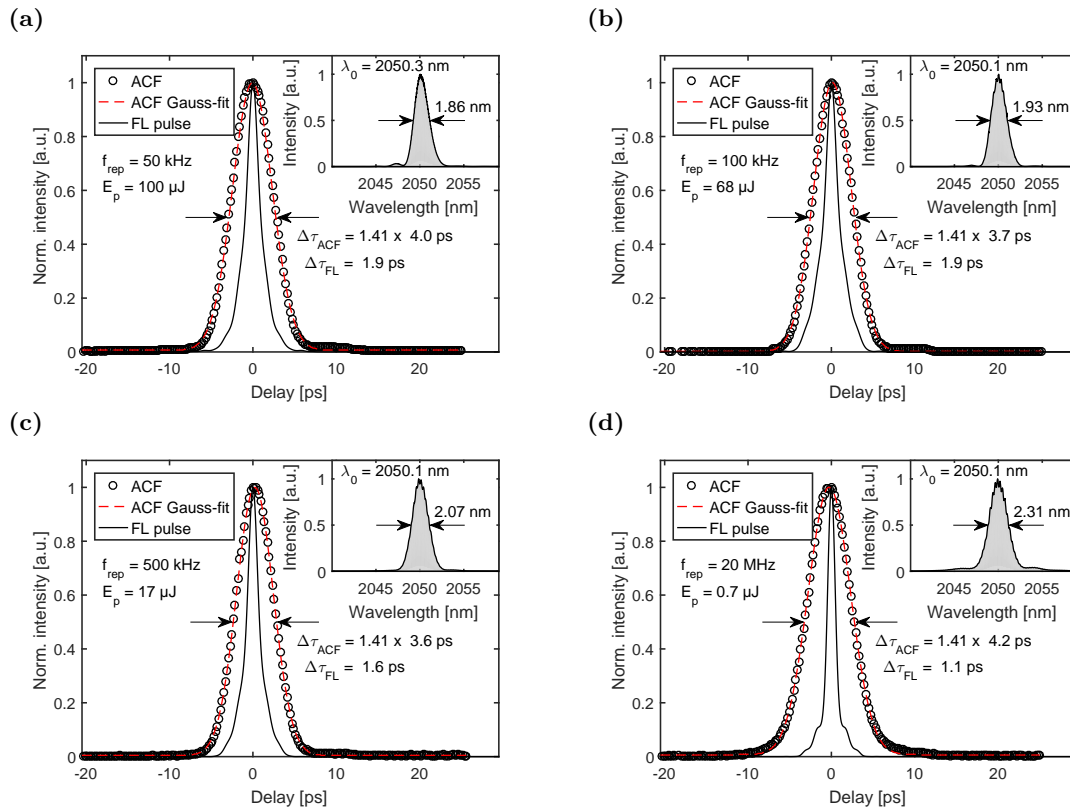


**Figure 4.12:** Measured autocorrelation traces (black circles) for different pulse repetition frequencies of (a) 50 kHz, (b) 100 kHz, (c) 500 kHz, and (d) 20 MHz at maximum achieved pulse energy assuming a Gauss-shaped pulse (red dotted line) as well as the calculated Fourier-limited pulse duration (black solid line) based on the corresponding optical spectrum (inset), respectively.

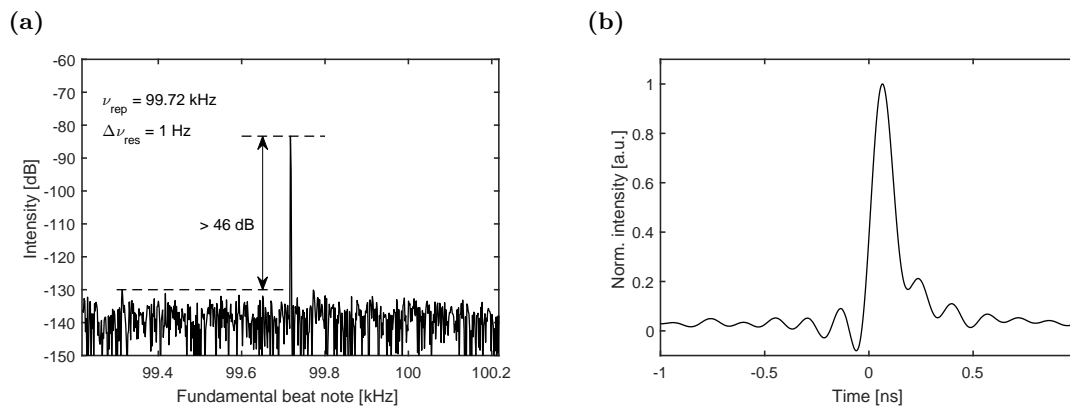


**Figure 4.13:** (a) Fundamental beat note of the 100 kHz amplified pulse train and (b) single pulse oscilloscope trace.

to about 100 kHz measured with a high resolution of 1 Hz. The signal is more than 46 dB above noise level indicating stable operation. In Figure 4.13(b) the oscilloscope signal for a single pulse is presented, which shows no signs of additional pre- or post-pulses within a temporal distance of 1 ns around the amplified pulse.

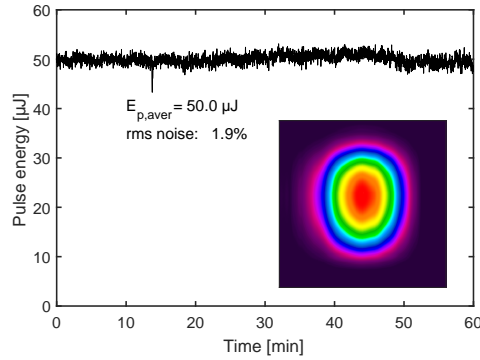


**Figure 4.14:** Long-term stability of the multipass amplifier at a pulse repetition frequency of 100 kHz. Inset: Corresponding far-field beam profile.

The long-term stability at a pulse repetition frequency of 100 kHz was investigated by measuring the average output power over a period of 1 h at a decent power level of 5 W, which corresponds to a pulse energy of 50  $\mu\text{J}$ . The results are shown in Figure 4.14. The root mean square power noise is below 2%. The corresponding far-field beam profile is depicted in the inset of Figure 4.14. The beam exhibits a slight elliptic profile. The measurement of the beam propagation parameter  $M^2$  yields a fitted value of 1.11 in the direction parallel and 1.09 perpendicular to the table (see Figure 4.15(a)). These results show that the beam quality did not significantly decrease in a multipass amplifier based on Ho:YLF compared to the pre-amplifier output depicted in Figure 3.13(a).

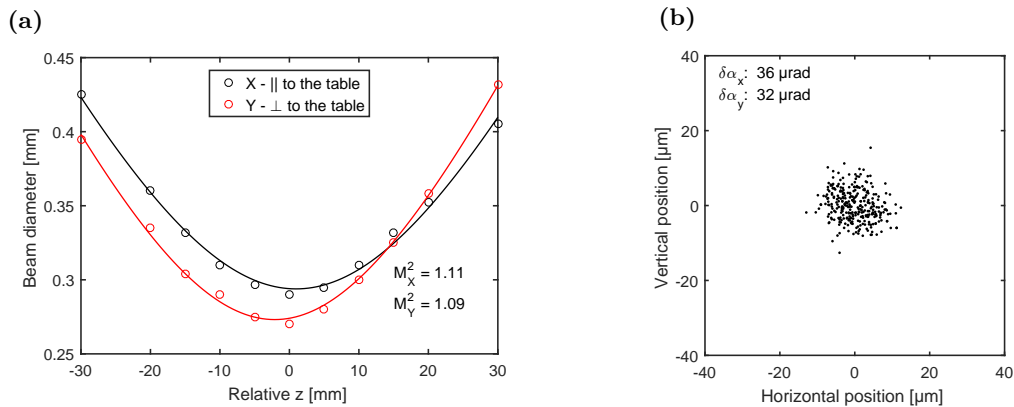


**Figure 4.15:** (a)  $M^2$  measurement at an average power of 5 W: measured data (circles) and fitted caustic (solid lines) according to Equation (3.13). (b) Pointing stability measurement over a period of 5 min.

The beam pointing is important for micromachining and materials processing applications. It was measured as described in Section 3.5. The results are shown in Figure 4.15(b) indicating an angular stability of  $36 \mu\text{rad}$  parallel (X) and  $32 \mu\text{rad}$  perpendicular (Y) to the optical table. Compared to the fiber-based pre-amplifier output characteristics (see Figure 3.13(b)), the pointing stability in Y-direction is almost unchanged, while it became worse by a factor of 2 in the case of the X-direction. The relative beam pointing considering the average focal waist is less than 2.8% for both directions.

#### 4.5 High-energy booster amplifier based on Ho:YLF

Simple single-pass booster amplifiers are easy to establish due to only few optical components that require alignment. However, the CPA-free amplification of sub-10 ps pulses towards the mJ-level pulse energies can be challenging even in such schemes. The high pulse peak intensities limited the accessible pulse energy in the past. Nevertheless, by carefully tailoring the beam propagation parameters as well as the properties of the gain medium, one can handle nonlinear effects and laser-induced damage. On the one hand, small beam diameters are beneficial to properly saturate the gain medium. On the other hand, the high intensities potentially damage the material. Long crystals can provide full pump power absorption and high gain factors, while a long light-matter interaction length can lead to self-focusing according to Equations (4.10) and (4.11). Here, the focus is on maximizing the pulse energy with a targeted pulse duration below 10 ps without the necessity of pulse compression and severe gain medium cooling efforts. The proposed design represents a very simplified, compact laser source, which generates high peak powers at the same time. Parts of this section were already published in [Hin18a].

The experimental setup of the booster amplifier is depicted in Figure 4.16. It was seeded from a multipass amplifier, whose pulse characteristics in terms of the spectral FWHM bandwidth and pulse duration were slightly different from those presented in the previous

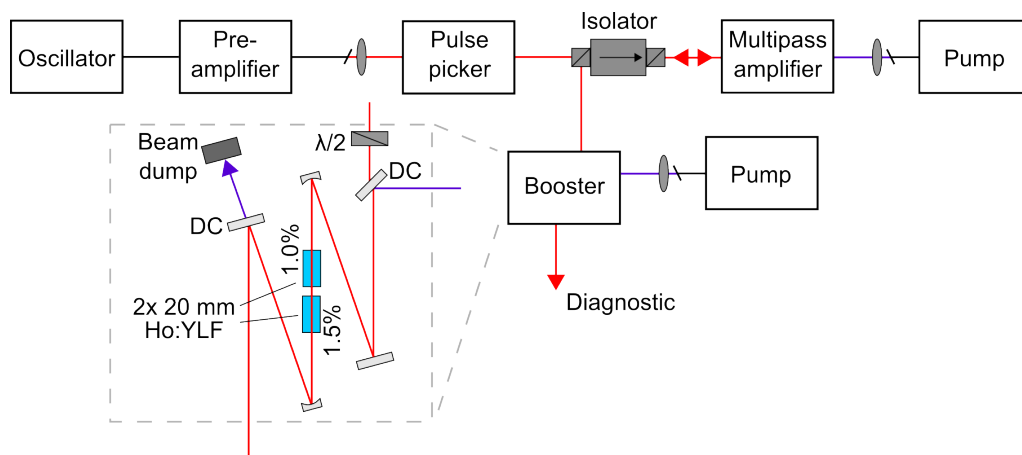


**Figure 4.16:** Experimental setup of the booster amplifier. DC: dichroic mirror,  $\lambda/2$ : half-wave plate.

section. For the seed pulse energies of  $40\ \mu\text{J}$  at  $100\ \text{kHz}$ ,  $110\ \mu\text{J}$  at  $10\ \text{kHz}$ , and  $100\ \mu\text{J}$  at  $1\ \text{kHz}$  the pulse durations are in the range of  $6.2\ \text{ps}$ ,  $8.1\ \text{ps}$ , and  $8.2\ \text{ps}$ , respectively. The amplifier stage consisted of two  $20\ \text{mm}$  long Ho-doped YLF crystals, which are placed  $4\ \text{mm}$  apart, with same dimension and properties as the ones used in the multipass amplifier. The first crystal exhibited a doping concentration of  $1.0\ \text{at.}\ \%$  and the second one  $1.5\ \text{at.}\ \%$ , respectively. They were wrapped in indium foil and mounted on a water-cooled copper mount. The water temperature was set to  $20\ ^\circ\text{C}$ . Increasing the doping concentration in propagation direction of the signal and pump allowed to distribute the heat load and compensated for the exponential decay of the pump light distribution. Pump and signal beam were combined via dichroic mirror. Two spherical mirrors ( $R = 250\ \mu\text{m}$ ) focused both beams in the crystals. Based on the collimated beam size, the focal beam waist radius can be calculated to a value of  $225\ \mu\text{m}$  located in between the two crystals. This is more than twice the size compared to the beam diameter in the multipass amplifier as described in Section 4.4. This beam waist was chosen according to the numerical investigations as described in the following section. Another dichroic mirror separates the amplified signal from the unabsorbed amount of pump power. The pump source was a customized Tm-doped fiber laser (LISA laser products OHG) with up to  $20\ \text{W}$  linearly polarized output at a central wavelength of  $1940\ \text{nm}$ . Pump and signal polarizations were aligned along the c-axis of the uniaxial Ho:YLF gain crystals in order to optimize the efficiency.

**Table 4.3:** Input parameters used in the numerical analysis of a single-pass booster stage operating at a pulse repetition frequency of  $1\ \text{kHz}$ .

<b>Seed parameter</b>	<b>unit</b>	<b>value</b>
Pulse energy	$\mu\text{J}$	100
Polarization		linear E  c
Center wavelength	nm	2050
Spectral bandwidth	nm	1.8
Pulse rep. freq.	kHz	1
Pulse duration	ps	8
Beam waist diameter	$\mu\text{m}$	450
<b>Pump parameter</b>	<b>unit</b>	<b>value</b>
Power	W	18
Polarization		linear E  c
Center wavelength	nm	1940
Spectral bandwidth	nm	1
Beam waist diameter	$\mu\text{m}$	450
<b>Crystal parameter</b>	<b>unit</b>	<b>value</b>
Refr. index		1.45
Dopant concentration	at.%	1.0 and 1.5
Fluorescence lifetime	ms	10 and 6
Length	mm	20

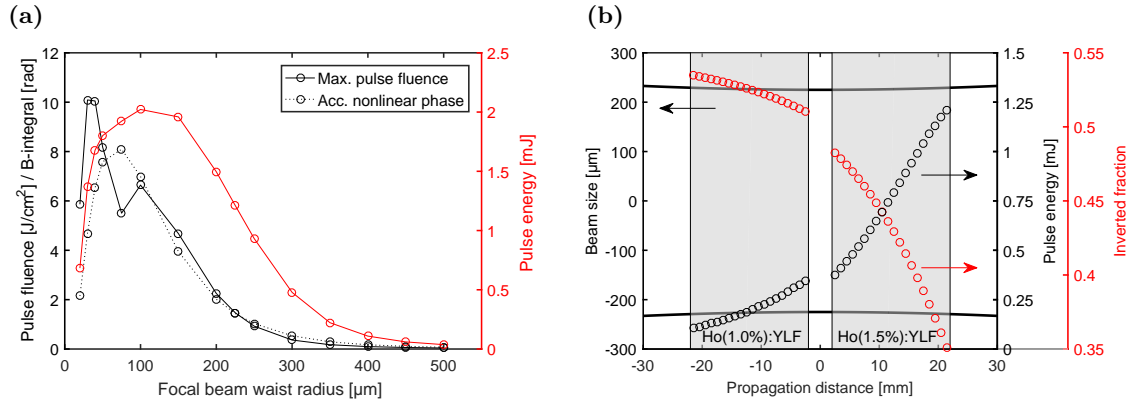


The numerical simulation of the single-pass booster amplifier was based on a calculation code written in MATLAB. It was used to support the development of the booster amplifier and to verify the experimental results. As the highest pulse energy is expected at lowest pulse repetition rate, the simulation was performed only at 1 kHz. The multipass amplifier as described above provided the input parameters such as optical spectrum, pulse energy, and pulse duration. The optical and mechanical properties of the Ho:YLF crystals were considered as well. A summary of the input parameters is given in Table 4.3.

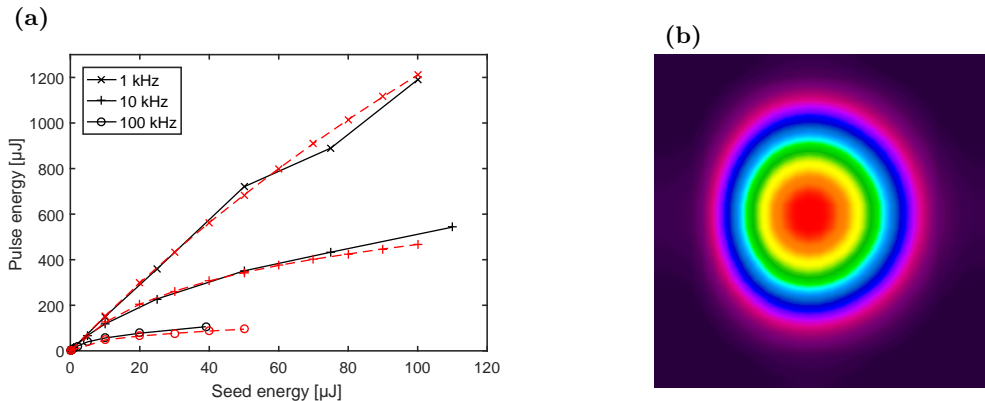
The simulation covered the evolution of the pulse energy, the peak intensity, the pulse fluence, the accumulated nonlinear phase, the optical spectrum and the inverted fraction  $A$  at steady-state as introduced in Section 4.2. However, nonlinear effects, thermal lensing, and pulse broadening due to chromatic dispersion were not considered. Figure 4.17 summarizes the simulation results. Figure 4.17(a) shows the output pulse energy, maximum pulse fluence, and accumulated B-integral as a function of the focal beam waist radius  $w_0$ . The maximum achievable pulse energy is 2 mJ at a beam waist of 100  $\mu\text{m}$ . It is decreasing for an even tighter focus due to the increasing divergence of the beam, which leads to less saturation of the gain medium, thus, less energy extraction. In contrast, it is decreasing due to the generally increasing beam size at larger beam waists. The accumulated nonlinear phase is only significant ( $> \pi$ ) in the range of  $30 \mu\text{m} < w_0 < 150 \mu\text{m}$ . As a consequence, a beam waist radius of  $> 150 \mu\text{m}$  was required. Finally, for an optimized design the pulse fluence needs to be below the damage threshold. According to the square-root scaling law and LIDT values from previous experiments, the damage threshold could be estimated to be around  $2 \text{ J/cm}^2$  at a pulse duration of 8 ps. Hence, the pulse fluence was limited to below  $2 \text{ J/cm}^2$ , which is given for a beam waist exceeding 200  $\mu\text{m}$ . It can be seen that in order to achieve more than 1 mJ of pulse energy the beam waist needs to be at least 250  $\mu\text{m}$  or less. Thus, a focal beam radius of 225  $\mu\text{m}$  was chosen to satisfy the requirements in terms of the B-integral and the pulse fluence with sufficient prospect of generating mJ-level ultrashort pulses.

Figure 4.17(b) features the details of the dual-crystal simulation at a beam waist radius of 225  $\mu\text{m}$  at steady-state. The pump and signal propagation was simulated from left to right with the solid black lines indicating the beam caustic. The shaded areas represent the two Ho:YLF crystals with doping concentrations of 1.0 at.% and 1.5 at.%, respectively. The circles show the evolution of the pulse energy (black) and the inverted fraction (red). The inversion level at the beginning of the first crystal is close to the highest possible value of 55% when a pump wavelength near 1940 nm is applied (see Figure 4.2(b)). It is decreasing in propagation direction due to the absorption-induced pump power depletion and the stronger gain saturation by the continuously amplified driving signal. These simulation results confirm that 1-mJ pulses are feasible in the proposed booster amplifier design while staying below the critical pulse fluences, which possibly induce damage or strong nonlinearities.

The corresponding experimental results will be presented in the following. The output pulse energies for different pulse repetition frequencies are presented in Figure 4.18(a).



**Figure 4.17:** Detailed simulation results of the double crystal booster amplifier according to the input parameters from Table 4.3: (a) Simulated output pulse energy, maximum pulse fluence, and accumulated nonlinear phase (B-integral) in dependence on the focal beam waist radius of the pump and signal beam; (b) evolution of the pulse energy and the inverted fraction at steady-state within the two Ho:YLF crystals (gray areas) during beam propagation in the case of a signal and pump beam waist radius of 225 μm (black solid lines).



**Figure 4.18:** (a) Numerical (red dashed line) and experimental (black solid line) results of the pulse energy with increasing seed pulse energy for different pulse repetition rates between 1 and 100 kHz. (b) Far-field beam profile of the booster amplifier output at an energy level of 1.2 mJ (1 kHz).

Since the pump source could not be tuned in terms of the output power without significantly changing its polarization properties, the pump power was kept constant at maximum value of 20 W. The input seed energy was varied and the amplified power was measured. The highest pulse energy of 1.2 mJ was obtained for the lowest pulse repetition frequency of 1 kHz. Considering the seed pulse energy of 100 μJ this corresponds to an amplification factor of 12. The highest average power of 10.6 W was achieved for a higher pulse repetition rate of 100 kHz. The extraction efficiency based on the absorbed pump power in this case is 39%, which is a remarkable value considering the operation at room temperature and the quenched lifetime associated with the high doping concentrations. The results from

the numerical model coincide with the experimental results for all different pulse repetition frequencies. They show some saturation effects of the achievable pulse energy with increasing seed pulse energy, particularly at highest pulse repetition frequency of 100 kHz. This can be explained by the fixed pump power, which was not able to provide sufficient energy stored in the gain medium to maintain a constant gain with increasing average seed power (gain saturation). The numerical simulations in Figure 4.18(a) agree well with the experimental results. The far-field beam shape was measured with a scanning-slit beam profiler. The result for 1.2 mJ pulses at the pulse repetition rate of 1 kHz is depicted in Figure 4.18(b) showing an almost perfectly round Gaussian intensity distribution.

The measured autocorrelation traces are presented in Figure 4.19(a)-(c) at maximum pulse energies for the pulse repetition frequencies of 1 kHz, 10 kHz, and 100 kHz, respectively. Based on a Gaussian pulse shape the measured durations are 8.3 ps (1 kHz), 8.2 ps (10 kHz), and 6.4 ps (100 kHz). Up to the highest achieved pulse energy of 1.2 mJ the pulse duration is considered to be sub-10 ps with a corresponding peak power of about 136 MW. The latter well exceeds the critical power in Ho:YLF crystals. The focusing length based on Equation (4.11) in this specific case is 36.7 mm. However, spatial beam distortions have not been observed as this high peak power levels are only reached at the end of the crystal. It is worth mentioning that the concave thermal lens was counteracting the nonlinear lens reducing the threshold for catastrophic self-focusing. The optical spectra are depicted in the insets (gray area). The simulated optical spectra agree with the measured ones in all cases. The side lobe centered at 2048.5 nm is a feature of the seed spectrum. The corresponding Fourier-limited pulse duration (black solid lines) indicates slightly chirped pulses. Note that these results are not directly comparable, as the seed pulse properties vary a lot depending on the pulse repetition frequency (pulse energy, spectral bandwidth, pulse duration). Therefore, a comparison of the properties such as pulse energy, spectral bandwidth, and pulse duration between the seed and the amplified pulses is given in Table 4.4. On the one hand, gain narrowing was vanishingly low. On the other hand, the amplified pulse durations were only slightly longer than those of the seed pulses. Nonlinear effects, which could appear in the optical spectrum or the autocorrelation trace are not observable. This can be attributed to the low B-integral value of 1.44 rad.

**Table 4.4:** Summary of the measured pulse energy  $E_p$ , spectral bandwidth  $\Delta\lambda$ , and pulse duration  $\tau_p$  for the amplification in the dual-crystal Ho:YLF amplifier at different pulse repetition rates  $f_{\text{rep}}$ .

$f_{\text{rep}}$	Seed			Amplified		
	$E_p$	$\Delta\lambda$	$\tau_p$	$E_p$	$\Delta\lambda$	$\tau_p$
[kHz]	[ $\mu\text{J}$ ]	[nm]	[ps]	[mJ]	[nm]	[ps]
1	100	1.3	8.0	1.2	1.26	8.3
10	110	1.33	8.1	0.54	1.3	8.2
100	40	1.51	6.2	0.11	1.4	6.4

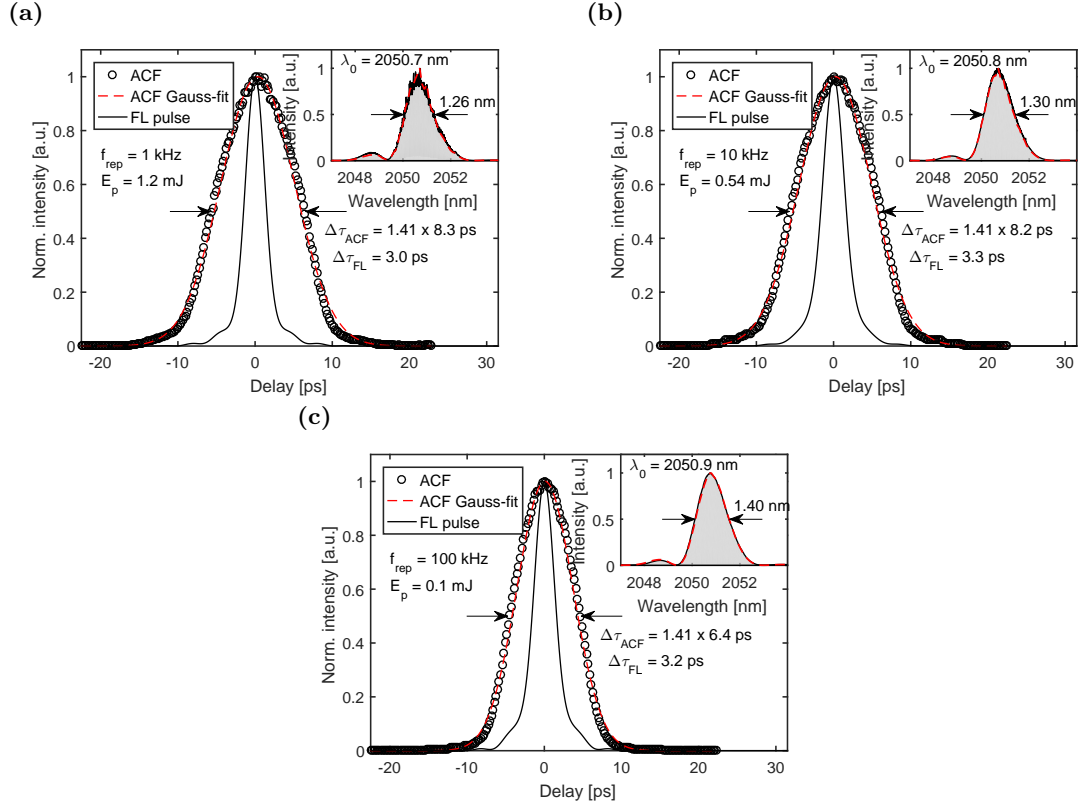


**Figure 4.19:** Measured autocorrelation traces (black circles) for different pulse repetition rates of (a) 1 kHz, (b) 10 kHz, and (c) 100 kHz at maximum achieved pulse energy assuming a Gauss-shaped pulse (red-dotted line) as well as the calculated Fourier-limited pulse duration (black solid line) based on the corresponding optical spectrum (inset, gray area), respectively. In addition, the simulated spectrum (inset, red dotted line) based on the seed optical input properties is presented.

#### 4.6 Summary and outlook

In summary, an amplifier chain was presented, which solely relied on CPA-free amplification in highly doped Ho:YLF crystals. Pulse energies up to the mJ-level with pulse durations  $< 10 \text{ ps}$  were achieved. The multipass laser amplifier benefits from its simplicity compared to the commonly applied CPA scheme in regenerative amplifiers. Due to the AOM pulse picker, any desired pulse repetition frequency can be used up to the fundamental rate of the ultrashort seed source. The operation characteristics were well-suited to support direct industrial applications as well as to pump nonlinear optical parametric conversion stages for the generation of mid-IR radiation.

Due to the limited pump power, operation at maximum pulse energy was achieved at lower pulse repetition frequency of 1 kHz. However, scaling the output power by increasing the pulse repetition frequency ( $E_p = \text{const.}$ ) seems to be feasible, particularly, since high-power pump sources ( $> 100 \text{ W}$ ) with emission at 1940 nm are commercially available.

Further investigations on the laser-induced damage threshold in Ho:YLF are necessary for generating even higher pulse energy. As scaling the latter goes hand in hand with an increasing peak power, the influence of self-focusing needs to be studied in detail. This could indicate the ultimate limit in pushing the output parameters in a CPA-free approach. However, this can be overcome by applying shorter crystals, which are cryogenically cooled to support similar gain factors at the expense of a more complex and spacious setup.

The 1890-nm pumping concept as described in Section 4.3 is another interesting possibility to optimize ultrashort pulse amplifier systems based on Ho:YLF crystals. The simulations with a pump wavelength of 1890 nm (all other input parameters the same as described in Table 4.3) show that the output pulse energy can be scaled by more than 10 % without exceeding the same maximum pulse fluence in comparison to the standard 1940-nm pumping. If the pulse fluence, i.e. the laser-induced damage threshold, is not the limiting parameter (e.g. in the case of chirped-pulse amplification), the alternative pumping scheme can be used to further increase the efficiency and the pulse energy or to decrease the size of the gain medium maintaining similar output parameters.



# CHAPTER 5

---

## Optical parametric conversion for mid-IR pulse generation

---

The mid-IR spectral region beyond  $2\ \mu\text{m}$  is interesting for a multitude of different applications and is not easily accessible as discussed in Chapter 1. The recent development of novel highly nonlinear non-oxide crystals with transparency windows reaching far into the mid-IR has established nonlinear frequency down-conversion schemes based on parametric processes, which are able to exploit the mid-wave (MWIR,  $\lambda = 3 - 8\ \mu\text{m}$ ) to long-wave infrared (LWIR,  $\lambda = 8 - 15\ \mu\text{m}$ ) and their numerous applications. Ultrashort  $2\ \mu\text{m}$  laser sources are perfectly suited to pump such schemes as demonstrated in the following chapter. In Section 5.1 the basic theory of nonlinear optics in particular second-order nonlinearities will be introduced. The focus will be on optical parametric amplification. The properties of potential crystals for the mid-IR generation will be presented in Section 5.2. The following Sections 5.3 and 5.4 will present a MWIR laser system based on a CPA-free optical parametric generation (OPG)/OPA tandem configuration pumped by the  $2\ \mu\text{m}$  front-end, which was presented in the previous Chapter 4 in Section 4.4. Finally, this chapter will be summarized in Section 5.5.

### 5.1 Theory of optical parametric generation and amplification

The following section is introducing the fundamental theoretical background of second-order nonlinear processes, particularly, parametric down-conversion of frequencies in non-centrosymmetric crystals. A more detailed insight into this topic can be found in textbooks such as [Boy08; Die06] or reviews such as [Man16; Pet15].

The propagation of an electromagnetic wave  $E(\omega)$  through a dielectric medium can be described by means of an induced macroscopic polarization  $P(\omega)$  in the material. In the case of conventional, i.e. linear light-matter interaction, the relationship between polarization and electric field can be described by the linear dependence

$$P(\omega) = \varepsilon_0 \chi^{(1)}(\omega) E(\omega) \quad (5.1)$$

with the permittivity of free space  $\varepsilon_0$  and the proportionality factor  $\chi^{(1)}(\omega)$  known as the linear or first-order susceptibility. Note that the first-order electric susceptibility  $\chi^{(1)}(\omega)$  defines the linear propagation phenomena such as chromatic dispersion and absorption in the medium. The real part of  $\chi^{(1)}$  is related to the linear refractive index  $n(\omega)$  by  $n(\omega) = \sqrt{1 + \text{Re}[\chi^{(1)}(\omega)]}$  (see Section 3.1.1), whereas the imaginary part defines the

absorption according to  $\alpha(\omega) = \omega \cdot \text{Im} [\chi^{(1)}(\omega)] / nc_0$ . In nonlinear optics, Equation (5.1) needs to be generalized by means of a polynomial expansion under the assumption of an instantaneous response, which yields

$$\begin{aligned} P(\omega) &= \varepsilon_0 \left( \chi^{(1)}(\omega)E(\omega) + \chi^{(2)}(\omega)E^2(\omega) + \chi^{(3)}(\omega)E^3(\omega) + \dots \right) \\ &= \underbrace{P^{(1)}(\omega)}_{P_L(\omega)} + \underbrace{P^{(2)}(\omega) + P^{(3)}(\omega) + \dots}_{P_{NL}(\omega)} \end{aligned} \quad (5.2)$$

The higher order quantities  $\chi^{(2)}(\omega)$  and  $\chi^{(3)}(\omega)$  are called second- and third-order nonlinear optical susceptibilities, respectively. While the first term in Equation (5.2) describes the linear propagation according to Equation (5.1), the higher order terms represent the nonlinear polarization response  $P_{NL}(\omega) = P^{(2)}(\omega) + P^{(3)}(\omega) + \dots$  of the material. Note that the susceptibility  $\chi^{(k)}(\omega)$  is a tensor of the rank  $k + 1$  for anisotropic media. Second-order nonlinear interactions can only emerge in non-centrosymmetric media, e.g. in crystals without inversion symmetry. Historically, the second-order susceptibility  $\chi^{(2)}$  is often expressed by the nonlinear coefficient  $d$  defined as  $d = \chi^{(2)}(\omega)/2$  in units of pm/V.

In the simple case of two monochromatic plane waves with distinct frequencies  $\omega_1$  and  $\omega_2$  (according to Equation (3.7) incident upon a crystal for which  $\chi^{(2)} \neq 0$  is given), the second-order nonlinear polarization  $P^{(2)}(\omega)$  consists of terms oscillating at the sum- and difference-frequencies. Second-harmonic generation (SHG) is a particular case of sum-frequency generation (SFG), in which the two interacting photons have the same properties in terms of their frequency. This process, which effectively generates photons at half the wavelength (twice the frequency) of the initial photons, was the first nonlinear optical process presented in 1961 by FRANKEN et al. [Fra61] soon after the demonstration of the first laser. In any other case, assuming  $\omega_1 > \omega_2$ , new frequencies at  $\omega_{\text{SFG}} = \omega_1 + \omega_2$  and  $\omega_{\text{DFG}} = \omega_1 - \omega_2$  are generated.

The difference-frequency generation (DFG) process is also known as optical parametric amplification (OPA) as the higher-frequency input field ( $\omega_1$ ) is annihilated while the lower-frequency component ( $\omega_2$ ) is amplified. The essential difference between these two mechanisms is the strength of the interacting fields: If the input fields  $\omega_1$  and  $\omega_2$  exhibit comparable intensities, the process is denoted DFG. In contrast, in the case of OPA the lower-frequency field  $\omega_2$  is much weaker exhibiting gain during nonlinear interaction, which can amount to several orders of magnitude. In accordance to the common nomenclature, the indices for parametric processes are changed to  $1 \rightarrow p$ ,  $2 \rightarrow s$ , and  $\text{DFG} \rightarrow i$  for pump (p), signal (s), and idler (i) wave, respectively, implying that  $\omega_i \geq \omega_s > \omega_p$ . The OPA process is schematically depicted in Figure 5.1.



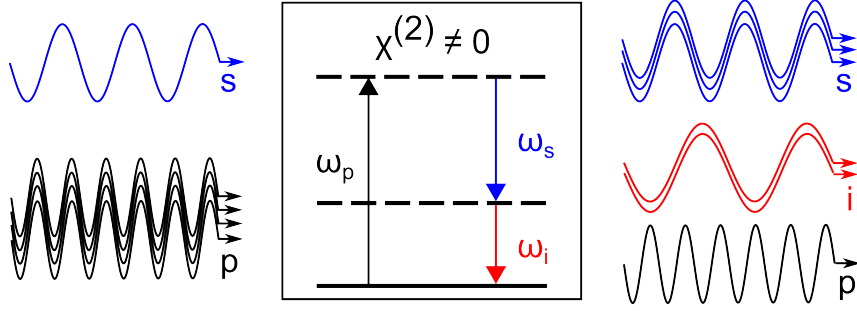


**Figure 5.1:** Schematic photon energy diagram for the second-order nonlinear three-wave mixing process optical parametric amplification. A seeded signal wave (s) gets amplified at the expense of an annihilated pump photon (p). At the same time an idler photon (i) with new frequency at  $\omega_i = \omega_p - \omega_s$  is generated.

The three-wave nonlinear interaction process in an optical parametric amplifier has to fulfill the photon energy and momentum conservation:

$$\begin{aligned}\hbar\omega_p &= \hbar\omega_s + \hbar\omega_i, \\ \hbar\vec{k}_p &= \hbar\vec{k}_s + \hbar\vec{k}_i,\end{aligned}\tag{5.3}$$

A special case in which only one frequency  $\omega_p$  enters the nonlinear medium is called optical parametric generation (OPG). According to Equation (5.3) two waves with lower frequencies  $\omega_s$  and  $\omega_i$  are generated. This process is based on optical parametric fluorescence starting from quantum noise which is then amplified to a significant level. A more detailed description of this pure quantum-mechanical effect can be found in literature [Car00; Kle68]. The OPG effect can be efficiently enhanced by enclosing the system in an optical resonator, which in its simplest case provides feedback for either the generated signal or idler wave. This concept is called optical parametric oscillator (OPO) and was first proposed in 1962 by KROLL [Kro62] and realized in 1965 by GIORDMAINE et al. [Gio65].

#### Coupled wave equations for optical parametric amplification

A common way to describe the three-wave mixing process for propagation collinearly along the  $z$ -axis in a lossless medium is a system of nonlinear coupled differential wave equations:

$$\begin{aligned}\frac{dA_p}{dz} &= -i\frac{\omega_p d_{\text{eff}}}{n(\omega_p)c_0}A_i A_s e^{i\Delta kz}, \\ \frac{dA_s}{dz} &= -i\frac{\omega_s d_{\text{eff}}}{n(\omega_s)c_0}A_i^* A_p e^{-i\Delta kz}, \\ \frac{dA_i}{dz} &= -i\frac{\omega_i d_{\text{eff}}}{n(\omega_i)c_0}A_s^* A_p e^{-i\Delta kz}.\end{aligned}\tag{5.4}$$

Note that these equations are only valid in the case of linearly polarized, plane waves assuming the slowly varying envelope approximation (see Section 3.1)  $|\frac{d^2 A_n}{dz^2}| \ll k_n |\frac{dA_n}{dz}|$ . This set of coupled wave equations can describe the various types of three-wave mixing processes,

such as OPA, which yields the corresponding intensity evolution  $I(z) = 2\varepsilon_0 c_0 n_0(\omega) |A(z)|^2$  of each wave. Equation (5.4) introduces the effective nonlinear optical coefficient  $d_{\text{eff}}$ , which is dependent on the propagation directions and polarizations of the contributing waves, and the wave-vector or phase mismatch  $\Delta k = k_p - k_s - k_i$  of the OPA process (see Section 5.1). The coupled wave equations can only be solved numerically. However, under the assumption of no pump depletion  $dA_p/dz = 0$  and neglectable initial idler  $A_i(0) = 0$ , an analytical solution for the evolution of the signal and idler intensities yields [Har69]

$$\begin{aligned} I_s(z) &= I_s(0) \left[ 1 + \frac{\Gamma^2}{g^2} \sinh^2(gz) \right], \\ I_i(z) &= I_s(0) \frac{\omega_i}{\omega_s} \frac{\Gamma^2}{g^2} \sinh^2(gz). \end{aligned} \quad (5.5)$$

Here, the exponential gain parameter  $\Gamma$  and the effective gain coefficient  $g$  are defined as

$$\begin{aligned} \Gamma &= \sqrt{\frac{2\omega_s \omega_i d_{\text{eff}}^2}{n_p n_s n_i \varepsilon_0 c_0^3} \cdot I_p}, \\ g &= \sqrt{\Gamma^2 - \left(\frac{\Delta k}{2}\right)^2}. \end{aligned} \quad (5.6)$$

As already mentioned, the gain coefficient  $g$  is strongly dependent on the wave-vector mismatch  $\Delta k$  and the pump intensity  $I_p$  dependent parameter  $\Gamma$ , which also represents the nonlinear potential of the  $\chi^{(2)}$  medium. Commonly, the nonlinear figure of merit (FOM) associated with an optical nonlinear medium is given by  $d_{\text{eff}}^2/n^3$  with respect to Equation (5.6) classifying the conversion potential. The steady-state parametric gain of the seeded signal wave can be expressed as

$$G = \frac{I_s(z)}{I_s(0)} = 1 + \frac{\Gamma^2}{g^2} \sinh^2(gz). \quad (5.7)$$

In the case of high gain ( $gz \gg 1$ ) and perfect phase-matching ( $\Delta k = 0$ ) Equation (5.7) yields

$$G \cong \frac{1}{4} \exp(2\Gamma z). \quad (5.8)$$

Equation (5.8) implies an exponential growth of the amplified signal wave in an OPA, which scales with the nonlinear coefficient  $d_{\text{eff}}$ , the crystal length  $z$ , and the square root of the pump wave intensity  $\sqrt{I_p}$ . Thus, high-energy ultrafast pump sources are beneficial as the intensity scales with the pulse energy  $E_p$  and duration  $\tau$  according to  $I \propto \frac{E_p}{\tau}$ .

### Phase-matching

As seen in the coupled wave equations (5.4), phase-matching is very important to maximize the efficiency of the nonlinear conversion process. The wave-vector mismatch  $\Delta k$  in an OPA process is defined as  $\Delta k = k_p - k_s - k_i$ .  $\Delta k = 0$  is equivalent to

$$n(\omega_i)\omega_i = n(\omega_p)\omega_p - n(\omega_s)\omega_s. \quad (5.9)$$

Figure 5.2(a) shows the relation between the accumulated phase mismatch  $\Delta kz$  and the normalized parametric gain of a nonlinear crystal with propagation length  $z$ . Optimum phase-matching  $\Delta kz = 0$ , known as phase-matching condition [Gio62; Mak62], results in a maximum gain. In contrast, the parametric gain drops to zero at  $\Delta kz = 2\pi$ . In isotropic, homogeneous media perfect phase-matching conditions are impossible to satisfy due to the dispersion. In this case the parametric gain experiences oscillations along the propagation direction as illustrated in Figure 5.2(b). However, phase-matching can be achieved by means of the following most widely used techniques:

- *Birefringent phase-matching* is commonly considered angular phase-matching. It exploits birefringent materials, where the refractive index depends on the polarization and the propagation direction of the electromagnetic wave. Here, the description is limited to uniaxial birefringent crystals, whereas a general treatment including biaxial birefringent crystals is explained in [Dmi99; Zer73]. Uniaxial crystals can be characterized by a particular direction, which is denoted the optic axis. As shown in Figure 5.3(a), the optic axis and the propagation vector  $\vec{k}$  define a plane. Light polarized perpendicular to that plane experiences the ordinary refractive index  $n_o$ , whereas light polarized parallel to that plane experiences the extraordinary refractive

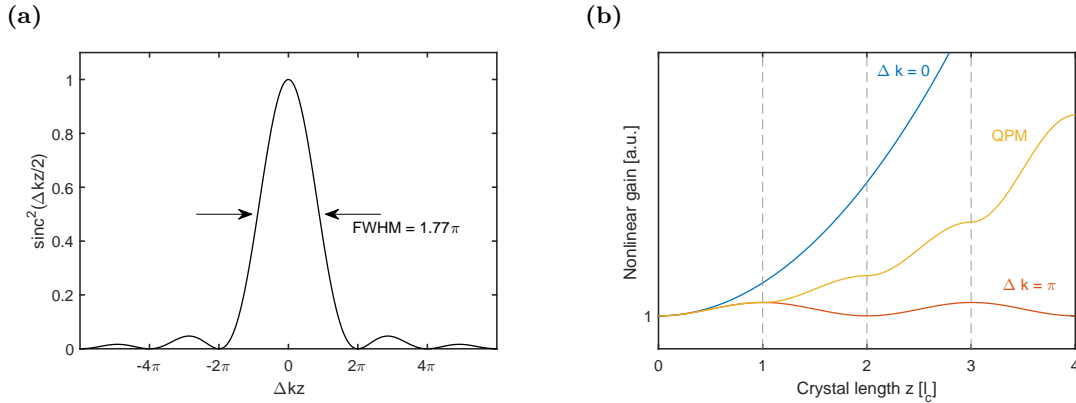


**Figure 5.2:** (a) Normalized parametric gain of a nonlinear optical crystal with propagation length  $z$  as a function of the accumulated phase mismatch  $\Delta kz$ . (b) Schematic evolution of the nonlinear parametric gain  $G$  seen by the seeded signal in an OPA as a function of the propagation length  $z$  for perfect phase-matching condition (blue), non-phase-matched case (red), and quasi-phase-matching (yellow).

index  $n_e(\theta)$ , which depends on the angle  $\theta$  between the optic axis and  $\vec{k}$ :

$$\frac{1}{n_e(\theta)^2} = \frac{\sin(\theta)^2}{n_e^2} + \frac{\cos(\theta)^2}{n_o^2}, \quad (5.10)$$

with the principal value  $n_e = n_e(\theta = 90^\circ)$ . One distinguishes between positive ( $n_e > n_o$ ) and negative uniaxial crystals ( $n_e < n_o$ ). For an appropriate angle  $\theta_m$  as schematically depicted in Figure 5.3(b) and polarization of the interacting waves in the birefringent crystal, the phase-matching condition can be realized giving exponential rise to the parametric gain (see Figure 5.2(b)). Taking into account the sequence  $\omega_i \leq \omega_s < \omega_p$  of the interacting fields for optical parametric generation (p  $\rightarrow$  si), the notation for type-I phase-matching conditions are e  $\rightarrow$  oo or o  $\rightarrow$  ee in an optically negative or positive uniaxial crystal, correspondingly. The type-II interaction in an optically negative (positive) crystal is denoted either e  $\rightarrow$  eo (o  $\rightarrow$  eo) or e  $\rightarrow$  oe (o  $\rightarrow$  oe).

Angular phase-matching is also known as critical phase-matching, as the birefringence has a serious drawback when  $\theta$  differs from  $0^\circ$  or  $90^\circ$ . In this case the Poynting vector  $\vec{S}$  and the propagation direction defined by  $\vec{k}$  of the extraordinary ray are not parallel. The corresponding angle is denoted walk-off angle  $\rho$ , which is dependent on

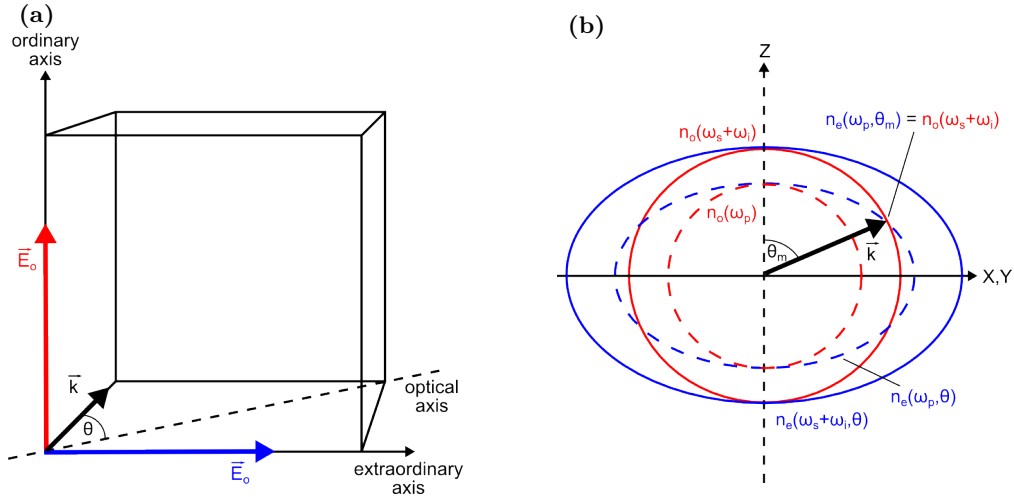


**Figure 5.3:** (a) Definition of ordinary and extraordinary directions in birefringent crystals. (b) Type-I, angular phase-matching in a negative, uniaxial crystal with signal and idler being the ordinary beams, whereas the pump is the extraordinary beam. Phase-matching condition is fulfilled for beam propagation at an angle of  $\theta_m$  with respect to the principal axis Z. In this case the index ellipsoid of the extraordinary pump  $n_e(\omega_p, \theta_m)$  intersects the sphere of ordinary signal and idler  $n_o(\omega_s + \omega_i)$ .

the phase-matching angle  $\theta$  according to [Boy65]

$$\tan(\rho) = \frac{n_{e,s}^2}{2} \left[ \frac{1}{n_{o,p}^2} - \frac{1}{n_{e,p}^2} \right] \sin(2\theta) \quad (5.11)$$

for the signal radiation in the case of a positive uniaxial crystal. During their collinear propagation through the crystal, ordinary and extraordinary beams diverge from each other reducing continuously the spatial overlap. Consequently, the interaction length in the nonlinear material is limited. For Gaussian beams this propagation distance, which is called aperture length  $l_a$ , is related to  $\rho$  by [Boy65]

$$l_a = \sqrt{\pi} w_0 / \rho \quad (5.12)$$

with  $w_0$  the pump beam waist radius. However, spatial walk-off vanishes for a propagation perpendicular to the principle axis ( $\theta = 90^\circ$ ). The phase-matching condition in this case can be achieved by exploiting nonlinear crystals whose birefringence is considerably temperature-dependent. Temperature-controlled phase-matching, also denoted non-critical phase-matching, is particularly interesting for tight focusing or long interaction lengths.

- *Quasi-phase-matching* (QPM) exploits a medium with alternating sign of the nonlinear optical coefficient  $\chi^{(2)}$ . Most commonly, the modulation period is chosen according to the coherence length  $l_c = \pi/\Delta k$  (see Figure 5.2(b)), where the conversion efficiency drops to 0.4 (see Figure 5.2). Here, phase-matching is not locally satisfied, but the periodical modulation leads to an average macroscopic exchange of energy between the fields [Hum07]. In comparison to angular phase-matching, QPM offers an advantage: It allows to use isotropic media such as gallium arsenide [Ska02]. Additionally, the polarization of the three coupled waves can be equal, which allows to exploit the largest nonlinear coefficient  $d$  of the crystal. However, it can be shown that the effective nonlinear coefficient  $d_{\text{eff}}$  is reduced by a factor of  $\pi/2$  in comparison to perfect phase-matching [Die06]. Common examples of nonlinear crystals for quasi-phase-matching are periodically poled lithium niobate (PPLN), potassium arsenate (PPKTA), potassium triphosphate (PPKTP) as well as OP-GaAs or orientation-patterned gallium phosphide (OP-GaP).

All these considerations, which are based on a monochromatic description, are taken into account for the layout of a frequency conversion stage. In contrast, the interaction of three spectrally broadband, coupled waves is more challenging and has not performed in this thesis. The interested reader is referred to [Die06] or [Man16], which provide a mathematical description including additional real experimental conditions like beam divergence or inhomogeneously distributed temperature. Next to the operation conditions, choosing

an appropriate nonlinear optical material plays a major role in developing parametric converters.

## 5.2 Properties of nonlinear crystals for mid-IR coherent sources

In recent years, the demand for high quality nonlinear optical materials for mid-infrared frequency conversion has increased. The major reason is the emergence of ultrafast laser applications as introduced in Section 1. However, traditional oxide crystals such as lithium niobate ( $\text{LiNbO}_3$ ) or potassium titanyl phosphate ( $\text{KTiOPO}_4$ ) suffer from the onset of severe multi-phonon absorption in the spectral region beyond  $4\ \mu\text{m}$ . With the development of coherent  $2\ \mu\text{m}$  sources, non-oxide nonlinear optical semiconductors such as zinc germanium phosphide ( $\text{ZnGeP}_2$ , or ZGP) or orientation-patterned gallium arsenide (OP-GaAs) have been established. Their transparency range offers the access to much longer mid-infrared radiation. However, they need to be pumped at wavelength  $\geq 1.9\ \mu\text{m}$  due to two-photon absorption at the lower bandgap edge. The chalcopyrites silver gallium sulfide ( $\text{AgGaS}_2$ , or AGS) and silver gallium selenide ( $\text{AgGaSe}_2$ , or AGSe) can be pumped at  $1\ \mu\text{m}$  and  $1.5\ \mu\text{m}$ , respectively, but exhibit very low laser-induced damage threshold and extremely poor thermo-mechanical properties. More recently, novel materials such as cadmium silicon phosphide ( $\text{CdSiP}_2$ , or CSP) and orientation-patterned gallium phosphide (OP-GaP) have successfully been demonstrated, which can be pumped with the well-developed  $1$  and  $1.5\ \mu\text{m}$  laser sources. The commercial availability of the former materials, however, is currently limited. In the appendix, Table B.1 provides a broad overview considering the most important nonlinear crystals, which offer access far into the mid-IR spectral region, with their mechanical and optical properties.

In Figure 5.4(a) the most prominent nonlinear optical materials for mid-infrared frequency conversion are summarized in terms of their efficiency potential represented by the nonlinear figure of merit ( $d_{\text{eff}}^2/n^3$ ) versus their transparency range. Among these crystals,

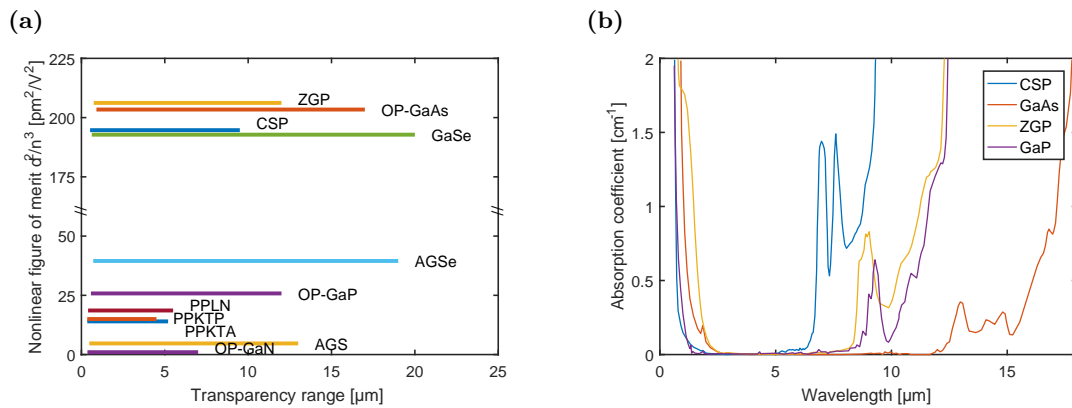


**Figure 5.4:** (a) Nonlinear FOM ( $d_{\text{eff}}^2/n^3$ ) versus transparency range of common nonlinear optical crystals for the mid-infrared spectral range. (b) Absorption spectra in the mid-IR spectral range for CSP, GaAs, ZGP, and GaP (digitized from [Sch16]).

ZGP has been widely used as nonlinear optical material for mid-infrared conversion since its first presentation in the early 1970s [Boy72]. Its nonlinear FOM is about an order of magnitude higher than that of oxide-based crystals. Nowadays, the improvement in crystal growth has pushed the optical quality reducing absorption losses in ZGP to below  $0.05 \text{ cm}^{-1}$  at  $2.05 \text{ }\mu\text{m}$  [Sch16]. The reported LIDT is on the order of  $4 \text{ J/cm}^2$ , making ZGP crystals attractive for high-energy applications. Figure 5.4(b) shows the typical absorption spectra for the non-oxide crystals with high potential in the mid-infrared, namely ZGP, CSP, GaAs, and GaP [Sch16]. Although gallium selenide (GaSe) provides superior transparency range and comparably nonlinear FOM, the main disadvantage is the layered structure of the material, which makes cutting and polishing at arbitrary angles difficult [All09].

Type-I interaction in ZGP crystals is advantageous due to the broader tuning range that is achievable with angular phase-matching and a lower pump threshold. In contrast, type-II nonlinear interaction in ZGP crystals is preferable for pulse durations  $> 1 \text{ ps}$ , since it provides much narrower and nearly wavelength-independent bandwidths [Pet99; Vod99]. Here, ZGP has been used for nonlinear frequency down-conversion of the  $2 \text{ }\mu\text{m}$  radiation into the mid-IR spectral region. The samples exhibit an aperture of  $5 \times 3 \text{ mm}^2$  with a length of  $4.9 \text{ mm}$ . They were cut at an angle of  $\theta = 55^\circ$  for type-I phase-matching. Based on the nonlinear coefficient  $d_{36} = 75.4 \text{ pm/V}$  (from [Boy71] corrected by Miller's rule [Mil64]), the effective nonlinear coefficient yields  $d_{\text{eff}} = 78.9 \text{ pm/V}$  in the case of optical parametric generation of  $3 \text{ }\mu\text{m}$  signal radiation from  $2.05 \text{ }\mu\text{m}$  pump wavelength in the type-I collinearly phase-matched ( $o \rightarrow ee$ ) condition.

The transmission of the ZGP crystals has been calculated based on the properties of the anti-reflection coating in combination with intrinsic absorption of the material as provided by the manufacturer (BAE Systems). The results are depicted in Figure 5.5(a). Due to the finite bandwidth of the anti-reflection coating, the transparency range is limited to below  $\sim 8.5 \text{ }\mu\text{m}$ . The measured absorption coefficient at the pump wavelength of  $2.05 \text{ }\mu\text{m}$

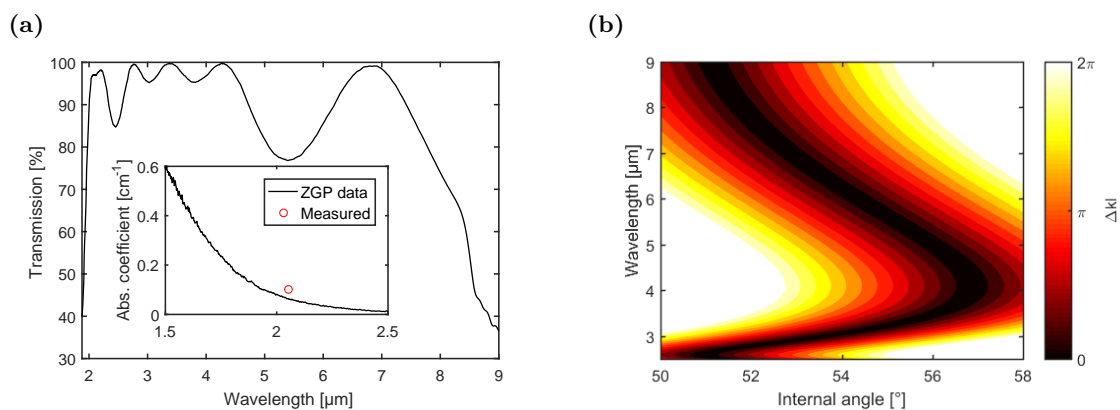


**Figure 5.5:** (a) Transmission of the ZGP crystal considering the anti-reflection coating as specified by the manufacturer and the intrinsic material absorption (inset, from [Pet99]). (b) Type-I phase-matching ( $o \rightarrow ee$ ) in ZGP pumped at a wavelength of  $2.05 \text{ }\mu\text{m}$ .

is  $0.1 \text{ cm}^{-1}$ . A comparison to the intrinsic material absorption between  $1.5 \text{ }\mu\text{m}$  to  $2.5 \text{ }\mu\text{m}$  is given in the inset of Figure 5.5(a), which yields  $0.07 \text{ cm}^{-1}$  at the intended pump wavelength of  $2.05 \text{ }\mu\text{m}$ .

Figure 5.5(b) presents the calculated phase mismatch  $\Delta kl$  for the ZGP crystal ( $l = 4.9 \text{ mm}$ ) in dependence on the internal phase-matching angle for various combinations of signal and idler wavelengths in the spectral region between  $2.5 \text{ }\mu\text{m}$  and  $9 \text{ }\mu\text{m}$  for a pump wavelength of  $2.05 \text{ }\mu\text{m}$ . Type-I angular phase-matching has been applied according to Equations (5.9) and (5.10) taking into account the frequency dependent ordinary and extraordinary refractive indices of ZGP. Degeneracy is achieved at twice the pump wavelength, whereas a phase mismatch of  $\Delta kl = 2\pi$  corresponds to parametric gain of zero (see Figure 5.2). Note that any temperature dependence on the refractive index has been neglected.

### 5.3 Mid-IR generation via OPG

The nonlinear generation of narrowband mid-infrared radiation by means of  $2 \text{ }\mu\text{m}$  pump sources has been shown either via DFG [Chu14; Sán14], OPG [Pet99; Rot01; Wan16], or OPO [Hen06; Lee13; Lei12] processes. Alternatively, (super-)octave spectral access is provided by supercontinuum generation in nonlinear fibers [Kub14], waveguides [Kuy11; Phi11], crystals [Che18], and bulk glasses [Gar17; Lia15], or via intrapulse DFG [But19; Gai18]. While the broadband emission in supercontinuum generation and intrapulse DFG with an average power typically in the sub-W regime is beneficial for spectroscopy in e.g. analytical chemistry, environmental monitoring, or life sciences, narrowband emission in OPG and DFG benefits from its high spectral density used for materials processing, medical applications, or sensing of specific trace gases. Among these nonlinear mid-IR generation approaches, OPG represents the simplest route towards intense mid-IR radiation. In comparison to DFG it requires only one input driving wavelength, while sufficient spectral broadening in supercontinuum generation can only be achieved by propagating femtosecond ( $\tau < 400 \text{ fs}$ ) optical pulses through a short piece of bulk glass or crystals.

Alternatively, much longer pulses in the ps-regime can be used in a nonlinear fiber or in waveguides at the expense of a limited average power. Just recently, supercontinuum generation with  $2 \text{ ps}$  pulses at  $2.05 \text{ }\mu\text{m}$  in a long YAG rod has been demonstrated [Che18]. However, pulse energies in the range of  $100 \text{ }\mu\text{J}$  are necessary to generate significant power levels in the spectral range above  $3 \text{ }\mu\text{m}$ .

Here, the mid-IR generation is realized in a traveling-wave OPG based on the highly nonlinear ZGP crystal. This comparably simple scheme benefits from its rather high conversion efficiency into a narrow bandwidth, thus, high spectral densities, maintaining broad wavelength tunability in dependence on the phase-matching conditions. The developed OPG stage, depicted in Figure 5.6(a), consisted of a  $4.9 \text{ mm}$  long ZGP crystal, which exhibited the optical properties presented in Section 5.2. Furthermore, the crystal was cut at an angle of  $55^\circ$  with respect to the optical axis for type-I phase-matching. It was



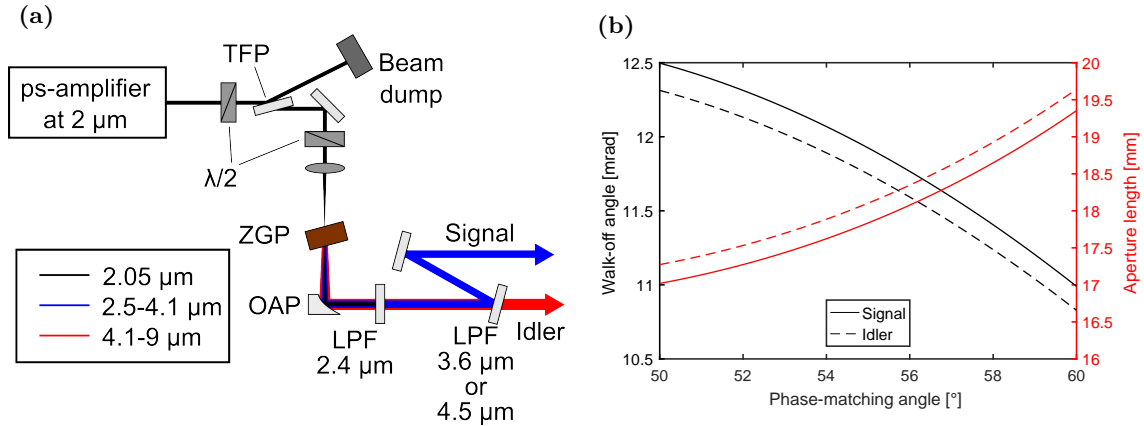


**Figure 5.6:** (a) Experimental setup of the mid-IR OPG. OAP: off-axis parabolic mirror, TFP: thin-film polarizer, LPF: long-pass filter,  $\lambda/2$ : half-wave plate. (b) Calculated walk-off angle and aperture length in ZGP as a function of the phase-matching angle for a signal and idler wavelength of 3  $\mu\text{m}$  and 6.5  $\mu\text{m}$ , respectively.

mounted on a rotation table to be able to tune the phase-matching angle. The ZGP crystal was not actively temperature stabilized, thus being operated around room temperature. The 2  $\mu\text{m}$  multipass laser amplifier described in Section 4.4 is used as front-end to pump the ZGP crystal. The maximum pump energy was 50  $\mu\text{J}$  at a pulse repetition rate of 100 kHz, which corresponds to a maximum average pump power of 5 W. A set of half-wave plate and thin-film polarizer was used to attenuate the pump power. The pump light was focused by a lens ( $f = 100 \text{ mm}$ ) into the crystal to achieve a focal beam waist diameter of 120  $\mu\text{m}$  in order to maximize the pump pulse intensity without exceeding the LIDT of the ZGP crystal, which will be discussed later. The linear pump pulse polarization was rotated by means of a half-wave plate prior to the focusing lens to meet the requirements set by the phase-matching condition. The generated signal and idler as well as the residual pump light were collimated via silver-coated off-axis parabolic mirror ( $f = 50 \text{ mm}$ ). A long-pass filter with a cut-on wavelength of about 2.4  $\mu\text{m}$  was used to remove the residual pump energy. For the characterization of the generated signal and idler different long-pass filters with cut-on wavelengths of about 3.6  $\mu\text{m}$  and 4.5  $\mu\text{m}$  were used, respectively, in order to improve the dynamic range.

The rather tight focusing scheme demands for an investigation of the aperture length, which limits the propagation length due to spatial walk-off (see Section 5.1). The calculated spatial walk-off angle and the corresponding aperture length as a function of the phase-matching angle are presented in Figure 5.6(b). As the aperture length is considerably longer than the length of the used ZGP crystals over the whole type-I phase-matching angular bandwidth, walk-off effects can be considered to be vanishingly low in the following experiments.

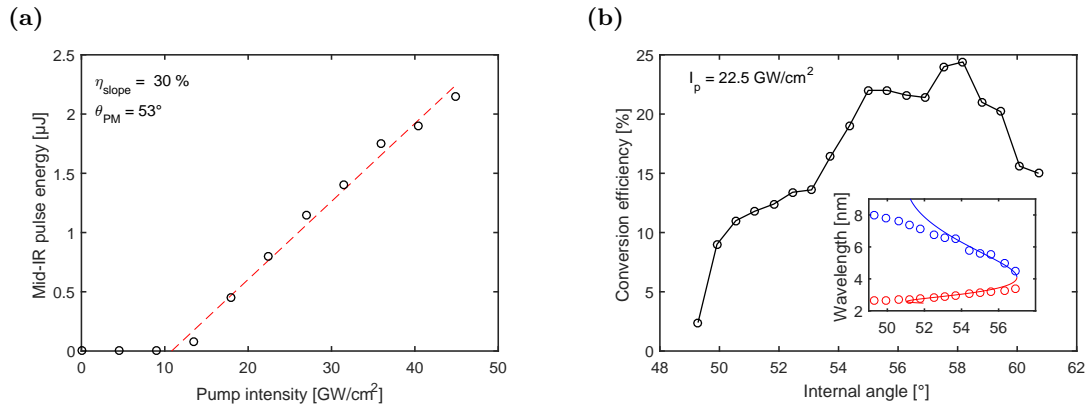


**Figure 5.7:** 2.05  $\mu\text{m}$  pumped optical parametric generation: mid-IR pulse energy (combined signal and idler) (a) in dependence on the pump intensity for a fixed phase-matching angle of  $\theta = 53^\circ$  and (b) in dependence on the internal phase-matching angle for a fixed pump intensity of 17  $\text{GW}/\text{cm}^2$ . The inset compares the experimentally obtained center wavelengths at different phase-matching angles with the theoretical values calculated from Equations (5.9) and (5.10) taking into account the frequency dependent ordinary and extraordinary refractive indices of ZGP.

Figure 5.7(a) shows the measured combined signal and idler power with increasing pump pulse intensity, while the phase-matching angle  $\theta$  is set to  $53^\circ$ . The OPG process was observed for pump intensities of  $> 10 \text{ GW}/\text{cm}^2$  with a parametric fluorescence cone emerging at further increasing pump intensities. The slope efficiency (red dashed line) amounts to 30% with respect to the incident pump pulse energy. The maximum pump pulse energy was limited to 10  $\mu\text{J}$  ( $45 \text{ GW}/\text{cm}^2$ ) due to the onset of laser-induced damage of the anti-reflection-coated surface of the ZGP crystal. This corresponds to an on-axis peak fluence of about  $0.18 \text{ J}/\text{cm}^2$ . Most systematic investigations on the LIDT in ZGP have been performed for rather long test pulses with durations in the ns-regime [Hil14; Pet95; Zaw06]. VODOPYANOV [Vod93] reported surface damage at a threshold of  $30 \text{ GW}/\text{cm}^2$  ( $3 \text{ J}/\text{cm}^2$ ) for 2.94- $\mu\text{m}$  pulses with a duration of 100 ps. Considering the square-root scaling law [Bet76] these values are similar to the ones obtained here. Additionally, this LIDT value is confirmed by previous experiments with few-ps pumped ZGP crystals at peak intensities of  $20 \text{ GW}/\text{cm}^2$ , which happened without any damage to the crystal [San16]. It is worth mentioning that in our setup the damage in the ZGP crystal occurred first at the entrance surface of the pump radiation.

The conversion efficiency in dependence on the phase-matching tuning is depicted in Figure 5.7(b). The combined signal and idler pulse energy for different internal phase-matching angles at a fixed pump intensity of  $22.5 \text{ GW}/\text{cm}^2$  is shown. Higher phase-matching angles  $> 61^\circ$  were not possible as the phase-matching condition is not fulfilled (see Figure 5.5(b)). The highest conversion efficiency was obtained near degeneracy as expected, which corresponds to an internal phase-matching angle of  $57^\circ$ . The inset of Figure 5.7(b) shows the corresponding center wavelengths in comparison to the theoretical predictions. The discrep-

ancy at the long wavelengths  $> 8 \mu\text{m}$  can be attributed to the increased losses induced by the finite bandwidth of the anti-reflection coating (see Figure 5.5(a)) and the limited detection sensitivity of the used Fourier-transform infrared spectrometer (ArcOptix, FT-MIR 1.5-8.5).

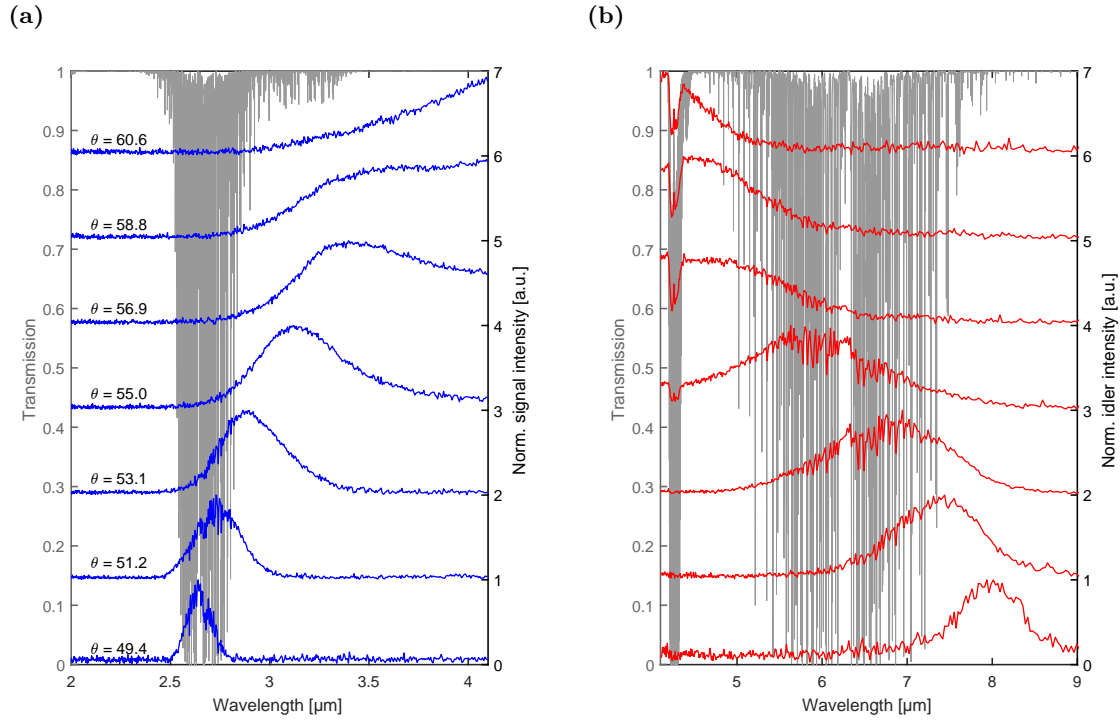


**Figure 5.8:** (a) Signal (blue) and (b) corresponding idler (red) spectra at different internal mode-matching angles in the ZGP-based OPG pumped with  $3.8 \mu\text{J}$  at a wavelength of  $2.05 \mu\text{m}$ . The transmission for the propagation through 1 m in the laboratory environment is shown in gray color (left axis). The latter has been calculated for a room temperature of  $20^\circ\text{C}$  and a relative humidity of 20 % based on the data provided by the HITRAN database [HIT19].

Figures 5.8(a) and (b) show the optical power spectra of the signal and idler radiation covering the full MWIR wavelength range between  $2.6$  and  $8 \mu\text{m}$ . The results are consistent with the theoretical ones of the phase mismatch in Figure 5.5(b). The OPG linewidth is rather large around the degeneracy point of  $4.1 \mu\text{m}$  and decreases as the signal and idler frequencies diverge. Shorter wavelengths of less than  $2.5 \mu\text{m}$  could not be detected due to the cut-on wavelength of the long-pass filter at  $2.4 \mu\text{m}$  to separate residual pump from the generated mid-IR radiation. Longer wavelengths of more than  $9 \mu\text{m}$  could not be detected due to the limited spectral sensitivity of the spectrometer and finite anti-reflection coating bandwidth as shown in Figure 5.5(a). Additionally, Figures 5.8(a) and (b) show the simulated transmission through 1 m in laboratory environment. The absorption around  $2.7 \mu\text{m}$  and  $6.5 \mu\text{m}$  can be attributed to water vapor in the air, whereas the strong absorption around  $4.2 \mu\text{m}$  originates from the atmospheric  $\text{CO}_2$  content. One can clearly identify the

water and CO<sub>2</sub> absorption lines in the spectra, which coincide with the simulated data [HIT19].

#### 5.4 High conversion efficiency mid-IR OPA

Only part of the available pump energy of 50  $\mu\text{J}$  could be used in the OPG stage to generate low-energy signal and idler pulses limited by the LIDT. The remaining pump pulse energy was used for the amplification in an optical parametric amplifier. As the seed and pump pulses in the OPA originated from the same front-end, no temporal synchronization except for a fixed delay stage was required. In addition, as the expected mid-IR seed pulse duration was similar to the pump pulse duration, no temporal stretching or compression was needed to optimize the parametric efficiency. Considering the CPA-free optical parametric amplification, the beam size needed to be tailored such that laser-induced damage was mitigated and, simultaneously, proper conversion efficiencies were obtained. GUARDALBEN et al. [Gua03] has shown that highest efficiency can be expected for an operation around pump depletion, which manifests itself through gain saturation in the OPA process. In contrast, the power stability is optimized for stronger back conversion, which does not coincide with the point of maximum conversion efficiency [Gua03]. Hence, every OPA design consideration involves an inherent trade-off between maximized efficiency and pulse stability.

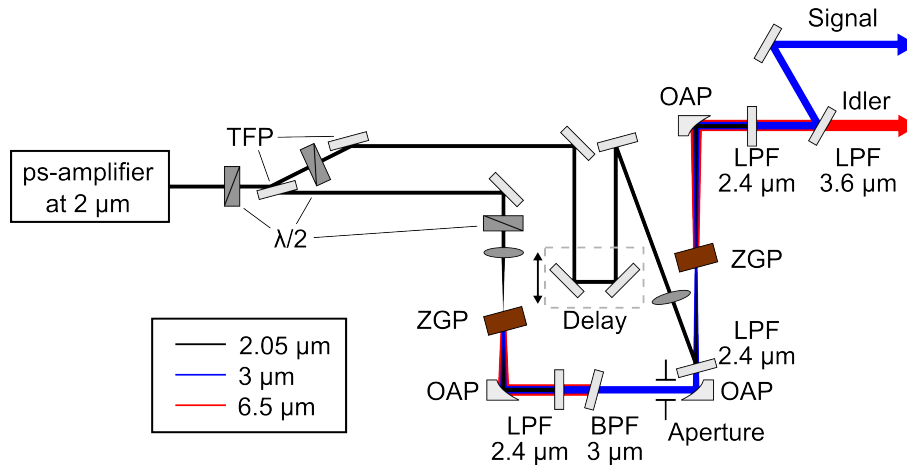


**Figure 5.9:** Experimental setup of the OPG/OPA tandem. OAP: off-axis parabolic mirror, TFP: thin-film polarizer, LPF: long-pass filter, BPF: band-pass filter,  $\lambda/2$ : half-wave plate.

A schematic of the experimental setup is shown in Figure 5.9. The OPG/OPA tandem consisted of the OPG stage introduced in Section 5.3 and an OPA pumped by the residual pump energy provided by the 2  $\mu\text{m}$  multipass amplifier described in Section 4.4. The nonlinear optical crystal was equal to one used in the OPG stage, and the parametric process was based on a type-I collinear phase-matching, as well. Approximately 4.8  $\mu\text{J}$  of pump pulse energy was used to produce signal and idler in the mid-IR spectral region via OPG. Due to the atmospheric absorption with discrete water absorption lines in the spectral vicinity around 2.6  $\mu\text{m}$  and a strong absorption features at 4.2  $\mu\text{m}$ , which is related to carbon dioxide, the signal wavelength was set to 3  $\mu\text{m}$  (see Figure 5.8). As the corre-

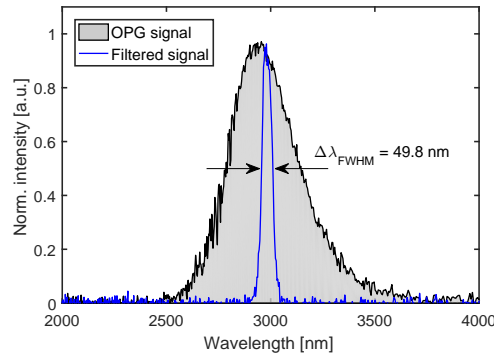


**Figure 5.10:** OPG signal spectrum set to a center wavelength of about 3  $\mu\text{m}$  (gray area) by proper adjustment of the phase-matching angle and seed spectrum filtered by a bandpass filter with FWHM transmission bandwidth of 60 nm.

sponding idler at 6.5  $\mu\text{m}$  was affected by water absorption, which may lead to temporal and spatial distortions of the pulse [Geb15b], the signal was used to seed the OPA stage instead. A bandpass filter with spectral transmission FWHM of 60 nm and peak transmittance of 80% selected only part of the OPG signal radiation in order to obtain high pulse energy confined in a narrow signal and idler bandwidth. At the same time, the coherence was enhanced, since OPGs naturally exhibit temporal incoherence [Wan16]. Furthermore, spatial filtering was performed with an adjustable hard aperture. The latter was required to fine-tune the mode-matching in the OPA stage, however, at the expense of some 3- $\mu\text{m}$  seed energy loss. The filtered OPA seed pulse spectrum in comparison to the initial OPG signal spectrum is shown in Figure 5.10. Temporal synchronization of pump and seed pulses was achieved by means of a delay stage. A lens with a focal length of 200 mm was chosen to realize a pump beam waist diameter of about 320  $\mu\text{m}$  inside the ZGP crystal. Note that this spot size is approximately three times the one used in the OPG stage in order to stay below the LIDT. An off-axis parabola mirror with longer focal distance of 100 mm was applied in the OPA stage to focus the mid-IR seed into the ZGP crystal and to account for the larger pump beam diameter in the focal area. The 2.05- $\mu\text{m}$  pump and 3- $\mu\text{m}$  signal radiation were collinearly combined via interference long-pass filter with a cut-on edge at 2.4  $\mu\text{m}$ . The three interacting waves were collimated via off-axis parabola mirror ( $f = 100$  mm) and separated by long-pass filters as explained in the previous section.

The signal and idler pulse energy in dependence on the pump pulse energy is shown in Figure 5.11(a). Any losses induced by the long-pass filters and the metallic mirrors are subtracted out. A maximum signal and idler pulse energy of 7.7  $\mu\text{J}$  and 2.5  $\mu\text{J}$  was achieved, respectively. Considering a pump pulse energy of 45  $\mu\text{J}$  this corresponds to an optical-to-optical efficiency of about 22.7% for the generation of the combined mid-IR radiation. It is worth mentioning that the maximum pump pulse energy in combination with the chosen spot size corresponds to an on-axis peak intensity of 6.6  $\text{GW}/\text{cm}^2$ . In fact, laser-induced damage was not observed during these experiments as this value is well below the LIDT as described in the previous section.

The output power stability was measured with a thermal laser power sensor over the course of 30 min (see Figure 5.11(b)). The rms noise for the signal and idler amounts to  $< 1.14\%$  and  $< 1.25\%$ , respectively. Note that the OPA noise is a superposition of the noise generated in the parametric process and the initial noise from the multipass amplifier, which was in the range of  $2\%$  (see Figure 4.15(a)). An explanation of the higher pump noise in comparison to the signal and idler noise can be attributed to the conversion process, which does not scale linearly with the pump power near pump depletion [Gua03]. In such a regime, pump power instabilities do not couple linearly to the signal and idler power instabilities. Additionally, it is worth mentioning that the generated mid-IR power exhibited a slightly higher initial value directly after the pump was increased. After a few minutes it converged against a stable level, which is described above. This behavior can be explained by an increasing temperature of the crystal due to some parasitic absorption of the interacting waves, particularly the pump radiation at a wavelength of  $2.05\ \mu\text{m}$ . As the temperature affects the refractive index, any change implies a different phase-matching condition, which in turn defines the efficiency of the parametric process. Here, the ZGP crystals were only clamped in a rotation mount without any efforts made to temperature stabilize them. The efficiency could be optimized again by fine-tuning of the phase-matching angle.

The corresponding beam profiles are depicted in the insets of Figure 5.11(b). The results show that the beam profiles differed significantly from a perfectly Gaussian intensity distribution. One possible explanation could be thermal lensing due to the linear residual absorption in the ZGP crystal. Considering a maximum pump power of  $4.5\ \text{W}$ , a focal beam waist radius of  $150\ \mu\text{m}$ , and thermo-mechanical properties of the ZGP crystal according to Table B.1 with  $dn/dT \sim 150 \times 10^{-6}\ \text{K}^{-1}$  [Boy71] yields a thermal lens of about  $150\ \text{mm}$  according to Equation (4.12). Plotting the  $1/e^2$  beam caustic for the propagation of the pump and signal radiation in the OPA (see Figure 5.12) reveals that such thermal lens had

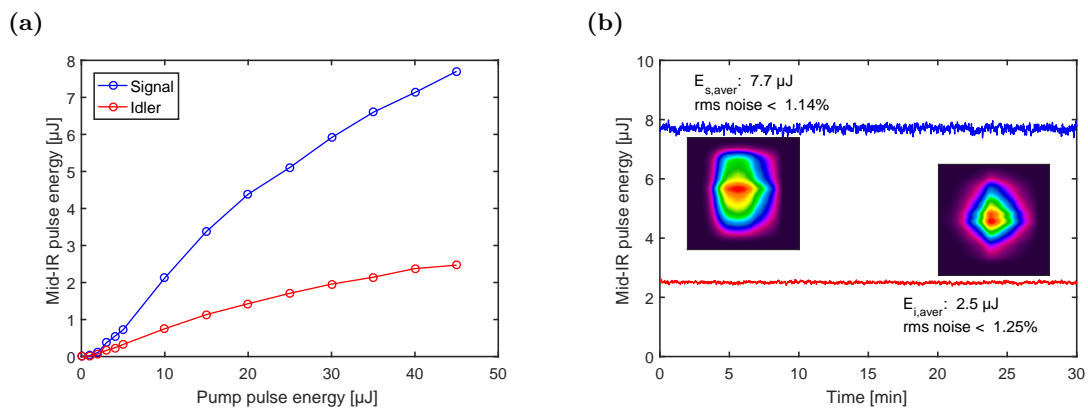


**Figure 5.11:** (a) Signal (blue) and idler (red) pulse energy in dependence of the pump pulse energy. (b) Long-term stability measurement of the signal and idler radiation at maximum pulse energy. Inset: Corresponding beam profile of the signal (left) and idler (right) beam.

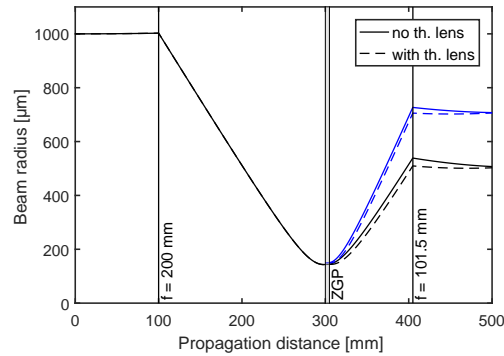


**Figure 5.12:** Evolution of the pump (black) and signal (blue)  $1/e^2$  beam radius during propagation in the OPA stage.

no significant impact, thus, being not responsible for beam distortions. More investigations are pending to clearly identify the origin of the observed signal and idler beam profile distortions.

With increasing pump intensity the signal and idler spectra broadened due to the onset of amplified parametric fluorescence (see Figure 5.13). At highest achieved pulse energy the signal FWHM was 125 nm, whereas the idler FWHM was 714 nm with a broadband spectral pedestal reaching from 4  $\mu\text{m}$  up to 9  $\mu\text{m}$ . The idler spectrum shows the characteristic water absorption features as mentioned above.

The pointing stability was measured as described in Section 3.5. An uncoated  $\text{BaF}_2$  lens was used to focus signal and idler beam to the automatized scanning slit beam

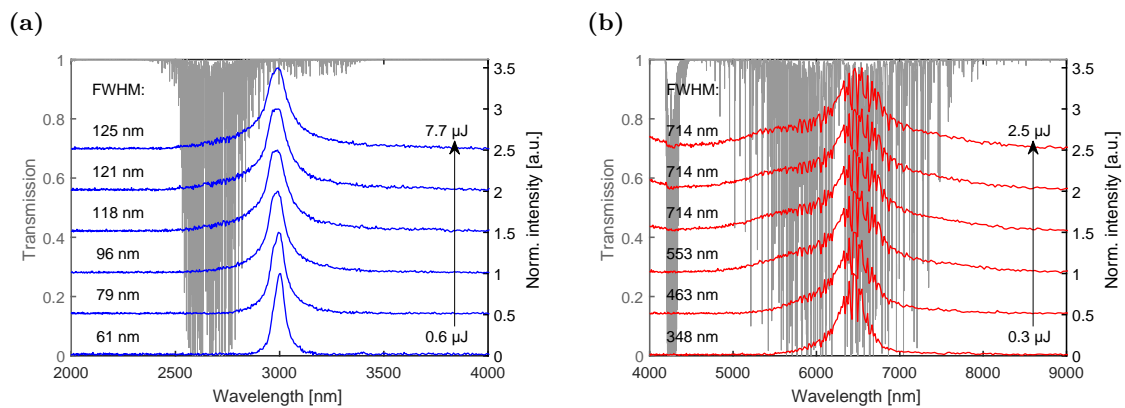


**Figure 5.13:** Measured optical spectrum in dependence on the amplified pulse energy for (a) the signal and (b) the idler radiation. Furthermore, the transmission for the propagation through 1 m in the laboratory environment is shown. The latter has been calculated for a room temperature of 20  $^{\circ}\text{C}$  and a relative humidity of 20 % based on the data provided by the HITRAN database [HIT19].

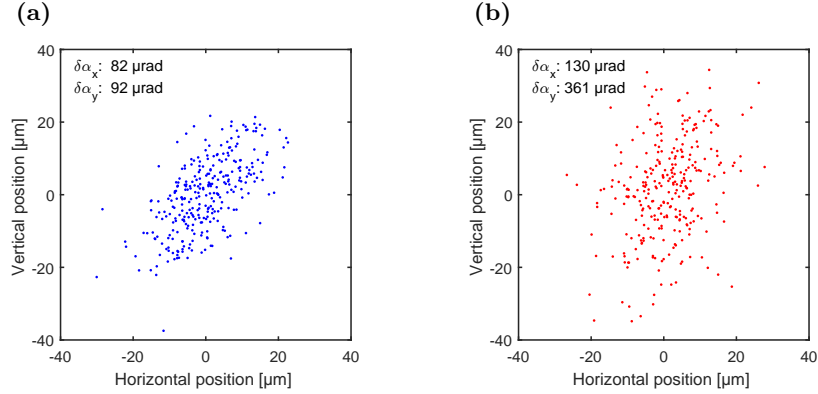


**Figure 5.14:** Measured pointing stability of (a) the signal at 3  $\mu\text{m}$  and (b) the idler at 6.5  $\mu\text{m}$  over a course of 5 min.

profiler with 5 Hz sampling rate. The collected data over the course of 5 min is given in Figures 5.14(a) and (b). In the case of the signal beam the standard deviation of the beam center position is 9  $\mu\text{m}$  and 10  $\mu\text{m}$  in horizontal and vertical position, respectively. The absolute idler pointing is comparably higher with 14  $\mu\text{m}$  and 40  $\mu\text{m}$ . Thus, the angular stability of the signal ( $\delta\alpha_x = 82 \mu\text{rad}$ ,  $\delta\alpha_y = 92 \mu\text{rad}$ ) is better than that of the idler ( $\delta\alpha_x = 130 \mu\text{rad}$ ,  $\delta\alpha_y = 361 \mu\text{rad}$ ). Taking into account the corresponding average focal beam waist diameters, the relative standard deviation for the signal is  $< 3.6\%$ , while it is  $< 9.9\%$  for the idler. The higher idler pointing can be attributed to the spectral location in the water absorption lines, which spatially distorts the beam or partly deflects it due to inhomogeneities of the moving air around the setup.

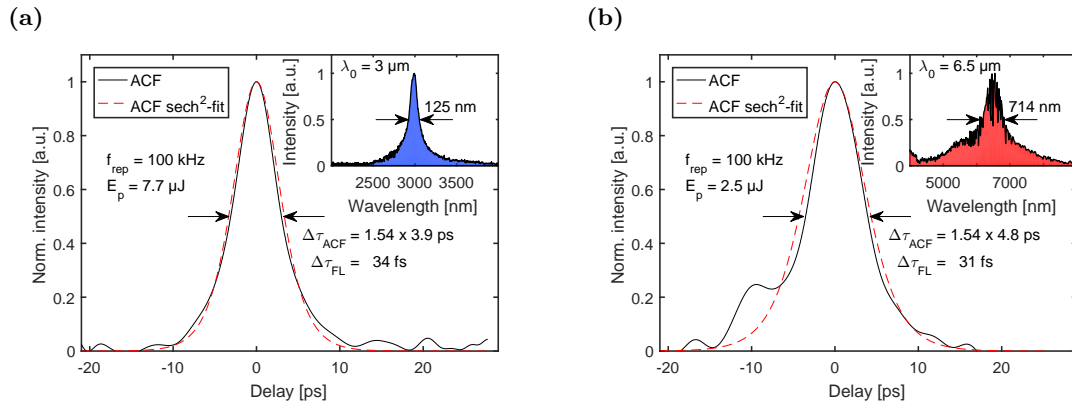


**Figure 5.15:** Measured autocorrelation of the (a) mid-IR signal at a wavelength of about 3  $\mu\text{m}$  and (b) idler at a wavelength of about 6.5  $\mu\text{m}$ . The inset shows the corresponding spectral distribution, respectively.  $\lambda_0$ : wavelength calculated by the center of gravity method.

The output pulse duration of the OPA was measured with an intensity autocorrelator based on two-photon absorption. Figures 5.15(a) and (b) show the autocorrelation traces for the signal and idler at highest output pulse energy, respectively. Assuming a



sech<sup>2</sup>-shaped pulse, it is 3.9 ps in the case of the signal and 4.8 ps for the idler. Note that the presented autocorrelations show some noise floor, especially in the case of the idler autocorrelation. However, the measured pulse durations are similar to the pump pulse duration (signal) or slightly longer (idler). Usually, a shortening of the pulse duration in comparison to the pump pulse duration is expected due to the nonlinear nature of the frequency down-conversion process. Here, the longer pulse duration, which is significant only in the case of the idler, can be attributed to the distorted pulse spectrum resulting in temporal pulse broadening as described in [Geb15b]. The corresponding pulse peak powers are about 2 MW for the signal at 3  $\mu\text{m}$  and 0.5 MW for the idler at 6.5  $\mu\text{m}$ . In the insets of Figures 5.15(a) and (b), the emission spectra are depicted. It is worth noting that signal and idler wavelength tuning of the system can be realized by changing the phase-matching conditions in the OPG and the OPA stage accordingly. Signal and idler center wavelengths covering the MWIR spectral range between 2.7 and 8  $\mu\text{m}$  have been shown in the previous Section 5.3. However, rotating the ZGP crystals affects the beam directions, which results in a misaligned signal and pump spatial mode-matching. Thus, appropriate beam realignment is required. Additionally, any OPG signal wavelength, which is affected by the molecular absorption, will result in temporal distortions of the pulse seeding the OPA stage. As a consequence, the synchronization of seed and pump pulses in the OPA stage is not optimal due to a decreased temporal overlap reducing the generated signal and idler pulse energy as well as their peak intensity.

## 5.5 Summary and outlook

This section successfully demonstrated the extension of the CPA-free approach to nonlinear frequency down-conversion in non-oxide crystals. Pulse energies in the  $\mu\text{J}$  range were achieved in a simplified, compact, and efficient OPG/OPA tandem configuration, maintaining sub-10 ps pulse duration. In principle, mid-IR laser radiation spanning the wavelength range from 2.5  $\mu\text{m}$  up to 9  $\mu\text{m}$  could be generated for an appropriate phase-matching condition. However, the optical parametric amplification is only optimal, when the pulse wavelength seeding the OPA stage is not affected by molecular absorption originating from water vapor and  $\text{CO}_2$ . In order to preserve the temporal and spatial pulse shape even for the aforementioned broad spectral tuning, purging with dry air or pure nitrogen might be necessary.

Even higher pulse energies seem to be feasible as it has been shown that the 2  $\mu\text{m}$  pump source is scalable towards the mJ-level, which corresponds to a 20-fold increase of available pump energy compared to the one used here. However, a second OPA stage with increased laser spot size might be necessary in order to mitigate laser-induced damage to the nonlinear crystal. In parallel, the beam profile after the OPA stage needs to be improved significantly. Further investigations are necessary to clarify, where the distorted beam profile originated from.

For the coherent generation of broadband mid-IR seed pulses, the OPG stage can be substituted by supercontinuum generation. Just recently, it has been shown that ps pump

sources with emission at  $2\ \mu\text{m}$  are able to generate sufficient mid-IR seed radiation in rather long YAG crystals [Che18]. Pump pulse energies in the range of  $100\ \mu\text{J}$  are required to trigger the filamentation process. The supercontinuum generation benefits from its coherent nature in comparison to the OPG process, which is based on the amplification of quantum noise. In combination with proper temporal pulse compression, much shorter pulse durations can be expected with this method.

Many applications demand for narrow linewidth mid-IR generation to address specific resonant absorption features of molecules or materials. Type-II phase-matching offers a much narrower gain bandwidth for the parametric conversion process, however, at the expense of a limited wavelength tuning range [Vod93]. Just recently, BAUDISCH et al. presented a ZGP-based OPG/OPA system tunable in the mid-IR wavelength range of  $2.5\ \mu\text{m}$ – $12\ \mu\text{m}$  [Bau19]. The parametric down-conversion was pumped by a similar multipass amplifier with emission at  $2.05\ \mu\text{m}$  (see Section 4.4) as described in [Hin18b]. Pulse energies at  $\mu\text{J}$ -level maintaining narrowband ( $< 20\ \text{cm}^{-1}$ ), ultrashort ( $< 7\ \text{ps}$ ) pulses have been achieved, showing the capabilities of these simplified CPA-free laser systems addressing specific absorption bands of polymers and organic molecules.

# CHAPTER 6

---

## Conclusion

---

In this thesis a CPA-free amplification of sub-10 ps pulses at a wavelength around 2  $\mu\text{m}$  up to the mJ-level was presented for the first time. The system consisted of an all-fiber MOPA based on holmium-doped silica fiber, an acousto-optic pulse picker, and multipass amplifiers based on highly doped Ho:YLF crystals. It was operated at room temperature with no significant efforts made to shield the system from environmental influences in order to keep the architecture simple, compact, reliable, and low-maintenance.

Low-energy pulses centered at 2.05  $\mu\text{m}$  were generated in an all-fiber ultrashort pulse oscillator. Hybrid mode-locking based on the combination of nonlinear polarization rotation and saturable absorption by means of semiconductor saturable absorber mirrors resulted in a self-starting and stable pulse train with a pulse repetition frequency of 20 MHz. It is worth mentioning that hybrid mode-locking of an all-fiber holmium laser has recently been presented by FILATOVA et al. [Fil18]. However, the developed ultrashort pulse oscillator described in this thesis is the first all-fiber holmium laser based on hybrid mode-locking operating in the stretched-pulse regime. A narrow bandwidth wavelength-division multiplexer was used to force the oscillator to emit at the central wavelength of 2.05  $\mu\text{m}$ , which meets the spectral requirements to seed subsequent amplifiers based on Ho:YLF crystals. The relative intensity noise (RIN) was measured yielding  $< 0.02\%$  rms in the frequency range up to 10 MHz, which is almost an order of magnitude lower than previously reported ultrafast oscillators with free-space sections [Li14]. The ps-pulses were pre-amplified in an all-fiber amplifier towards 40 nJ of pulse energy with a slope efficiency of 67% maintaining an ultrashort and stable pulse duration of 5.7 ps. The MOPA beam quality revealed excellent characteristics with  $M^2 < 1.16$  and a pointing stability of  $< 31\ \mu\text{rad}$ . The integrated RIN at an average output power of 500 mW was  $< 0.1\%$  rms, which can be mainly attributed to the noise induced by the fiber-based pump source.

Regenerative amplifiers are typically limited to pulse repetition rates below some tens of kHz due to switching constraints in the high voltage-driven Pockels cells [Ber15] or bifurcation effects [Dör04; Gri07]. In contrast, an acousto-optic modulator was used in this thesis to set the pulse repetition frequency from the fundamental 20 MHz down to the kHz-rates. The following crystal-based main amplifier was split into two parts: a high-gain multipass amplification stage and a single-pass booster. The design was carefully tailored to handle the prevalent high peak power, which potentially triggers severe nonlinear effects such as self-focusing or the laser-induced damage. As conventional doping concentrations between 0.5

and 1.0 at.% are not sufficient to provide the required gain for compact CPA-free multipass amplifiers, high doping concentrations up to 1.5at.% were used. Preliminary investigations of lifetime quenching in highly doped Ho:YLF crystals showed a reduction of 60 % from initially 14.6 ms to 5.7 ms at an excitation intensity of 76 kW/cm<sup>2</sup>. Nevertheless, up to 100 μJ of pulse energy were generated in an 8-fold amplification scheme at 50 kHz repetition rate corresponding to a gain factor of 41 dB. The maximum pulse duration was limited by the onset of laser-induced damage in the bulk material. The measured pulse duration was 4 ps, which corresponds to a peak power of 24 MW. Due to spectral filtering of the chirped pulses by the finite gain bandwidth, the pulse duration of the amplified signal was smaller than the one of the fiber front-end. Further investigations covered an analysis of the pulse repetition rate tuning between 10 kHz up to 20 MHz. In comparison to the fiber-based seed source, the multipass amplifier did not exhibit any significant power stability or beam quality reduction. The long-term stability at a power level of 5 W (100 kHz) was < 2 %, while the  $M^2$  and pointing noise was nearly unaffected with respect to the seed output characteristics.

Further energy scaling required a detailed analysis of the pulse evolution within crystal-based amplifiers. Therefore, numerical simulations based on a modified Frantz-Nodvik formalism revealed an amplifier design capable of generating mJ-level ultrashort pulses in a CPA-free architecture. Experimentally, the consecutive single-pass booster amplifier generated about 1.2 mJ of pulse energy at 1 kHz repetition rate maintaining sub-10 ps pulse duration. A pulse peak power of 136 MW is the highest reported for a CPA-free ultrashort pulse amplifier system with emission in the 2 μm region so far. While the optical-to-optical efficiency is comparably low at 1 kHz with 7.4 %, it is 39 % at 100 kHz, however, at the expense of a reduced pulse energy of 106 μJ. These experimental results agreed well with the theoretical predictions from the numerical simulations.

The developed 2 μm system was used as front-end to pump an OPG/OPA-tandem configuration based on highly nonlinear non-oxide ZGP crystals. First, mid-infrared seed generation was conducted in a standing-wave optical parametric generator. Wavelength tuning between 2.5 and 8 μm was achieved, limited only by the transmission characteristics of the ZGP crystal itself or by the interferometric filters used in the experimental setup. The OPG threshold intensity was roughly 10 GW/cm<sup>2</sup> with a slope efficiency of 30 % considering the combined signal and idler output power. Laser-induced damage occurred at on-axis peak intensities exceeding 45 GW/cm<sup>2</sup>, which is in line with recently reported values taking into account the square root scaling law [Vod93].

By choosing the proper phase-matching angle of 53°, the signal wavelength was set to 3 μm in the OPG stage. The latter was used to seed an OPA, which was pumped by the residual pulse energy of 45 μJ from the 2 μm pump source. A maximum signal and idler pulse energy of 7.7 μJ and 2.5 μJ was achieved, respectively. Considering the maximum OPA pump pulse energy of 45 μJ this yields an optical-to-optical efficiency of about 23 %. A long-term power stability measurement revealed a root-mean square noise of < 1.25 %, which is less than the pump power noise. This can be explained by the nonlinear scaling behavior of the conversion efficiency near pump depletion [Gua03]. The measured

autocorrelation trace for signal and idler beam revealed a  $\text{sech}^2$ -based pulse duration of 3.9 ps and 4.8 ps, respectively. These values correspond to a pulse peak power of about 2 MW for the signal at 3  $\mu\text{m}$  and 0.5 MW for the idler centered at 6.5  $\mu\text{m}$ .



# CHAPTER 7

---

## Outlook

---

The developed laser system described in this thesis represents a simplified route towards the direct generation of intense radiation in the spectral vicinity around  $2\ \mu\text{m}$ . It represents the most promising technical concept for ultrashort pulse lasers, which paves the way to cost effective industrial micromachining. Major challenges arising for CPA-free amplification schemes have been addressed. The laser source has been successfully used to pump nonlinear frequency conversion stages based on optical parametric generation and amplification to approach the mid-infrared spectral region. However, further research regarding the following aspects is still pending and will push this technology towards commercial availability.

Scaling the  $2\ \mu\text{m}$  peak intensity can be realized by additional booster stages, which are carefully tailored to mitigate laser-induced damage and nonlinear effects. Especially the latter might be an ultimate limit in the CPA-free approach, as self-focusing is not dependent on the beam size, but rather on the peak power and the propagation length. In this thesis, the generated pulse peak powers were already a multiple of the critical power associated with Ho:YLF crystals and further investigation in terms of potential peak power scaling is needed. Amplifiers utilizing short, highly doped crystals remain indispensable in such architectures to approach the GW-regime.

Scaling the average output power can be easily achieved by means of high power ( $> 100\ \text{W}$ ) commercially available pump sources emitting at  $1940\ \text{nm}$  [Fut19; Pho19] without any additional setup variation. Nowadays, these pump sources are still rather cost intensive. Special attention has to be focused on the thermal lens in the Ho:YLF crystal and water vapor absorption in the spectral vicinity of the pump emission. The latter can strongly affect the overall stability of an amplifier, which demands for proper housing and purging of the beam line at the expense of an increased system complexity. In principle, several tens of W of output power will be a unique feature to ultrashort pulse laser amplifiers around  $2\ \mu\text{m}$  with pulse energies in the mJ-range.

Shorter pulse durations at  $2\ \mu\text{m}$  can be achieved by nonlinear pulse compression in gas-filled hollow-core photonic crystal fibers, which was demonstrated by BALCIUNAS et al. [Bal15], GEBHARDT et al. [Geb15a][Geb17] just recently. Pulse energies in the range of  $100\ \mu\text{J}$  are required to trigger the nonlinear spectral broadening process in such fibers, which supports few-optical-cycle pulse duration after proper temporal compression. As the attained peak intensity approaches electric field strengths on the order of the molecule

binding energy of gaseous media ( $10^{13}$  to  $10^{14}$  GW/cm<sup>2</sup>), strong-field experiments like high-harmonic generation become possible.

As already mentioned in the previous chapter, the OPG stage can be substituted by a supercontinuum generation. The latter benefits from its coherent spectral broadening, which can be used to achieve sub-fs pulse durations as seed for an OPA process. In addition, deriving the pump and seed pulses in the OPA from the same front-end enables the generation of passive carrier-envelope phase-stable idler pulses in the LWIR spectral region with few-optical-cycle pulse duration. This concept, however, requires vacuum technology or purging with dry gas in order to prevent spatial and temporal pulse degradation due to molecular absorption.



---

## Bibliography

---

- [Ada89] ADAIR, R., L. L. CHASE, and S. A. PAYNE: ‘Nonlinear refractive index of optical crystals’. *Phys. Rev. B* (1989), vol. 39(5): pp. 3337–3350 (cit. on p. 35).
- [Ada92] ADAIR, R., L. L. CHASE, and S. A. PAYNE: ‘Disersion of the nonlinear refractive index of optical crystals’. *Optical Materials* (1992), vol. 1(3): pp. 185–194 (cit. on p. 35).
- [Agg05] AGGARWAL, R. L., D. J. RIPIN, J. R. OCHOA, and T. Y. FAN: ‘Measurement of thermo-optic properties of  $Y_3Al_5O_{12}$ ,  $Lu_3Al_5O_{12}$ ,  $YAlO_3$ ,  $LiYF_4$ ,  $LiLuF_4$ ,  $BaY_2F_8$ ,  $KGd(WO_4)_2$ , and  $KY(WO_4)_2$  laser crystals in the 80-300 K temperature range’. *J. Appl. Phys.* (2005), vol. 98: p. 103514 (cit. on p. 35).
- [Agr12] AGRAWAL, GOVIND: *Nonlinear Fiber Optics*. 5th ed. Elsevier, 2012 (cit. on pp. 9, 11–15, 23).
- [All09] ALLAKHVERDIEV, K. R., M. Ö. YETIS, S. ÖZBEK, T. K. BAYKARA, and E. YU. SALAEV: ‘Effective Nonlinear GaSe Crystal. Optical Properties and Applications’. *Laser Phys.* (2009), vol. 19(5): pp. 1092–1104 (cit. on p. 65).
- [Bal15] BALCIUNAS, T., C. FOURCADE-DUTIN, G. FAN, T. WITTING, A. A. VORIN, A. M. ZHELTIKOV, F. GEROME, G. G. PAULUS, A. BALTUSKA, and F. BEN-ABID: ‘A strong-field driver in the single-cycle regime based on self-compression in a kagome fibre’. *Nat. Commun.* (2015), vol. 6: p. 6117 (cit. on p. 81).
- [Bar73] BARKER, A. S. and M. ILEGEMS: ‘Infrared Lattice Vibrations and Free-Electron Dispersion in GaN’. *Phys. Rev. B* (1973), vol. 7(2): pp. 743–750 (cit. on p. 115).
- [Bar03] BARNES, N. P., B. M. WALSH, and E. D. FILER: ‘Ho:Ho upconversion: applications to Ho lasers’. *J. Opt. Soc. Am. B* (2003), vol. 20(6): pp. 1212–1219 (cit. on p. 37).
- [Bau19] BAUDISCH, M., M. HINKELMANN, D. WANDT, K. ZAWILSKI, P. SCHUNEMANN, J. NEUMANN, and I. RIMKE: ‘2.5-12  $\mu\text{m}$  tunable, 2  $\mu\text{m}$  pumped,  $ZnGeP_2$ -based OPG/OPA System for the generation of narrowband,  $\mu\text{J}$ -level pulses with sub-20  $\text{cm}^{-1}$  bandwidth’. *2019 European Conference on Lasers and Electro-Optics - European Quantum Electronics Conference*. 2019: CF-7.3 (cit. on p. 76).
- [Bea94] BEASLEY, J. D.: ‘Thermal conductivities of some novel nonlinear optical materials’. *Appl. Optics* (1994), vol. 33(6): pp. 1000–1003 (cit. on p. 115).
- [Ber15] BERGMANN, F., M. SIEBOLD, M. LOESER, F. RÖSER, D. ALBACH, and U. SCHRAMM: ‘MHz Repetition Rate Yb:YAG and Yb:CaF<sub>2</sub> Regenerative Picosecond Laser Amplifiers with a BBO Pockels Cell’. *Appl. Sci.* (2015), vol. 5: pp. 761–769 (cit. on pp. 30, 77).

- [Bet76] BETTIS, J. R., R. A. HOUSE II, and A. H. GUENTHER: ‘Spot Size and Pulse Duration Dependence of Laser-Induced Damage’. *Laser Induced Damage in Optical Materials*. NBS Spec. Pub. 462 (US GPO, Washington, D.C.), 1976: pp. 338–345 (cit. on pp. 37, 68).
- [Bey04] BEYERTT, A., D. MÜLLER, D. NICKEL, and A. GIESEN: ‘CPA-free femtosecond thin disk Yb:KYW regenerative amplifier with high repetition rate’. *ASSP: 2004* (2004), vol.: p. 231 (cit. on p. 32).
- [Bon65] BOND, W. L.: ‘Measurement of the Refractive Indices of Several Crystals’. *J. Appl. Phys.* (1965), vol. 36(5): pp. 1674–1677 (cit. on p. 115).
- [Bow14] BOWMAN, S. R., C. G. BROWN, M. BRINDZA, G. BEADIE, J. K. HITE, J. A. FREITAS, C. R. EDDY JR., J. R. MEYER, and I. VURGAFTMAN: ‘Broadband measurement of the refractive indices of bulk gallium nitride’. *Opt. Mat. Express* (2014), vol. 4(7): pp. 1287–1296 (cit. on p. 115).
- [Boy65] BOYD, G. D., A. ASHKIN, J. M. DZIEDZIC, and D. A. KLEINMAN: ‘Second-Harmonic Generation of Light with Double Refraction’. *Phys. Rev.* (1965), vol. 137(4A): pp. 1305–1320 (cit. on p. 63).
- [Boy71] BOYD, G. D., E. BUEHLER, and F. G. STORZ: ‘Linear and nonlinear optical properties of ZnGeP<sub>2</sub> and CdSe’. *Appl. Phys. Lett.* (1971), vol. 18(7): pp. 301–304 (cit. on pp. 65, 72, 115).
- [Boy72] BOYD, G. D., E. BUEHLER, F. G. STORZ, and J. H. WERNICK: ‘Linear and Nonlinear Optical Properties of Ternary A<sup>II</sup> B<sup>IV</sup> C<sub>2</sub><sup>V</sup> Chalcopyrite Semiconductors’. *IEEE J. Quantum Electron.* (1972), vol. 8(4): pp. 419–426 (cit. on p. 65).
- [Boy08] BOYD, ROBERT W.: *Nonlinear Optics*. 3rd ed. Academic Press, 2008 (cit. on pp. 57, 115).
- [Bre89] BRENIER, A., J. RUBIN, R. MONCORGE, and C. PEDRINI: ‘Excited-state dynamics of the Tm<sup>3+</sup> ions and Tm<sup>3+</sup> → Ho<sup>3+</sup> energy transfers in LiYF<sub>4</sub>’. *J. Phys. France* (1989), vol. 50: pp. 1463–1482 (cit. on p. 35).
- [But19] BUTLER, T. P. et al.: ‘Watt-scale 50-MHz source of single-cycle waveform-stable pulses in the molecular fingerprint region’. *Opt. Lett.* (2019), vol. 44(7): pp. 1730–1733 (cit. on p. 66).
- [Car00] CARRION, L. and J.-P. GIRARDEAU-MONTAUT: ‘Development of a simple model for parametric generation’. *J. Opt. Soc. Am. B* (2000), vol. 17(1): pp. 78–83 (cit. on p. 59).
- [Cas19] CASTECH: *KTA crystal product information*. Accessed on 01.08.2019. 2019. URL: <http://www.castech.com/productsinfo.aspx?id=117&selectIndex=0> (cit. on p. 115).
- [Cas75] CASTLEBERRY, D. E. and A. LINZ: ‘Measurement of the refractive indices of LiYF<sub>4</sub>’. *Appl. Optics* (1975), vol. 14(9): p. 2056 (cit. on p. 35).

- 
- [Cha12a] CHAMOROVSKIY, A., A. V. MARAKULIN, S. RANTA, M. TAVAST, J. RAUTIAINEN, T. LEINONEN, A. S. KURKOV, and O. G. OKHOTNIKOV: ‘Femtosecond mode-locked holmium fiber laser pumped by semiconductor disk laser’. *Opt. Lett.* (2012), vol. 37(9): pp. 1448–1450 (cit. on p. 19).
- [Cha12b] CHAMOROVSKIY, A. Y., A. V. MARAKULIN, A. S. KURKOV, and O. G. OKHOTNIKOV: ‘Tunable Ho-doped soliton fiber laser mode-locked by carbon nanotube saturable absorber’. *Laser Phys. Lett.* (2012), vol. 9(8): p. 602 (cit. on p. 19).
- [Che18] CHENG, S., G. CHATTERJEE, F. TELLKAMP, A. RUEHL, and R. J. DWAYNE MILLER: ‘Multi-octave supercontinuum generation in YAG pumped by mid-infrared, multi-picosecond pulses’. *Opt. Lett.* (2018), vol. 43(18): pp. 4329–4332 (cit. on pp. 66, 76).
- [Cho08] CHONG, A., W. H. RENNINGER, and F. W. WISE: ‘Properties of normal-dispersion femtosecond fiber lasers’. *J. Opt. Soc. Am. B* (2008), vol. 25(2): pp. 140–148 (cit. on p. 14).
- [Chu14] CHURIN, D., K. KIEU, R. A. NORWOOD, and N. PEYGHAMBARIAN: ‘Efficient Frequency Comb Generation in the 9- $\mu\text{m}$  Region Using Compact Fiber Sources’. *IEEE Photon. Technol. Lett.* (2014), vol. 26(22): pp. 2271–2274 (cit. on p. 66).
- [Col11] COLUCELLI, N., A. GAMBETTA, D. GATTI, M. MARANGONI, A. DI LIETO, M. TONELLI, G. GALZERANO, and P. LAPORTA: ‘1.6-W self-referenced frequency comb at 2.06  $\mu\text{m}$  using a Ho:YLF multipass amplifier’. *Opt. Lett.* (2011), vol. 36(12): pp. 2299–2301 (cit. on p. 6).
- [DeM66] DEMARIA, A. J., D. A. STETSER, and H. HEYNAU: ‘Self mode-locking of laser with saturable absorbers’. *Appl. Phys. Lett.* (1966), vol. 8: pp. 174–176 (cit. on p. 16).
- [Der13] DERGACHEV, A.: ‘High-energy, kHz-rate, picosecond, 2- $\mu\text{m}$  laser pump source for mid-IR nonlinear optical devices’. *Proc. SPIE 8599, Solid State Lasers XXII: Technology and Devices*. 2013: 85990B (cit. on p. 5).
- [Die06] DIELS, J.-C. and W. RUDOLPH: *Ultrashort Laser Pulse Phenomena*. 2nd ed. Academic Press, 2006 (cit. on pp. 57, 63).
- [Dmi99] DMITRIEV, V. G., G. G. GURZADYAN, and D. N. NIKOGOSYAN: *Handbook of Nonlinear Optical Crystals*. Springer, 1999 (cit. on p. 61).
- [Dör04] DÖRRING, J., A. KILLI, U. MORGNER, A. LANG, M. LEDERER, and D. KOPF: ‘Period doubling and deterministic chaos in continuously pumped regenerative amplifiers’. *Opt. Express* (2004), vol. 12(8): pp. 1759–1768 (cit. on pp. 30, 77).
- [Du94] DU, D., X. LIU, G. KORN, J. SQUIR, and G. MOUROU: ‘Laser-induced breakdown by impact ionization in  $\text{SiO}_2$  with pulse widths from 7 ns to 150 fs’. *Appl. Phys. Lett.* (1994), vol. 64(23): pp. 3071–3073 (cit. on p. 37).

- [Dvo15] DVOYRIN, V., N. TOLSTIK, E. SOROKIN, I. SOROKINA, and A. KURKOV: ‘Graphene-mode-locked Holmium Fiber Laser Operating Beyond 2.1  $\mu\text{m}$ ’. *CLEO Europe*. Optical Society of America, 2015: CJ-7-4 (cit. on p. 19).
- [Edw03] EDWARDS, G. S. et al.: ‘Free-electron-laser-based biophysical and biomedical instrumentation’. *Rev. Scientific Instruments* (2003), vol. 74(7): p. 3207 (cit. on p. 1).
- [Elu19] ELU, U., T. STEINLE, D. SÁNCHEZ, L. MAIDMENT, K. ZAWILSKI, P. SCHUNEMANN, U. D. ZEITNER, C. SIMON-BOISSON, and J. BIEGERT: ‘Table-top high-energy 7  $\mu\text{m}$  OPCPA and 260 mJ Ho:YLF pump laser’. *Opt. Lett.* (2019), vol. 44(13): pp. 3194–3197 (cit. on p. 7).
- [Fen95] FENIMORE, D. L., K. L. SCHEPLER, U. B. RAMABADRAN, and S. R. MCPHERSON: ‘Infrared corrected Sellmeier coefficients for potassium titanyl arsenate’. *J. Opt. Soc. Am. B* (1995), vol. 12(5): pp. 794–796 (cit. on p. 115).
- [Fer98] FERMAN, M. E.: ‘Single-mode excitation of multimode fibers with ultrashort pulses’. *Opt. Lett.* (1998), vol. 23(1): pp. 52–54 (cit. on p. 28).
- [Fer93] FERMAN, M. E., M. J. ANDREJCO, Y. SILBERBERG, and M. L. STOCK: ‘Passive mode locking by using nonlinear polarization evolution in a polarization-maintaining erbium-doped fiber’. *Opt. Lett.* (1993), vol. 18(11): pp. 894–896 (cit. on p. 17).
- [Fer13] FERMAN, M. E. and I. HARTL: ‘Ultrafast fibre lasers’. *Nature Photonics* (2013), vol. 7: pp. 868–874 (cit. on p. 16).
- [Fil18] FILATOVA, S. A., V. A. KAMYNIN, N. R. ARUTYUNYAN, A. S. POZHAROV, A. I. TRIKSHEV, I. V. ZHLUTKOVA, I. O. ZOLOTOVSKII, E. D. OBRAZTSOVA, and V. B. TSVETKOV: ‘Hybrid mode-locking of an all-fiber holmium laser’. *J. Opt. Soc. Am. B* (2018), vol. 35(12): pp. 3122–3125 (cit. on pp. 22, 77).
- [Fil15] FILATOVA, S. A., V. A. KAMYNIN, V. B. TSVETKOV, O. I. MEDVEDKOV, and A. S. KURKOV: ‘Gain spectrum of the Ho-doped fiber amplifier’. *Laser Phys. Lett.* (2015), vol. 12(9) (cit. on p. 29).
- [Fil16] FILATOVA, S. A., V. A. KAMYNIN, I. V. ZHLUKTOVA, A. I. TRIKSHEV, and V. B. TSVETKOV: ‘All-fiber passively mode-locked Ho-laser pumped by ytterbium fiber laser’. *Laser Phys. Lett.* (2016), vol. 13: p. 115103 (cit. on p. 19).
- [Fon13] FONNUM, H., E. LIPPERT, and M. W. HAAKESTEDT: ‘550 mJ Q-switched cryogenic Ho:YLF oscillator pumped with a 100 W Tm: fiber laser’. *Opt. Lett.* (2013), vol. 38(11): pp. 1884–1886 (cit. on p. 41).
- [Fra61] FRANKEN, P. A., A. E. HILL, C. W. PETERS, and G. WEINREICH: ‘Generation of optical harmonics’. *Phys. Rev. Lett.* (1961), vol. 7(4): pp. 118–119 (cit. on p. 58).
- [Fra63] FRANTZ, L. M. and J. S. NODVIK: ‘Theory of pulse propagation in a laser amplifier’. *J. Appl. Phys.* (1963), vol. 34(8): pp. 2346–2350 (cit. on p. 30).

- 
- [Fu18] FU, W., L. G. WRIGHT, P. SIDORENKO, S. BACKUS, and F. W. WISE: ‘Several new directions for ultrafast fiber lasers’. *Opt. Express* (2018), vol. 26(8): pp. 9432–9463 (cit. on p. 14).
- [Fut19] FUTONICS: *2  $\mu\text{m}$  Thulium Fiber Laser*. 2019. URL: <https://www.fotonics.de/wp-content/uploads/2019/02/Fotonics250W.pdf> (visited on 08/20/2019) (cit. on p. 81).
- [Gai18] GAIDA, C., M. GEBHARDT, T. HEUERMANN, F. STUTZKI, C. JAUREGUI, J. ANTONIO-LOPEZ, A. SCHÜLZGEN, R. AMEZCUA-CORREA, A. TÜNNERMANN, I. PUPEZA, and J. LIMPET: ‘Watt-scale super-octave mid-infrared intrapulse difference frequency generation’. *Light: Science & Applications* (2018), vol. 7(94): pp. 1–8 (cit. on p. 66).
- [Gar17] GAREJEV, N., G. TAMOSAUSKAS, and A. DUBIETIS: ‘Comparative study of multioctave supercontinuum generation in fused silica, YAG, and LiF in the range of anomalous group velocity dispersion’. *J. Opt. Soc. Am. B* (2017), vol. 34(1): pp. 88–94 (cit. on p. 66).
- [Gar09] GARRETT-ROE, S. and P. HAMM: ‘Purely absorptive three-dimensional infrared spectroscopy’. *J. Chem. Phys.* (2009), vol. 130: pp. 164510-1–9 (cit. on p. 2).
- [Geb15a] GEBHARDT, M., C. GAIDA, S. HÄDRICH, F. STUTZKI, C. JAUREGUI, J. LIMPET, and A. TÜNNERMANN: ‘Nonlinear compression of an ultrashort-pulse thulium-based fiber laser to sub-70 fs in Kagome photonic crystal fiber’. *Opt. Lett.* (2015), vol. 40(12): pp. 2770–2773 (cit. on p. 81).
- [Geb17] GEBHARDT, M., C. GAIDA, T. HEUERMANN, F. STUTZKI, C. JAUREGUI, J. ANTONIO-LOPEZ, A. SCHULZGEN, R. AMEZCUA-CORREA, J. LIMPET, and A. TÜNNERMANN: ‘Nonlinear pulse compression to 43 W GW-class few-cycle pulses at 2  $\mu\text{m}$  wavelength’. *Opt. Lett.* (2017), vol. 42(20): pp. 4179–4182 (cit. on pp. 6, 81).
- [Geb15b] GEBHARDT, M., C. GAIDA, F. STUTZKI, S. HÄDRICH, C. JAUREGUI, J. LIMPET, and A. TÜNNERMANN: ‘Impact of atmospheric molecular absorption on the temporal and spatial evolution of ultra-short optical pulses’. *Opt. Express* (2015), vol. 23(11): pp. 13776–13787 (cit. on pp. 2, 33, 71, 75).
- [Geh14] GEHLICH, N., T. BONHOFF, L. SISKEN, M. RAMM, C. GAIDA, M. GEBHARDT, I. MINGAREEV, L. SHAH, and M. C. RICHARDSON: ‘Utilizing the transparency of semiconductors via backside machining with nanosecond 2  $\mu\text{m}$  Tm: fiber laser’. *Proc. SPIE 8968, Laser-based Micro- and Nanoprocessing VIII*. 2014: 89680W (cit. on p. 2).
- [Gio62] GIORDMAINE, J. A.: ‘Mixing of light beams in crystals’. *Phys. Rev. Lett.* (1962), vol. 8(1): p. 19 (cit. on p. 61).
- [Gio65] GIORDMAINE, J. A. and R. C. MILLER: ‘Tunable coherent parametric oscillation in LiNbO<sub>3</sub> at optical frequencies’. *Phys. Rev. Lett.* (1965), vol. 14: pp. 973–976 (cit. on p. 59).

- [Gol02] GOLAB, S., P. SOLARZ, G. DOMINIAK-DZIK, T. LUKASIEWICZ, and W. RYBAROMANOWSKI: ‘Optical properties of YVO<sub>4</sub> crystals singly doped with Er<sup>3+</sup>, Ho<sup>3+</sup>, Tm<sup>3+</sup>’. *J. of Alloys and Compounds* (2002), vol. 341: pp. 165–169 (cit. on p. 34).
- [Gra16] GRAFENSTEIN, L. von, M. BOCK, G. STEINMEYER, U. GRIEBNER, and T. ELSAESSER: ‘Taming chaos: 16 mJ picosecond Ho:YLF regenerative amplifier with 0.7 kHz repetition rate’. *Laser Photonics Rev.* (2016), vol. 10(1): pp. 123–130 (cit. on pp. 31, 32).
- [Gra15] GRAFENSTEIN, L. von, M. BOCK, D. UEBERSCHAER, U. GRIEBNER, and T. ELSAESSER: ‘Picosecond 34 mJ pulses at kHz repetition rates from a Ho:YLF amplifier at 2 μm wavelength’. *Opt. Express* (2015), vol. 23(26): pp. 33142–33149 (cit. on p. 5).
- [Gra17] GRAFENSTEIN, L. von, M. BOCK, D. UEBERSCHAER, K. ZAWILSKI, P. SCHUNEMANN, U. GRIEBNER, and T. ELSAESSER: ‘5 μm few-cycle pulses with multi-gigawatt peak power at a 1 kHz repetition rate’. *Opt. Lett.* (2017), vol. 42(19): pp. 3796–3799 (cit. on p. 7).
- [Gre12] GRELU, P. and N. AKHMEDIEV: ‘Dissipative solitons for mode-locked lasers’. *Nature Photonics* (2012), vol. 6: pp. 84–92 (cit. on p. 14).
- [Gri07] GRISHIN, M., V. GULBINAS, and A. MICHAIOVAS: ‘Dynamics of high repetition rate regenerative amplifiers’. *Opt. Expr.* (2007), vol. 15(15): pp. 9434–9443 (cit. on pp. 30, 77).
- [Gua03] GUARDALBEN, M. J., J. KEEGAN, L. J. WAXER, V. BAGNOUD, I. A. BEGISHEV, J. PUTH, and J. D. ZUEGEL: ‘Design of a highly stable, high-conversion-efficiency, optical parametric chirped-pulse amplification system with good beam quality’. *Opt. Express* (2003), vol. 11(20): pp. 2511–2524 (cit. on pp. 70, 72, 78).
- [Hai04] HAIML, M., R. GRANGE, and U. KELLER: ‘Optical characterization of semiconductor saturable absorbers’. *Appl. Phys. B* (2004), vol. 79: pp. 331–339 (cit. on p. 17).
- [Har97] HARASAKI, A. and K. KATO: ‘New Data on the Nonlinear Optical Constant, Phase-Matching, and Optical Damage of AgGaS<sub>2</sub>’. *Jpn. J. Appl. Phys.* (1997), vol. 36(2): pp. 700–703 (cit. on p. 115).
- [Har69] HARRIS, S. E.: ‘Tunable Optical Parametric Oscillator’. *Proc. IEEE*. Vol. 57. 1969: pp. 2096–2113 (cit. on p. 60).
- [Hau91] HAUS, H. A, U. KELLER, and W. H. KNOX: ‘A theory of coupled cavity modelocking with resonant nonlinearity’. *J. Opt. Soc. Am. B* (1991), vol. 8: pp. 1252–1258 (cit. on p. 16).
- [Hax08] HAXSEN, F., A. RUEHL, M. ENGELBRECHT, D. WANDT, U. MORGNER, and D. KRACHT: ‘Stretched-pulse operation of a thulium-doped fiber laser’. *Opt. Express* (2008), vol. 16(25): pp. 20471–20476 (cit. on p. 16).



- 
- [Hem15] HEMMER, M., D. SÁNCHEZ, M. JELÍNEK, V. SMIRNOV, H. JELINKOVA, V. KUBEČEK, and J. BIEGERT: ‘2- $\mu\text{m}$  wavelength, high-energy Ho:YLF chirped-pulse amplifier for mid-infrared OPCPA’. *Opt. Lett.* (2015), vol. 40(4): pp. 451–454 (cit. on pp. 6, 41).
- [Hen06] HENRIKSSON, M., M. TIHONEN, V. PASISKEVICIUS, and F. LAURELL: ‘ZnGeP<sub>2</sub> parametric oscillator pumped by a linewidth-narrowed parametric 2  $\mu\text{m}$  source’. *Opt. Lett.* (2006), vol. 31(12): pp. 1878–1880 (cit. on p. 66).
- [Hil14] HILDEBRAND, A., C. KIELECK, A. TYAZHEV, G. MARCHEV, G. STÖPPLER, M. EICHHORN, P. G. SCHUNEMANN, V. L. PANYUTIN, and V. PETROV: ‘Laser damage of the nonlinear crystals CdSiP<sub>2</sub> and ZnGeP<sub>2</sub> studied with nanosecond pulses at 1064 and 2090 nm’. *Opt. Engineering* (2014), vol. 53(12): p. 122511 (cit. on p. 68).
- [Hin18a] HINKELMANN, M., B. SCHULZ, D. WANDT, U. MORGNER, M. FREDE, J. NEUMANN, and D. KRACHT: ‘Millijoule-level, kilohertz-rate, CPA-free linear amplifier for 2  $\mu\text{m}$  ultrashort laser pulses’. *Opt. Lett.* (2018), vol. 43(23): pp. 5857–5860 (cit. on p. 49).
- [Hin18b] HINKELMANN, M., D. WANDT, U. MORGNER, J. NEUMANN, and D. KRACHT: ‘High repetition rate,  $\mu\text{J}$ -level, CPA-free ultrashort pulse multipass amplifier based on Ho:YLF’. *Opt. Express* (2018), vol. 26(14): pp. 18125–18130 (cit. on pp. 44, 76).
- [Hin17] HINKELMANN, M., D. WANDT, U. MORGNER, J. NEUMANN, and D. KRACHT: ‘Mode-locked Ho-doped amplifier in an all-fiber design operating at 2052 nm’. *Opt. Express* (2017), vol. 25(17): pp. 20522–20529 (cit. on pp. 15, 19, 25).
- [HIT19] HITRAN: *HITRAN database*. 2019. URL: <http://hitran.iao.ru/> (visited on 08/16/2019) (cit. on pp. 69, 70, 73).
- [Hof92] HOFER, M., M. H. OBER, F. HABERL, and M. E. FERMAN: ‘Characterization of Ultrashort Pulse Formation in Passively Mode-Locked Fiber Lasers’. *IEEE J. Quantum Electron.* (1992), vol. 28(3): pp. 720–728 (cit. on pp. 16, 17).
- [Hon14] HONG, K.-H., C.-J. LAI, J. P. SIQUEIRA, P. KROGEN, J. MOSES, C.-L. CHANG, G. J. STEIN, L. E. ZAPATA, and F. X. KÄRTNER: ‘Multi-mJ, kHz, 2.1  $\mu\text{m}$  optical parametric chirped-pulse amplifier and high-flux soft x-ray high-harmonic generation’. *Opt. Lett.* (2014), vol. 39(11): pp. 3145–3148 (cit. on p. 5).
- [Hum07] HUM, D. S. and M. M. FREJER: ‘Quasi-phasematching’. *C. R. Phys.* (2007), vol. 8(2): pp. 180–198 (cit. on p. 63).
- [Hur07] HURLBUT, W. C., Y.-S. LEE, K. L. VODOPYANOV, P. S. KUO, and M. M. FEJER: ‘Multiphoton absorption and nonlinear refraction of GaAs in the mid-infrared’. *Opt. Lett.* (2007), vol. 32(6): pp. 668–670 (cit. on p. 2).
- [Ild04] ILDAY, F. Ö., J. R. BUCKLEY, W. G. CLARK, and F. W. WISE: ‘Self-Similar Evolution of Parabolic Pulses in a Laser’. *Phys. Rev. Lett.* (2004), vol. 92: pp. 213902-1–213902-4 (cit. on p. 14).

- [Ild03] ILDAY, F. Ö., J. R. BUCKLEY, H. LIM, F. W. WISE, and W. G. CLARK: ‘Generation of 50-fs, 5-nJ pulses at 1.03  $\mu\text{m}$  from a wave-breaking-free fiber laser’. *Opt. Lett.* (2003), vol. 28(15): pp. 1365–1367 (cit. on p. 16).
- [Inn90] INNOCENZI, M. E., H. T. YURA, C. L. FINCHER, and R. A. FIELDS: ‘Thermal modeling of continuous-wave end-pumped solid-state lasers’. *Appl. Phys. Lett.* (1990), vol. 56(19): pp. 1831–1833 (cit. on p. 41).
- [Ipp94] IPPEN, E. P.: ‘Principles of passive mode locking’. *Appl. Phys. B* (1994), vol. 58(3): pp. 159–170 (cit. on p. 17).
- [Irm16] IRMER, G., C. RÖDER, C. HIMCINSCHI, and J. KORTUS: ‘Nonlinear optical coefficients of wurtzite-type  $\alpha$ -GaN determined by Raman spectroscopy’. *Phys. Rev. B* (2016), vol. 94: p. 195201 (cit. on p. 115).
- [ISO05] ISO11146:2005: ‘Lasers and laser-related equipment - Test methods for laser beam widths, divergence angles and beam propagation ratios’. (2005), vol. (cit. on p. 27).
- [Joo00] JOOS, K. M., J. H. SHEN, D. J. SHETLAR, and V. A. CASAGRANDE: ‘Optic Nerve Sheath Fenestration With a Novel Wavelength Produced by the Free Electron Laser (FEL)’. *Lasers Surgery and Med.* (2000), vol. 27: pp. 191–205 (cit. on p. 1).
- [Jun97] JUNG, I. D., F. X. KÄRTNER, N. MATUSCHEK, D. H. SUTTER, F. MORIER-GENOUD, Z. SHI, V. SCHEUER, M. TILSCH, T. TSCHUDI, and U. KELLER: ‘Semiconductor saturable absorber mirrors supporting sub-10-fs pulses’. *Appl. Phys. B* (1997), vol. 65: pp. 137–150 (cit. on p. 17).
- [Kad11] KADWANI, P., R. SIMS, J. CHIA, F. ALTAT, L. SHAH, and M. RICHARDSON: ‘Atmospheric Propagation Testing Using Broadband Thulium Fiber Systems’. *Advances in Optical Materials*. Optical Society of America, 2011: FWB3 (cit. on p. 2).
- [Kam16] KAMYNIN, V. A., S. A. FILATOVA, I. V. ZHLUKTOVA, and V. B. TSVETKOV: ‘Picosecond holmium fibre laser pumped at 1125 nm’. *Quantum Electron.* (2016), vol. 46(12): pp. 1082–1084 (cit. on p. 19).
- [Kan18] KANAI, T., U. ELU, D. SÁNCHEZ, K. ZAWILSKI, P. SCHUNEMANN, O. CHALUS, G. MATRAS, C. SIMON-BOISSON, and J. BIEGERT: ‘260-mJ Ho:YLF pump for a 7- $\mu\text{m}$  OPCPA’. *High-brightness Sources and Laser-driven Interactions Congress*. Optical Society of America, 2018: HT3A.8 (cit. on pp. 6, 7).
- [Kan17] KANAI, T., P. MALEVICH, S. S. KANGAPARAMBIL, K. ISHIDA, M. MIZUI, K. YAMANOUCHI, H. HOOGLAND, R. HOLZWARH, A. PUGZLYS, and A. BAL-TUSKA: ‘Parametric amplification of 100 fs mid-infrared pulses in ZnGeP<sub>2</sub> driven by a Ho:YAG chirped-pulse amplifier’. *Opt. Lett.* (2017), vol. 42(4): pp. 683–686 (cit. on p. 7).
- [Kär98] KÄRTNER, F. X., J. AUS DER AU, and U. KELLER: ‘Mode-Locking with Slow and Fast Saturable Absorbers - What’s the difference?’ *IEEE J. Sel. Topics Quantum Electron.* (1998), vol. 4(2): pp. 159–168 (cit. on pp. 19, 112).



- 
- [Kat02] KATO, K. and E. TAKAOKA: ‘Sellmeier and thermo-optic dispersion formulas for KTP’. *Appl. Optics* (2002), vol. 41(24): pp. 5040–5044 (cit. on p. 115).
- [Kat13] KATO, K., F. TANNO, and N. UMEMURA: ‘Sellmeier and thermo-optic dispersion formulas for GaSe’. *Appl. Optics* (2013), vol. 52(11): pp. 2325–2328 (cit. on p. 115).
- [Kel91] KELLER, U., G. H. HOOFT, W. H. KNOX, and J. E. CUNNINGHAM: ‘Femtosecond pulses from a continuously self-starting passively mode-locked Ti:sapphire laser’. *Opt. Lett.* (1991), vol. 16: pp. 1022–1024 (cit. on p. 16).
- [Kel90] KELLER, U., W. H. KNOX, and H. ROSKOS: ‘Coupled-cavity resonant passive modelocked (RPM) Ti:Sapphire laser’. *Opt. Lett.* (1990), vol. 15: pp. 1377–1379 (cit. on p. 16).
- [Kel96] KELLER, U., K. J. WEINGARTEN, F. X. KÄRTNER, D. KOPF, B. BRAUN, I. D. JUNG, R. FLUCK, and C. HONNINGER: ‘Semiconductor saturable absorber mirrors (SESAM’s) for femtosecond to nanosecond pulse generation in solid-state lasers’. *IEEE J. Sel. Top. Quantum Electron.* (1996), vol. 2(3): pp. 435–453 (cit. on p. 17).
- [Kel92] KELLY, S. M. J.: ‘Characteristic sideband instability of periodically amplified average soliton’. *Electronic Lett.* (1992), vol. 28(8): pp. 806–807 (cit. on p. 15).
- [Kib05] KIBLER, B., J.M. DUDLEY, and S. COEN: ‘Supercontinuum generation and nonlinear pulse propagation in photonic crystal fiber: influence of the frequency-dependent effective mode area’. *Appl. Phys. B* (2005), vol. 81(2–3): pp. 337–342 (cit. on p. 111).
- [Kle68] KLEINMAN, D. A.: ‘Theory of Optical Parametric Noise’. *Phys. Rev.* (1968), vol. 174(3): pp. 1027–1041 (cit. on p. 59).
- [Kno88] KNOX, W. H., D. S. CHEMLA, G. LIVESCU, J. E. CUNNINGHAM, and J. E. HENRY: ‘Femtosecond Carrier Thermalization in Dense Fermi Seas’. *Phys. Rev. Lett.* (1988), vol. 61(11): pp. 1290–1293 (cit. on p. 17).
- [Koe06] KOECHNER, W.: *Solid-state Laser Engineering*. Ed. by RHODES, W. T. 6th ed. Springer-Verlag, 2006 (cit. on pp. 32, 33).
- [Kol12] KOLE, M. R., R. K. REDDY, M. V. SCHULMERICH, M. K. GELBER, and R. BHARGAVA: ‘Discrete Frequency Infrared Microspectroscopy and Imaging with a Tunable Quantum Cascade Laser’. *Analytical Chemistry* (2012), vol. 84: pp. 10366–10372 (cit. on p. 6).
- [Koo12] KOOPMANN, P.: ‘Thulium- and Holmium-Doped Sesquioxides for 2  $\mu\text{m}$  Lasers’. PhD thesis. University of Hamburg, 2012 (cit. on pp. 34, 35).
- [Kop00] KOPLOW, J. P., D. A. V. KLINER, and L. GOLDBERG: ‘Single-mode operation of a coiled multimode fiber amplifier’. *Opt. Lett.* (2000), vol. 25(7): pp. 442–444 (cit. on p. 28).

- [Kro16a] KROETZ, P., A. RUEHL, K. MURARI, H. CANKAYA, F. X. KÄRTNER, I. HARTL, and R. J. DWAYNE MILLER: ‘Numerical study of spectral shaping in high energy Ho:YLF amplifiers’. *Opt. Express* (2016), vol. 24(9): pp. 9905–9921 (cit. on pp. 30–32).
- [Kro16b] KROGEN, P., H. LIANG, K. ZAWILSI, P. SCHUNEMANN, T. LANG, U. MORGNER, J. MOSES, F. X. KÄRTNER, and K.-H. HONG: ‘Octave-spanning 1.5-optical-cycle 6.5- $\mu\text{m}$  OPA pumped by 2.1- $\mu\text{m}$  OPCPA’. *Conference on Lasers and Electro-Optics*. Optical Society of America, 2016: STu3I.4 (cit. on p. 7).
- [Kro62] KROLL, N. M.: ‘Parametric amplification in spatially extended media and application to the design of tuneable oscillators at optical frequencies’. *Phys. Rev.* (1962), vol. 127: pp. 1207–1211 (cit. on p. 59).
- [Kub14] KUBAT, I., C. ROSENBERG PETERSEN, U. VISBECH MOLLER, A. SEDDON, T. BENSON, L. BRILLAND, D. MÉCHIN, P. M. MOSELMUND, and O. BANG: ‘Thulium pumped mid-infrared 0.9-9 $\mu\text{m}$  supercontinuum generation in concatenated fluoride and chalcogenide glass fibers’. *Opt. Express* (2014), vol. 22(4): pp. 3959–3967 (cit. on p. 66).
- [Kur10] KURKOV, A. S., V. V. DVOYRIN, and A. V. MARAKULIN: ‘All-fiber 10 W holmium lasers pumped at  $\lambda = 1.15 \mu\text{m}$ ’. *Opt. Lett.* (2010), vol. 35(4): pp. 490–492 (cit. on p. 17).
- [Kuy11] KUYKEN, B., X. LIU, R. M. OSGOOD JR., R. BAETS, G. ROELKENS, and W. M. J. GREEN: ‘Mid-infrared to telecom-band supercontinuum generation in highly nonlinear silicon-on-insulator wire waveguides’. *Opt. Express* (2011), vol. 19(21): pp. 20172–20181 (cit. on p. 66).
- [Kwi09] KWIATKOWSKI, J., J. K. JABCZYNSKI, L. GORAJEK, W. ZENDZIAN, H. JELÍNKO-VÁ, J. ŠULC, M. NĚMEC, and P. KORANDA: ‘Resonantly pumped tunable Ho:YAG laser’. *Laser Phys. Lett.* (2009), vol. 6(7): pp. 531–534 (cit. on p. 34).
- [Lag05] LAGATSKY, A. A., A. R. SARMANI, C. T. A. BROWN, W. SIBBETT, V. E. KISEL, A. G. SELIVANOV, I. A. DENISOV, A. E. TROSHIN, K. V. YUMASHEV, N. V. KULESHOV, V. N. MATROSOV, T. A. MATROSOVA, and M. I. KUPCHENKO: ‘Yb<sup>3+</sup>-doped YVO<sub>4</sub> crystal for efficient Kerr-lens mode locking in solid-state lasers’. *Opt. Lett.* (2005), vol. 30(23): pp. 3234–3236 (cit. on p. 35).
- [Lee13] LEE, K. F., J. JIANG, C. MOHR, J. BETHGE, M. E. FERMAN, N. LEINDECKER, K. L. VODOPYANOV, P. G. SCHUNEMANN, and I. HARTL: ‘Carrier envelope offset frequency of a doubly resonant, nondegenerate, mid-infrared GaAs optical parametric oscillator’. *Opt. Lett.* (2013), vol. 38(8): pp. 1191–1193 (cit. on p. 66).
- [Lei12] LEINDECKER, N., A. MARANDI, R. L. BYER, K. L. VODOPYANOV, J. JIANG, I. HARTL, M. FERMAN, and P. G. SCHUNEMANN: ‘Octave-spanning ultrafast OPO with 2.6-6.1 $\mu\text{m}$  instantaneous bandwidth pumped by femtosecond Tm-fiber laser’. *Opt. Express* (2012), vol. 20(7): pp. 7046–7053 (cit. on p. 66).

- 
- [Len98] LENZNER, M., J. KRÜGER, S. SARTANIA, Z. CHENG, C. SPIELMANN, G. MOUROU, W. KAUTEK, and F. KRAUSZ: ‘Femtosecond Optical Breakdown in Dielectrics’. *Phys. Rev. Lett.* (1998), vol. 80(18): pp. 4076–4079 (cit. on p. 37).
- [Li11] LI, G., B. Q. YAO, P. B. MENG, X. M. DUAN, Y. L. JU, and Y. Z. WANG: ‘Diode-pumped efficient laser operation and spectroscopy of Tm,Ho:YVO<sub>4</sub>’. *Opt. Mater.* (2011), vol. 33(6): pp. 937–941 (cit. on p. 35).
- [Li16] LI, P., A. RUEHL, C. BRANSLEY, and I. HARTL: ‘Low Noise, tunable Ho:fiber Soliton Oscillator for Ho:YLF Amplifier Seeding’. *Laser Phys. Lett.* (2016), vol. 13(6): p. 065104 (cit. on p. 19).
- [Li14] LI, P., A. RUEHL, U. GROSSE-WORTMANN, and I. HARTL: ‘Sub-100 fs passively mode-locked holmium-doped fiber oscillator operating at 2.06  $\mu\text{m}$ ’. *Opt. Lett.* (2014), vol. 39(24): pp. 6859–6862 (cit. on pp. 16, 19, 22, 77).
- [Lia15] LIANG, H., P. KROGEN, R. GRYNKO, O. NOVAK, C.-L. CHANG, G. J. STEIN, D. WEERAWARNE, B. SHIM, F. X. KÄRTNER, and K.-H. HONG: ‘Three-octave-spanning supercontinuum generation and sub-two-cycle self-compression of mid-infrared filaments in dielectrics’. *Opt. Lett.* (2015), vol. 40(6): pp. 1069–1072 (cit. on p. 66).
- [Liu19] LIU, Y., P. KROGEN, K.-H. HONG, Q. CAO, P. KEATHLEY, and F. X. KÄRTNER: ‘Fiber-amplifier-pumped, 1-MHz, 1- $\mu\text{J}$ , 2.1- $\mu\text{m}$ , femtosecond OPA with chirped-pulse DFG front-end’. *Opt. Express* (2019), vol. 27(6): pp. 9144–9154 (cit. on p. 5).
- [Mai60] MAIMAN, T. H.: ‘Stimulated Optical Radiation in Ruby’. *Nature* (1960), vol. 187(4736): pp. 493–494 (cit. on p. 1).
- [Mak62] MAKER, P. D., R. W. TERHUNE, M. NISSENOFF, and C. M. SAVAGE: ‘Effects of dispersion and focusing on the production of optical harmonics’. *Phys. Rev. Lett.* (1962), vol. 8(1): pp. 21–22 (cit. on p. 61).
- [Mak64] MAKER, P. D., R. W. TERHUNE, and C. M. SAVAGE: ‘Intensity-dependent changes in the refractive index of liquids’. *Phys. Rev. Lett.* (1964), vol. 12(18): pp. 507–509 (cit. on p. 17).
- [Mal13] MALEVICH, P., G. ANDRIUKAITIS, T. FLÖRY, A. J. VERHOEF, A. FERNÁNDEZ, S. ALIŠAUSKAS, A. PUGŽLYS, A. BALTUŠKA, L. H. TAN, C. F. CHUA, and P. B. PHUA: ‘High energy and average power femtosecond laser for driving mid-infrared optical parametric amplifiers’. *Opt. Lett.* (2013), vol. 38(15): pp. 2746–2749 (cit. on p. 5).
- [Mam98] MAMYSHEV, P. V.: ‘All-optical data regeneration based on self-phase modulation effect’. *24th European Conference on Optical Communication*. IEEE, 1998: pp. 475–476 (cit. on p. 46).
- [Man16] MANZONI, C. and G. CERULLO: ‘Design criteria for ultrafast optical parametric amplifiers’. *J. Opt.* (2016), vol. 18(10): p. 103501 (cit. on pp. 57, 63).

- [Mar77] MARCUSE, D.: ‘Loss Analysis of Single-Mode Fiber Splices’. *Bell Syst. Tech. J.* (1977), vol. 56(5): pp. 703–718 (cit. on p. 19).
- [Mat93] MATSAS, V. J., D. J. RICHARDSON, T. P. NEWSON, and D. N. PAYNE: ‘Characterization of a self-starting, passively mode-locking fiber ring laser that exploits nonlinear polarization evolution’. *Opt. Lett.* (1993), vol. 18(5): pp. 358–360 (cit. on p. 17).
- [Mil77] MILAM, D., M. J. WEBER, and A. J. GLASS: ‘Nonlinear refractive index of fluoride crystals’. *Appl. Phys. Lett.* (1977), vol. 31(12): p. 822 (cit. on p. 35).
- [Mil64] MILLER, R. C.: ‘Optical Second Harmonic Generation in Piezoelectric Crystals’. *Appl. Phys. Lett.* (1964), vol. 5(1): pp. 17–19 (cit. on pp. 65, 114).
- [Min16] MINGAREEV, I., N. GEHLICH, T. BONHOFF, A. ABDULFATTAH, A. M. SINCORE, P. KADWANI, L. SHAH, and M. RICHARDSON: ‘Principles and applications of trans-wafer processing using a 2- $\mu\text{m}$  thulium fiber laser’. *Int. J. Adv. Manuf. Technol.* (2016), vol. 84: pp. 2567–2578 (cit. on p. 2).
- [Min12] MINGAREEV, I., F. WEIRAUCH, A. OLOWINSKY, L. SHAH, P. KADWANI, and M. RICHARDSON: ‘Welding of polymers using a 2  $\mu\text{m}$  thulium fiber laser’. *Optics & Laser Technology* (2012), vol. 44: pp. 2095–2099 (cit. on p. 2).
- [Mir18] MIROV, S. B., I. S. MOSKALEV, S. VASILYEV, V. SMOLSKI, V. V. FEDEROV, D. MARTYSHKIN, J. PEPPERS, M. MIROV, A. DERGACHEV, and V. GAPONTSEV: ‘Frontiers of Mid-IR Lasers Based on Transition Metal Doped Chalcogenides’. *IEEE J. Sel. Top. Quantum. Electron.* (2018), vol. 24(5): p. 1601829 (cit. on p. 6).
- [Mir15] MIROV, SERGEY B., VLADIMIR V. FEDOROV, DMITRY MARTYSHKIN, IGOR S. MOSKALEV, MIKE MIROV, and SERGEY VASILYEV: ‘Progress in Mid-IR Lasers Based on Cr and Fe-Doped II-VI Chalcogenides’. *IEEE J. Sel. Top. Quantum Electron.* (2015), vol. 21(1): p. 1601719 (cit. on p. 33).
- [Mit05] MITSCHKE, F.: *Glasfasern*. Elsevier GmbH, 2005 (cit. on p. 10).
- [Moc65] MOCKER, H. W. and R. J. COLLINS: ‘Mode competition and self-locking effects in a Q-switched ruby laser’. *Appl. Phys. Lett.* (1965), vol. 7: pp. 270–273 (cit. on p. 16).
- [Mol80] MOLLENAUER, L. F., R. H. STOLEN, and J. P. GORDON: ‘Experimental Observation of Picosecond Pulse Narrowing and Solitons in Optical Fibers’. *Phys. Rev. Lett.* (13 1980), vol. 45: pp. 1095–1098 (cit. on p. 14).
- [Nai14] NAITHANI, S., C. DUTERTE, M. LEVICHKOVA, A. GRISARD, D. SCHAUBROECK, E. LALLIER, Y. HERNANDEZ, K. WALZER, and G. VAN STEENBERGE: ‘Mid-infrared resonant ablation for selective patterning of thin organic films’. *Proc. SPIE 9135, Laser Sources and Applications II*. 2014: 91350K-01–91350K-12 (cit. on p. 2).

- 
- [Nai13] NAITHANI, S., A. GRISARD, D. SCHAUBROECK, E. LALLIER, and G. VAN STEENBERGE: ‘Mid-infrared resonant ablation of PMMA’. *Proceedings of 6th International Congress on Laser Advanced Materials Processing*. Niigata, Japan, 2013: pp. 1–5 (cit. on p. 2).
- [Nel97] NELSON, L. E., D. J. JONES, K. TAMURA, H. A. HAUS, and E. P. IPPEN: ‘Ultrashort-pulse fiber ring lasers’. *Appl. Phys. B* (1997), vol. 65(2): pp. 277–294 (cit. on p. 16).
- [Nik05] NIKOGOSYAN, D. N.: *Nonlinear Optical Crystals: A Complete Survey*. Springer, 2005 (cit. on p. 115).
- [Nis01] NISHIZAWA, N. and T. GOTO: ‘Widely Wavelength-Tunable Ultrashort Pulse Generation Using Polarization Maintaining Optical Fibers’. *IEEE J. Sel. Top. Quantum. Electron.* (2001), vol. 7(4): pp. 518–524 (cit. on p. 5).
- [Nuf19] NUFERN: *EyeSafe 40 Micron Core Holmium-Doped LMA Double Clad Fiber*. 2019. URL: [https://www.nufern.com/pam/optical\\_fibers/spec/id/1076/?2351](https://www.nufern.com/pam/optical_fibers/spec/id/1076/?2351) (cit. on p. 28).
- [Obe93] OBER, M., M. HOFER, U. KELLER, and T. CHIU: ‘Self-starting diode-pumped femtosecond Nd fiber laser’. *Opt. Lett.* (1993), vol. 18: pp. 1532–1534 (cit. on p. 19).
- [Pac04] PACK, M. V., D. J. ARMSTRONG, and A. V. SMITH: ‘Measurement of the  $\chi^{(2)}$  tensors of  $\text{KTiOPO}_4$ ,  $\text{KTiOAsO}_4$ ,  $\text{RbTiOPO}_4$ , and  $\text{RbTiOAsO}_4$  crystals’. *Appl. Optics* (2004), vol. 43(16): pp. 3319–3323 (cit. on p. 115).
- [Paw17] PAWLISZEWSKA, M., Y. GE, Z. LI, H. ZHANG, and J. SOTOR: ‘Fundamental and harmonic mode-locking at 2.1  $\mu\text{m}$  with black phosphorus saturable absorber’. *Opt. Express* (2017), vol. 25(13): pp. 16916–16921 (cit. on pp. 15, 19, 22).
- [Paw18] PAWLISZEWSKA, M., T. MARTYNKIEN, A. PRZEWŁOKA, and J. SOTOR: ‘Dispersion-managed Ho-doped fiber laser mode-locked with a graphene saturable absorber’. *Opt. Lett.* (2018), vol. 43(1): pp. 38–41 (cit. on pp. 16, 19, 20).
- [Pay92] PAYNE, S. A., L. L. CHASE, L. K. SMITH, W. L. KWAY, and W. F. KRUPKE: ‘Infrared cross-section measurements for crystals doped with  $\text{Er}^{3+}$ ,  $\text{Tm}^{3+}$ , and  $\text{Ho}^{3+}$ ’. *IEEE J. Quantum Electron.* (1992), vol. 28(11): pp. 2619–2630 (cit. on pp. 35, 38, 39).
- [Pet95] PETERSON, R. D., K. L. SCHEPLER, J. L. BROWN, and P. G. SCHUNEMANN: ‘Damage properties of  $\text{ZnGeP}_2$  at 2  $\mu\text{m}$ ’. *J. Opt. Soc. Am. B* (1995), vol. 12(11): pp. 2142–2146 (cit. on p. 68).
- [Pet11] PETRICH, W.: ‘Mid-Infrared and Raman Spectroscopy for Medical Applications’. *Appl. Spectroscopy Rev.* (2011), vol. 36(1-2): pp. 181–237 (cit. on p. 1).
- [Pet15] PETROV, V.: ‘Frequency down-conversion of solid-state laser sources to the mid-infrared spectral range using non-oxide nonlinear crystals’. *Prog. Quantum Electron.* (2015), vol. 42: pp. 1–106 (cit. on pp. 7, 57).

- [Pet09] PETROV, V., F. NOACK, I. TUNCHEV, P. SCHUNEMANN, and K. ZAWILSKI: ‘The nonlinear coefficient  $d_{36}$  of  $\text{CdSiP}_2$ ’. *Proc. SPIE 7197, Nonlinear Frequency Generation and Conversion: Materials, Devices, and Applications VIII*. 2009 (cit. on p. 115).
- [Pet99] PETROV, V., F. ROTERMUND, F. NOACK, and P. SCHUNEMANN: ‘Femtosecond parametric generation in  $\text{ZnGeP}_3$ ’. *Opt. Lett.* (1999), vol. 24(6): pp. 414–416 (cit. on pp. 65, 66).
- [Phi11] PHILLIPS, C. R., C. LANGROCK, J. S. PELC, M. M. FEJER, J. JIANG, M. E. FERMAN, and I. HARTL: ‘Supercontinuum generation in quasi-phase-matched  $\text{LiNbO}_3$  waveguide pumped by a Tm-doped fiber laser system’. *Opt. Lett.* (2011), vol. 36(19): pp. 3912–3914 (cit. on p. 66).
- [Pho19] PHOTONICS, IPG: *TLR-200 Thulium CW Fiber Laser*. IPG Photonics Corporation. 2019. URL: <https://www.ipgphotonics.com/en/104/FileAttachment/TLM-200+Datasheet.pdf> (visited on 08/20/2019) (cit. on pp. 17, 81).
- [Pop12] POPMINTCHEV, T. et al.: ‘Bright Coherent Ultrahigh Harmonics in the keV X-ray Regime from Mid-Infrared Femtosecond Lasers’. *Science* (2012), vol. 336: pp. 1287–1291 (cit. on p. 2).
- [Rau15] RAUTER, P. and F. CAPASSO: ‘Multi-wavelength quantum cascade laser arrays’. *Laser Photon. Rev.* (2015), vol. 9(5): pp. 452–477 (cit. on p. 6).
- [Ray05] RAYBAUT, P., F. BALEMBOIS, F. DRUON, and P. GEORGES: ‘Numerical and experimental study of gain narrowing in Ytterbium-based regenerative amplifiers’. *IEEE J. Quantum Electron.* (2005), vol. 41(3): pp. 415–425 (cit. on p. 30).
- [Ric02] RICHMOND, G. L.: ‘Molecular Bonding and Interactions at Aqueous Surfaces as Probed by Vibrational Sum Frequency Spectroscopy’. *Chem. Rev.* (2002), vol. 102: pp. 2693–2724 (cit. on p. 2).
- [Rig18] RIGLER, M., T. TROHA, W. GUO, R. KIRSTE, I. BRYAN, R. COLLAZO, Z. SITAR, and M. ZGONIK: ‘Second-Harmonic Generation of Blue Light in GaN Waveguides’. *Appl. Sci.* (2018), vol. 8: p. 1218 (cit. on p. 115).
- [Rob92] ROBERTS, D. A.: ‘Simplified Characterization of Uniaxial and Biaxial Nonlinear Optical Crystals: A Plea for Standardization of Nomenclature and Conventions’. *IEEE J. Quantum. Electron.* (1992), vol. 28(10): pp. 2057–2074 (cit. on p. 115).
- [Rot01] ROTERMUND, F., V. PETROV, F. NOACK, and P. SCHUNEMANN: ‘Characterization of  $\text{ZnGeP}_2$  for Parametric Generation with Near-Infrared Femtosecond Pumping’. *Fiber Integr. Optics* (2001), vol. 20: pp. 139–150 (cit. on p. 66).
- [Rot89] ROTHENBERG, J. E. and D. GRISCHKOWSKY: ‘Observation of the Formation of an Optical Intensity Shock and Wave Breaking in the Nonlinear Propagation of Pulses in Optical Fibers’. *Phys. Rev. Lett.* (1989), vol. 62(5): pp. 531–534 (cit. on p. 12).



- 
- [San16] SANCHEZ, D., M. HEMMER, M. BAUDISCH, S. L. COUSIN, K. ZAWILSKI, P. SCHUNEMANN, O. CHALUS, C. SIMON-BOISSON, and J. BIEGERT: ‘7  $\mu\text{m}$ , ultrafast, sub-millijoule-level mid-infrared optical parametric chirped pulse amplifier pumped at 2  $\mu\text{m}$ ’. *Optica* (2016), vol. 3(2): pp. 147–150 (cit. on pp. 7, 68).
- [Sán14] SÁNCHEZ, D., M. HEMMER, M. BAUDISCH, K. ZAWILSKI, P. SCHUNEMANN, H. HOOGLAND, R. HOLZWARTH, and J. BIEGERT: ‘Broadband mid-IR frequency comb with CdSiP<sub>2</sub> and AgGaS<sub>2</sub> from an Er,Tm:Ho fiber laser’. *Opt. Lett.* (2014), vol. 39(24): pp. 6883–6886 (cit. on p. 66).
- [Sch10] SCHOLLE, K., S. LAMRINI, P. KOOPMANN, and P. FUHRBERG: ‘Frontiers in Guided Wave Optics and Optoelectronics’. Ed. by PAL, B. InTech, 2010. Chap. 2  $\mu\text{m}$  Laser Sources and Their Possible Applications: pp. 471–500 (cit. on p. 2).
- [Sch19] SCHREIBER, T.: *Fiberdesk*. 2019. URL: <http://www.fiberdesk.com/> (visited on 06/14/2019) (cit. on pp. 20, 111).
- [Sch05] SCHUNEMANN, P. G., S. D. SETZLER, L. MOHNKERN, T. M. POLLAK, D. F. BLISS, D. WEYBURN, and K. O’HEARN: ‘2.05- $\mu\text{m}$ -laser-pumped orientation-patterned gallium arsenide (OPGaAs) OPO’. *CLEO: 2005*. Optical Society of America, 2005: CThQ4 (cit. on p. 115).
- [Sch08] SCHUNEMANN, P. G., K. ZAWILSKI, T. M. POLLAK, D. E. ZELMON, N. C. FERNELIUS, and F. KENNETH HOPKINS: ‘New nonlinear optical crystal for mid-IR OPOs: CdSiP<sub>2</sub>’. *ASSP: 2008*. Optical Society of America, 2008: MG6 (cit. on p. 115).
- [Sch16] SCHUNEMANN, P. G., K. T. ZAWILSKI, L. A. POMERANZ, D. J. CREEDEN, and P. A. BUDNI: ‘Advances in nonlinear optical crystals for mid-infrared coherent sources’. *J. Opt. Soc. Am. B* (2016), vol. 33(11): pp. D36–D43 (cit. on pp. 2, 7, 64, 65, 115).
- [Sha01] SHAN, B. and Z. H. CHANG: ‘Dramatic extension of the high-order harmonic cutoff by using a long-wavelength driving field’. *Phys. Rev. A* (2001), vol. 65: p. 011804 (cit. on p. 2).
- [Sha69] SHAND, W. A.: ‘Single crystal growth and some properties of LiYF<sub>4</sub>’. *J. Crystal Growth* (1969), vol. 5: pp. 143–146 (cit. on p. 35).
- [Sho97] SHOJI, I., T. KONDO, A. KITAMOTO, M. SHIRANE, and R. ITO: ‘Absolute scale of second-order nonlinear-optical coefficients’. *J. Opt. Soc. Am. B* (1997), vol. 14(9): pp. 2268–2294 (cit. on p. 115).
- [Sie86] SIEGMAN, A. E.: *Lasers*. University Science Books, 1986 (cit. on p. 32).
- [Sim13] SIMAKOV, N., A. HEMMING, W. A. CLARKSON, J. HAUB, and A. CARTER: ‘A cladding-pumped, tunable holmium doped fiber laser’. *Opt. Express* (2013), vol. 21(23): pp. 28415–28422 (cit. on pp. 17, 18).

- [Ska03] SKAULI, T., P. S. KUO, K. L. VODOPYANOV, T. J. PINGUET, O. LEVI, L. A. EYRES, J. S. HARRIS, M. M. FEJER, B. GERARD, L. BECOUARN, and E. LALLIER: ‘Improved dispersion relations for GaAs and applications to nonlinear optics’. *J. Appl. Phys.* (2003), vol. 94(10): pp. 6447–6455 (cit. on p. 115).
- [Ska02] SKAULI, T., K. L. VODOPYANOV, T. J. PINGUET, A. SCHOBER, O. LEVI, L. A. EYRES, M. M. FEJER, J. S. HARRIS, B. GERARD, L. BECOUARN, E. LALLIER, and G. ARISHOLM: ‘Measurement of the nonlinear coefficient of orientation-patterned GaAs and demonstration of highly efficient second-harmonic generation’. *Opt. Lett.* (2002), vol. 27(8): pp. 628–630 (cit. on pp. 63, 115).
- [Smi70] SMITH, P. W.: ‘Mode-locking of lasers’. *Proc. of the IEEE* (1970), vol. 58(9): pp. 1342–1357 (cit. on p. 16).
- [Sny83] SNYDER, A. W. and J. D. LOVE: *Optical Waveguide Theory*. Kluwer Academic, 1983 (cit. on p. 23).
- [Sob18] SOBON, G., T. MARTYNKIEN, D. TOMASZEWSKA, K. TARNOWSKI, P. MERGO, and J. SOTOR: ‘All-in-fiber amplification and compression of coherent frequency-shifted solitons tunable in the 1800-2000 nm range’. *Photon. Research* (2018), vol. 6(5): pp. 368–372 (cit. on p. 5).
- [Sor18] SOROKIN, E., A. MARANDI, P. G. SCHUNEMANN, M. M. FEJER, R. L. BYER, and I. T. SOROKINA: ‘Efficient half-harmonic generation of three-optical-cycle mid-IR frequency comb around 4  $\mu\text{m}$  using OP-GaP’. *Opt. Express* (2018), vol. 26(8): pp. 9963–9971 (cit. on p. 115).
- [Sor05] SOROKIN, E., S. NAUMOV, and I. T. SOROKINA: ‘Ultrabroadband Infrared Solid-State Lasers’. *IEEE J. Sel. Top. Quantum. Electron.* (2005), vol. 11(3): pp. 690–712 (cit. on p. 6).
- [Sor10] SOROKIN, E., I. T. SOROKINA, M. S. MIROV, V. V. FEDOROV, I. S. MOSKALEV, and S. B. MIROV: ‘Ultrabroad continuous-wave tuning of ceramic Cr:ZnSe and Cr:ZnS lasers’. *Advanced Solid State Lasers*. Optical Society of America, 2010: AMC2 (cit. on p. 33).
- [Sor02] SOROKINA, I. T., E. SOROKIN, S. MIROV, V. FEDEROV, V. BADIKOV, V. PANYUTIN, and K. I. SCHAFFERS: ‘Broadly tunable compact continuous-wave Cr<sup>2+</sup>:ZnS laser’. *Opt. Lett.* (2002), vol. 27(12): pp. 1040–1042 (cit. on p. 33).
- [Sot16] SOTOR, J., M. PAWLISZEWSKA, G. SOBON, P. KACZMAREK, A. PRZEWOŁKA, I. PASTERNAK, J. CAJZL, P. PETERKA, P. HONZÁTKO, I. KAŠÍK, W. STRUPINSKI, and K. ABRAMSKI: ‘All-fiber Ho-doped mode-locked oscillator based on a graphene saturable absorber’. *Opt. Lett.* (2016), vol. 41(11): pp. 2592–2595 (cit. on pp. 15, 19, 22).
- [Str13] STRAUSS, H. J., D. PREUSSLER, M. J. D. ESSER, W. KOEN, G. JACOBS, O. J. P. COLLETT, and C. BOLLIG: ‘330 mJ single-frequency Ho:YLF slab amplifier’. *Opt. Lett.* (2013), vol. 38(7): pp. 1022–1024 (cit. on p. 36).



- 
- [Str85] STRICKLAND, D. and G. MOUROU: ‘Compression of amplified chirped optical pulses’. *Opt. Commun.* (1985), vol. 55(6): pp. 447–449 (cit. on p. 29).
- [Stu95] STUART, B. C., M. D. FEIT, A. M. RUBENCHIK, B. W. SHORE, and M. D. PERRY: ‘Laser-Induced Damage in Dielectrics with Nanosecond to Subpicosecond Pulses’. *Phys. Rev. Lett.* (1995), vol. 74(12): pp. 2248–2251 (cit. on p. 37).
- [Stu14] STUTZKI, F., F. JANSEN, H. J. OTTO, C. JAUREGUI, J. LIMPERT, and A. TÜNNERMANN: ‘Designing advanced very-large-mode-area fibers for power scaling of fiber-laser systems’. *Optica* (2014), vol. 1(4): pp. 233–242 (cit. on p. 23).
- [Tak99] TAKAOKA, E. and K. KATO: ‘Thermo-optics dispersion formula for AgGaS<sub>2</sub>’. *Appl. Optics* (1999), vol. 38(21): pp. 4577–4580 (cit. on p. 115).
- [Tam92] TAMURA, K., H. A. HAUS, and E. P. IPPEN: ‘Self-starting additive pulse mode-locked erbium fibre ring laser’. *Electron. Lett.* (1992), vol. 28(24): pp. 2226–2228 (cit. on p. 17).
- [Tam93] TAMURA, K., E. P. IPPEN, H. A. HAUS, and L. E. NELSON: ‘77-fs pulse generation from a stretched-pulse mode-locked all-fiber ring laser’. *Opt. Lett.* (1993), vol. 18(13): pp. 1080–1082 (cit. on p. 16).
- [Tie99] TIEN, A.-C., S. BACKUS, H. KAPTEYN, M. MURNANE, and G. MOUROU: ‘Short-Pulse Laser Damage in Transparent Materials as a Function of Pulse Duration’. *Phys. Rev. Lett.* (1999), vol. 82(19): pp. 3883–3886 (cit. on p. 37).
- [Tit03] TITTEL, F. K., D. RICHER, and A. FRIED: ‘Mid-Infrared Laser Applications in Spectroscopy’. *Solid-State Mid-Infrared Laser Sources* (2003), vol. 89: pp. 445–516 (cit. on p. 2).
- [Toc12] TOCHITSKY, S. YA., J. J. PIGEON, D. J. HABERBERGER, C. GONG, and C. JOSHI: ‘Amplification of multi-gigawatt 3 ps pulses in an atmospheric CO<sub>2</sub> laser using ac Stark effect’. *Opt. Express* (2012), vol. 20(13): pp. 13762–13768 (cit. on p. 6).
- [Tol16] TOLSTIK, N., E. SOROKIN, I. BUGAR, and I. T. SOROKINA: ‘Compact Diode-Pumped Dispersion-managed SESAM-mode-locked Ho: fiber Laser’. *High-Brightness Sources and Laser-Driven Interactions*. Optical Society of America, 2016: p. MM6C.4 (cit. on pp. 16, 19).
- [Var96] VAREL, H., D. ASHKENASI, A. ROSENFELD, R. HERRMANN, F. NOACK, and E. E. B. CAMPBELL: ‘Laser-induced damage in SiO<sub>2</sub> and CaF<sub>2</sub> with picosecond and femtosecond laser pulses’. *Appl. Phys. A* (1996), vol. 62: pp. 293–294 (cit. on p. 37).
- [Vas19] VASILYEV, S., I. MOSKALEV, V. SMOLSKI, J. PEPPERS, M. MIROV, V. FEDEROV, D. MARTYSHKIN, S. MIROV, and V. GAPONTSEV: ‘Octave-spanning Cr:ZnS femtosecond laser with intrinsic nonlinear interferometry’. *Optica* (2019), vol. 6(2): pp. 126–127 (cit. on p. 6).

- [Vod99] VODOPYANOV, K. L.: ‘Mid-infrared optical parametric generator with extra-wide (3-19- $\mu\text{m}$ ) tunability: applications for spectroscopy of two-dimensional electrons in quantum wells’. *J. Opt. Soc. Am. B* (1999), vol. 16(9): pp. 1579–1586 (cit. on p. 65).
- [Vod93] VODOPYANOV, K. L.: ‘Parametric generation of tunable infrared radiation in  $\text{ZnGeP}_2$  and  $\text{GaSe}$  pumped at 3  $\mu\text{m}$ ’. *J. Opt. Soc. Am. B* (1993), vol. 10(9): pp. 1723–1729 (cit. on pp. 68, 76, 78).
- [Wal98] WALSH, B. M., N. P. BARNES, and B. DI BARTOLO: ‘Branching ratios, cross sections, and radiative lifetimes of rare earth ions in solids: Application to  $\text{Tm}^{3+}$  and  $\text{Ho}^{3+}$  ions in  $\text{LiYF}_4$ ’. *J. Appl. Phys.* (1998), vol. 83(5): pp. 2772–2787 (cit. on pp. 2, 33–36, 38, 39).
- [Wan16] WANDEL, S., M.-W. LIN, Y. YIN, G. XU, and I. JOVANOVIĆ: ‘Parametric generation and characterization of femtosecond mid-infrared pulses in  $\text{ZnGeP}_2$ ’. *Opt. Express* (2016), vol. 24(5): pp. 5287–5299 (cit. on pp. 66, 71).
- [Wan14] WANDEL, S., G. XU, and I. JOVANOVIĆ: ‘Development of a high-peak-power 5- $\mu\text{m}$  parametric source for dielectric laser acceleration’. *Proceedings of International Particle Accelerator Conference (IPAC)*. 2014: TUPME045-1460–1462 (cit. on p. 7).
- [Wan17] WANG, Y., T. T. FERNANDEZ, N. COLUCCCELLI, A. GAMBETTA, P. LAPORTA, and G. GALZERANO: ‘47-fs Kerr-lens mode-locked  $\text{Cr}:\text{ZnSe}$  laser with high spectral purity’. *Opt. Express* (2017), vol. 25(21): pp. 25193–25200 (cit. on p. 6).
- [Web03] WEBER, M. J.: *Handbook of Optical Materials*. CRC Press LLC, Boca Raton, 2003 (cit. on pp. 35, 115).
- [Wie16] WIENKE, A.: ‘Regenerative amplification of ultrashort laser pulses with thulium- and holmium-doped materials’. PhD thesis. Leibniz Universität Hannover, 2016 (cit. on p. 2).
- [Wis08] WISE, F. W., A. CHONG, and W. H. RENNINGER: ‘High-energy femtosecond fiber lasers based on pulse propagation at normal dispersion’. *Laser & Photon. Rev.* (2008), vol. 2(1-2): pp. 58–73 (cit. on p. 15).
- [Zan01] ZANNI, M. T. and R. M. HOCHSTRASSER: ‘Two-dimensional infrared spectroscopy: a promising new method for the time resolution of structures’. *Current Opinion Struct. Biology* (2001), vol. 11: pp. 516–522 (cit. on p. 2).
- [Zaw10] ZAWILSKI, K. T., P. G. SCHUNEMANN, T. C. POLLAK, D. E. ZELMON, N. C. FERNELIUS, and F. KENNETH HOPKINS: ‘Growth and characterization of large  $\text{CdSiP}_2$  single crystals’. *J. Crystal Growth* (2010), vol. 312: pp. 1127–1132 (cit. on p. 115).
- [Zaw06] ZAWILSKI, K. T., S. D. SETZLER, P. G. SCHUNEMANN, and T. M. POLLAK: ‘Increasing the laser-induced damage threshold of single-crystal  $\text{ZnGeP}_2$ ’. *J. Opt. Soc. Am. B* (2006), vol. 23(11): pp. 2310–2316 (cit. on p. 68).

- 
- [Zel01] ZELMON, D. E., E. A. HANNING, and P. G. SCHUNEMANN: ‘Refractive-index measurements and Sellmeier coefficients for zinc germanium phosphide from 2 to 9  $\mu\text{m}$  with implications for phase matching in optical frequency-conversion devices’. *J. Opt. Soc. Am. B* (2001), vol. 18(9): pp. 1307–1310 (cit. on p. 115).
- [Zel10] ZELMON, D. E., J. J. LEE, K. M. CURRIN, J. M. NORTHRIDGE, and D. PERLOV: ‘Revisiting the optical properties of Nd doped yttrium orthovanadate’. *Appl. Optics* (2010), vol. 49(4): pp. 644–647 (cit. on p. 35).
- [Zel97] ZELMON, D. E., D. L. SMALL, and D. JUNDT: ‘Infrared corrected Sellmeier coefficients for congruently grown lithium niobate and 5 mol.% magnesium oxide-doped lithium niobate’. *J. Opt. Soc. Am. B* (1997), vol. 14(12): pp. 3319–3322 (cit. on p. 115).
- [Zel98] ZELMON, D. E., D. L. SMALL, and R. PAGE: ‘Refractive-index measurements of undoped yttrium aluminium garnet from 0.4 to 5.0  $\mu\text{m}$ ’. *Appl. Optics* (1998), vol. 37(21): pp. 4933–4935 (cit. on p. 35).
- [Zer73] ZERNIKE, F. and J. E. MIDWINTER: *Applied Nonlinear Optics*. Wiley, New York, 1973 (cit. on p. 61).
- [Zon97] ZONDY, J.-J., D. TOUAHRI, and O. ACEF: ‘Absolute value of the  $d_{36}$  nonlinear coefficient of  $\text{AgGaS}_2$ : prospect for a low-threshold doubly resonant oscillator-based 3:1 frequency divider’. *J. Opt. Soc. Am. B* (1997), vol. 14(10): pp. 2481–2497 (cit. on p. 115).



---

## List of Figures

---

1.1	Part of the electromagnetic spectrum ranging from the ultraviolet (UV) to the infrared (IR) radiation. Nowadays, conventional laser sources emitting in the visible to near-IR spectral region are more and more replaced by mid-IR laser sources. The short-wave infrared (SWIR) and, especially, the mid-wave (MWIR) and long-wave infrared (LWIR) radiation is interesting for a multitude of recently emerging applications. . . . .	1
3.1	(a) Electrical field $E(t)$ of an optical pulse with Gauss-shaped envelope $A(t)$ based on Equation (3.7) and (b) linear up-chirp on an optical pulse, which manifests itself in a linear variation of the instantaneous frequency. . . . .	10
3.2	Simulated dispersion of (a) standard passive fiber (similar to SMF-28e+: $d_{\text{core}} = 8.2 \mu\text{m}$ , NA 0.14) and (b) dispersion compensating fiber (similar to UHNA4: $d_{\text{core}} = 2.2 \mu\text{m}$ , NA 0.35). . . . .	11
3.3	Schematic evolution of the pulse duration, chirp, and dispersion during cavity propagation for different pulse regimes [Wis08]. . . . .	15
3.4	(a) Schematic energy level diagram with the most important transitions and (b) corresponding emission and absorption cross sections of holmium-doped silica fiber (digitized from [Sim13]). . . . .	18
3.5	Effective gain cross section of holmium-doped silica fiber at different inverted fractions $\Lambda$ as introduced in Equation (4.4). . . . .	18
3.6	Experimental setup of the holmium-doped fiber oscillator. SESAM: semiconductor saturable absorber mirror, PC: polarization controller, WDM: wavelength division multiplexer, PM: polarization maintaining, HDF: holmium-doped fiber, NDF: normal dispersive fiber. . . . .	20
3.7	(a) Experimental (black solid line) and simulated (red dotted line) optical spectrum of the ultrashort pulse oscillator and transmission of the narrow-band WDM measured with an optical spectrum analyzer with a resolution of $\Delta\lambda_{\text{res}} = 0.05 \text{ nm}$ . (b) Fourier-limited pulse duration based on the measured optical spectrum (black solid line) and simulated autocorrelation (red dashed line). . . . .	21
3.8	(a) Measured fundamental beat note and (b) radio-frequency comb up to 1 GHz measured with a RF spectrum analyzer. . . . .	22
3.9	(a) Oscilloscope trace of the measured pulse train emitted by the ultrashort pulse laser source. (b) RIN measurement of the Ho-doped fiber oscillator (black solid line), technical background noise (grey solid line), and shot noise limit (black dashed line). . . . .	23

3.10	Experimental Ho-doped fiber pre-amplifier setup. M: monitoring port, HDF: Ho-doped fiber, PC: polarization controller, PM: polarization maintaining, TDFA: Tm-doped fiber amplifier, WDM: wavelength division multiplexer, AOM: acousto-optic modulator. . . . .	24
3.11	(a) Average output power and corresponding pulse energy vs. the absorbed pump power (black circles). The linear fit (red dashed line) indicates a slope efficiency of 67%. Inset: Long-term measurement at a fixed output power of 500 mW over a time period of 3 h. (b) RIN measurement of the pre-amplifier (black solid line), technical background noise (grey solid line), and shot noise limit (black dashed line). . . . .	25
3.12	(a) Experimental (black solid lines) and simulated (red dashed lines) optical spectrum at different pulse energies and (b) corresponding autocorrelation traces. . . . .	26
3.13	(a) $M^2$ measurement at an average output power level of 500 mW: measured data (circles) and fitted caustic (solid lines) according to Equation (3.13). (b) Pointing stability measurement over a period of 5 min. . . . .	26
4.1	Emission (black) and absorption (red) cross section of various holmium-doped crystals, which are commonly used in laser systems with emission around 2 $\mu\text{m}$ , digitized from [Gol02; Koo12; Kwi09; Wal98]. Note that the ordinate is scaled according to the different cross section values. . . . .	34
4.2	(a) Schematic energy level diagram with the most important transitions and (b) the corresponding emission and absorption cross sections of Ho:YLF for $\vec{E} \parallel c$ (digitized from [Wal98]). . . . .	36
4.3	(a) Fluorescence spectrum of a 1.5 at. % doped Ho:YLF sample excited at a wavelength of 1940 nm and (b) effective gain cross section of Ho:YLF in the case of $\vec{E} \parallel c$ . . . . .	36
4.4	Normalized fluorescence decay in Ho:YLF at different excitation intensities. The black dotted line represents the literature value for the upper-state lifetime with 15 ms [Pay92; Wal98]. . . . .	38
4.5	Continuous wave pump absorption in 20 mm long Ho:YLF crystals at different wavelengths of 1890 nm and 1940 nm. The linear polarization has been orientated along the c-axis. The maximum pump power of 4 W corresponds to an intensity of 35 kW/cm <sup>2</sup> . . . . .	39
4.6	Single-pass small-signal gain in 20 mm long Ho:YLF crystals at different wavelengths of 1890 nm and 1940 nm: experimental data (circles) and numerical simulation (dotted lines). . . . .	40
4.7	Single-pass small-signal gain in 20 mm long Ho:YLF crystals at different wavelengths of 1890 nm and 1940 nm versus the crystal temperature: experimental data (circles) and linear fit (solid lines). . . . .	41

4.8	(a) Temperature profile of the pumped spot in the crystal at maximum pump power of 10 W with an on-axis maximum of about 40 °C. (b) Thermal lensing in an end-pumped Ho:YLF laser crystal depending on the absorbed pump power. The simulated values are based on the Ho:YLF thermo-mechanical properties as summarized in Table 4.1. . . . .	42
4.9	Experimental setup of the multipass amplifier system. AOM: acousto-optic modulator, TFP: thin-film polarizer, FR: Faraday rotator, PBS: polarization beam splitter, DC: dichroic mirror, $\lambda/2$ : half-wave plate. . . . .	43
4.10	(a) Measured output pulse energy as a function of the launched pump power for different pulse repetition frequencies between 10 kHz up to 20 MHz and (b) at fixed pump power of 7.5 W limited by the damage threshold at the lowest pulse repetition frequency of 10 kHz. . . . .	45
4.11	Simulation of different combinations of doping concentrations in a dual-stage amplifier (first stage/second stage) for a pulse repetition frequency of 100 kHz and a fixed maximum pump power of 18 W. The diagram shows the calculated pulse energy as a function of the used pump power in the first stage, while the remaining pump power is pumping the second stage. The numerical model is based on the final experimental setup considering the seed and pump properties as well as the Ho:YLF characteristics. . . . .	45
4.12	Measured autocorrelation traces (black circles) for different pulse repetition frequencies of (a) 50 kHz, (b) 100 kHz, (c) 500 kHz, and (d) 20 MHz at maximum achieved pulse energy assuming a Gauss-shaped pulse (red dotted line) as well as the calculated Fourier-limited pulse duration (black solid line) based on the corresponding optical spectrum (inset), respectively. . . . .	47
4.13	(a) Fundamental beat note of the 100 kHz amplified pulse train and (b) single pulse oscilloscope trace. . . . .	47
4.14	Long-term stability of the multipass amplifier at a pulse repetition frequency of 100 kHz. Inset: Corresponding far-field beam profile. . . . .	48
4.15	(a) $M^2$ measurement at an average power of 5 W: measured data (circles) and fitted caustic (solid lines) according to Equation (3.13). (b) Pointing stability measurement over a period of 5 min. . . . .	48
4.16	Experimental setup of the booster amplifier. DC: dichroic mirror, $\lambda/2$ : half-wave plate. . . . .	49
4.17	Detailed simulation results of the double crystal booster amplifier according to the input parameters from Table 4.3: (a) Simulated output pulse energy, maximum pulse fluence, and accumulated nonlinear phase (B-integral) in dependence on the focal beam waist radius of the pump and signal beam; (b) evolution of the pulse energy and the inverted fraction at steady-state within the two Ho:YLF crystals (gray areas) during beam propagation in the case of a signal and pump beam waist radius of 225 $\mu\text{m}$ (black solid lines). . . . .	52
4.18	(a) Numerical (red dashed line) and experimental (black solid line) results of the pulse energy with increasing seed pulse energy for different pulse repetition rates between 1 and 100 kHz. (b) Far-field beam profile of the booster amplifier output at an energy level of 1.2 mJ (1 kHz). . . . .	52

- 4.19 Measured autocorrelation traces (black circles) for different pulse repetition rates of (a) 1 kHz, (b) 10 kHz, and (c) 100 kHz at maximum achieved pulse energy assuming a Gauss-shaped pulse (red-dotted line) as well as the calculated Fourier-limited pulse duration (black solid line) based on the corresponding optical spectrum (inset, gray area), respectively. In addition, the simulated optical spectrum (inset, red dotted line) based on the seed optical input properties is presented. . . . . 54
- 5.1 Schematic photon energy diagram for the second-order nonlinear three-wave mixing process optical parametric amplification. A seeded signal wave (s) gets amplified at the expense of an annihilated pump photon (p). At the same time an idler photon (i) with new frequency at  $\omega_i = \omega_p - \omega_s$  is generated. 59
- 5.2 (a) Normalized parametric gain of a nonlinear optical crystal with propagation length  $z$  as a function of the accumulated phase mismatch  $\Delta kz$ . (b) Schematic evolution of the nonlinear parametric gain  $G$  seen by the seeded signal in an OPA as a function of the propagation length  $z$  for perfect phase-matching condition (blue), non-phase-matched case (red), and quasi-phase-matching (yellow). . . . . 61
- 5.3 (a) Definition of ordinary and extraordinary directions in birefringent crystals. (b) Type-I, angular phase-matching in a negative, uniaxial crystal with signal and idler being the ordinary beams, whereas the pump is the extraordinary beam. Phase-matching condition is fulfilled for beam propagation at an angle of  $\theta_m$  with respect to the principal axis Z. In this case the index ellipsoid of the extraordinary pump  $n_e(\omega_p, \theta_m)$  intersects the sphere of ordinary signal and idler  $n_o(\omega_s + \omega_i)$ . . . . . 62
- 5.4 (a) Nonlinear FOM ( $d_{\text{eff}}^2/n^3$ ) versus transparency range of common nonlinear optical crystals for the mid-infrared spectral range. (b) Absorption spectra in the mid-IR spectral range for CSP, GaAs, ZGP, and GaP (digitized from [Sch16]). . . . . 64
- 5.5 (a) Transmission of the ZGP crystal considering the anti-reflection coating as specified by the manufacturer and the intrinsic material absorption (inset, from [Pet99]). (b) Type-I phase-matching ( $o \rightarrow ee$ ) in ZGP pumped at a wavelength of 2.05  $\mu\text{m}$ . . . . . 65
- 5.6 (a) Experimental setup of the mid-IR OPG. OAP: off-axis parabolic mirror, TFP: thin-film polarizer, LPF: long-pass filter,  $\lambda/2$ : half-wave plate. (b) Calculated walk-off angle and aperture length in ZGP as a function of the phase-matching angle for a signal and idler wavelength of 3  $\mu\text{m}$  and 6.5  $\mu\text{m}$ , respectively. . . . . 67



5.7	2.05 $\mu\text{m}$ pumped optical parametric generation: mid-IR pulse energy (combined signal and idler) (a) in dependence on the pump intensity for a fixed phase-matching angle of $\theta = 53^\circ$ and (b) in dependence on the internal phase-matching angle for a fixed pump intensity of 17 GW/cm <sup>2</sup> . The inset compares the experimentally obtained center wavelengths at different phase-matching angles with the theoretical values calculated from Equations (5.9) and (5.10) taking into account the frequency dependent ordinary and extraordinary refractive indices of ZGP. . . . .	68
5.8	(a) Signal (blue) and (b) corresponding idler (red) spectra at different internal mode-matching angles in the ZGP-based OPG pumped with 3.8 $\mu\text{J}$ at a wavelength of 2.05 $\mu\text{m}$ . The transmission for the propagation through 1 m in the laboratory environment is shown in gray color (left axis). The latter has been calculated for a room temperature of 20 $^\circ\text{C}$ and a relative humidity of 20 % based on the data provided by the HITRAN database [HIT19]. . . . .	69
5.9	Experimental setup of the OPG/OPA tandem. OAP: off-axis parabolic mirror, TFP: thin-film polarizer, LPF: long-pass filter, BPF: band-pass filter, $\lambda/2$ : half-wave plate. . . . .	70
5.10	OPG signal spectrum set to a center wavelength of about 3 $\mu\text{m}$ (gray area) by proper adjustment of the phase-matching angle and seed spectrum filtered by a bandpass filter with FWHM transmission bandwidth of 60 nm. . . . .	71
5.11	(a) Signal (blue) and idler (red) pulse energy in dependence of the pump pulse energy. (b) Long-term stability measurement of the signal and idler radiation at maximum pulse energy. Inset: Corresponding beam profile of the signal (left) and idler (right) beam. . . . .	72
5.12	Evolution of the pump (black) and signal (blue) $1/e^2$ beam radius during propagation in the OPA stage. . . . .	73
5.13	Measured optical spectrum in dependence on the amplified pulse energy for (a) the signal and (b) the idler radiation. Furthermore, the transmission for the propagation through 1 m in the laboratory environment is shown. The latter has been calculated for a room temperature of 20 $^\circ\text{C}$ and a relative humidity of 20 % based on the data provided by the HITRAN database [HIT19]. . . . .	73
5.14	Measured pointing stability of (a) the signal at 3 $\mu\text{m}$ and (b) the idler at 6.5 $\mu\text{m}$ over a course of 5 min. . . . .	74
5.15	Measured autocorrelation of the (a) mid-IR signal at a wavelength of about 3 $\mu\text{m}$ and (b) idler at a wavelength of about 6.5 $\mu\text{m}$ . The inset shows the corresponding spectral distribution, respectively. $\lambda_0$ : wavelength calculated by the center of gravity method. . . . .	74

- 
- A.1 (a) Experimental setup of the holmium-doped fiber oscillator (b) in comparison with the corresponding numerical model. SA: saturable absorber, Circ.: circulator, WDM: wavelength division multiplexer, NPR: nonlinear polarization rotation, OC: output coupler, HDF: holmium-doped fiber, SESAM: semiconductor saturable absorber mirror. . . . . 112
- C.1 Experimental setup of the thulium-doped fiber MOPA. HR: high reflective, FBG: fiber Bragg grating, PR: partial reflective, MMPC: multimode pump combiner, TDF: thulium-doped fiber. . . . . 117
- C.2 (a) Optical output spectrum of the Tm: fiber MOPA system used for pumping the Ho:YLF crystals in the multipass amplifier at a power of 17.4 W. (b) Long-term stability of the 1939 nm pump source. . . . . 118

---

## List of Tables

---

4.1	Mechanical and spectroscopic properties of different holmium-doped crystals [Ada89; Agg05; Bre89; Cas75; Koo12; Lag05; Li11; Mil77; Pay92; Sha69; Wal98; Web03; Zel10; Zel98]. The saturation fluence has been calculated based on Equation (4.6) with the data from Figure 4.1 at the specified main emission wavelength. Note that the literature values for the nonlinear refractive index $n_2$ are only valid at the specified wavelength. However, for a rough comparison these values are sufficient as the dispersion of the refractive index from one frequency $\omega$ to its second harmonic $2\omega$ is barely 10 % [Ada92].	35
4.2	Measured excited-state fluorescence lifetime of different Ho-doped YLF crystal samples. . . . .	38
4.3	Input parameters used in the numerical analysis of a single-pass booster stage operating at a pulse repetition frequency of 1 kHz. . . . .	50
4.4	Summary of the measured pulse energy $E_p$ , spectral bandwidth $\Delta\lambda$ , and pulse duration $\tau_p$ for the amplification in the dual-crystal Ho:YLF amplifier at different pulse repetition rates $f_{\text{rep}}$ . . . . .	53
A.1	Summary of the calculated fiber properties ( $\beta_2$ and MFD) of the different fiber types used for modeling the fiber-based ultrashort pulse oscillator for a design wavelength of 2050 nm. . . . .	111
B.1	Mechanical and optical properties of different nonlinear optical crystals used in parametric conversion stages for the generation of mid-IR radiation (references see B.2). MC: Miller's correction [Mil64]. The $d_{\text{eff}}$ is calculated for an OPA process pumped at 2.05 $\mu\text{m}$ to generate 3 $\mu\text{m}$ signal radiation. The corresponding phase matching condition is given in brackets (type-I, type-II, or QPM). Note that transparency range for the nonlinear optical materials PPKTA, PPKTP, and PPLN is not covering the idler wavelength at $\sim 6.5 \mu\text{m}$ . (*) Phase-matching under given conditions not possible. . . . .	114
B.2	References for the nonlinear optical crystal properties from Table B.1. . . . .	115



## A Numerical model for the fiber-based MOPA

Numerical simulations, which were essential for the development of the fiber-based ultrashort pulse oscillator and amplifier system, were performed with the commercial software fiberdesk [Sch19]. It is numerically solving the nonlinear Schrödinger Equation 3.11, which is extended by additional nonlinear effects,

$$\begin{aligned}
 \frac{\partial A}{\partial z} = & \underbrace{-\frac{\alpha}{2}A}_{\text{losses}} + \underbrace{\int_{-\infty}^{\infty} \frac{g(\omega)}{2} \tilde{A}(\omega) e^{-i\omega T} d\omega}_{\text{gain}} + \underbrace{\sum_{n \geq 1} \beta_n \frac{i^{n+1}}{n!} \frac{\partial^n}{\partial T^n} A}_{\text{dispersion}} \\
 & + \underbrace{i\gamma}_{\text{SPM}} \cdot \left( \underbrace{1 + i\tau_{\text{shock}} \frac{\partial}{\partial T}}_{\text{self-steepening}} \right) \left( A(T) \underbrace{\int_{-\infty}^{\infty} R(\tau) |A(T-\tau)|^2 d\tau}_{\text{Raman-response}} \right).
 \end{aligned} \tag{A.1}$$

by the split-step Fourier method. The corresponding expressions for the Raman-response and self-steepening can be found in [Kib05]. Higher-order dispersion such as TOD can be neglected as the pulse duration was always  $> 100$  fs during one cavity round-trip. The split-step Fourier method is based on the assumption that in propagating the optical field over small distances, the various linear (dispersion and losses) and nonlinear effects act independently. In this case, an analytical solution can be found, when considering only linear effects in the frequency domain in a first step and only nonlinear in the time domain in a second step. In other words, each small propagation distance is solved in two steps, while continuously switching between frequency and time domain until the solution for the complete fiber length is calculated. As a laser resonator consists of multiple fiber sections and components each inducing different linear and nonlinear effects, the fiber-based ultrashort pulse oscillator was modeled according to the scheme depicted in Figure A.1.

**Table A.1:** Summary of the calculated fiber properties ( $\beta_2$  and MFD) of the different fiber types used for modeling the fiber-based ultrashort pulse oscillator for a design wavelength of 2050 nm.

Fiber type	$\beta_2$ [fs <sup>2</sup> /mm]	MFD [μm]
HDF	-95.7	10.32
PM1550	-94.4	13.46
SM2000	-103.7	13.8
SMF-28	-94.1	11.82
NDF	90	6.55

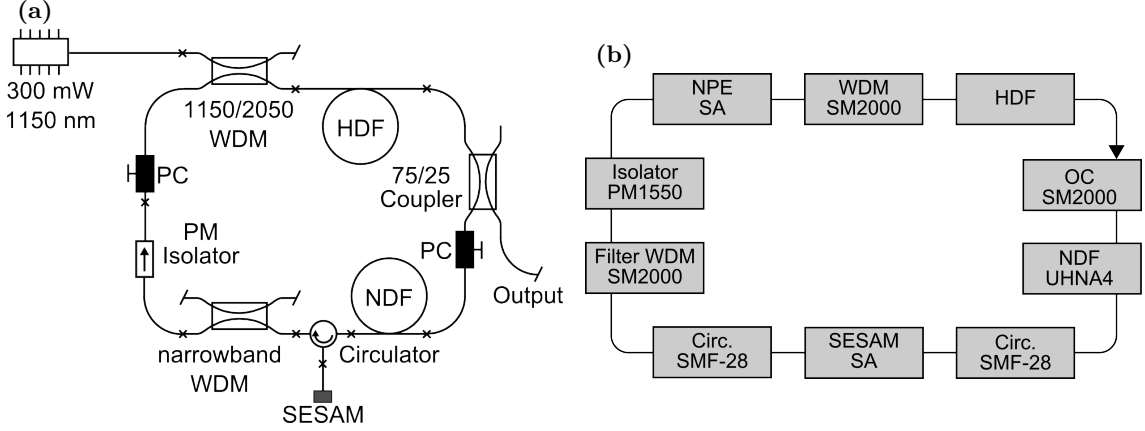


**Figure A.1:** (a) Experimental setup of the holmium-doped fiber oscillator (b) in comparison with the corresponding numerical model. SA: saturable absorber, Circ.: circulator, WDM: wavelength division multiplexer, NPR: nonlinear polarization rotation, OC: output coupler, HDF: holmium-doped fiber, SESAM: semiconductor saturable absorber mirror.

The simulation started with the 75/25 output coupler (0.78 m SM2000) followed by the propagation in the NDF (4.8 m UHNA4). In order to account for the increased propagation and bending losses in the NDF, a loss of 0.05/m was included, which corresponds to about 80% transmission for the 4.8 m of UHNA4 fiber in the cavity. The SESAM was embedded between two passive fiber sections originating from the circulator with a length of 0.85 m (SMF-28) each. The SESAM was modeled with a modulation depth of 12% and an unsaturable reflectivity of 70%. The saturation fluence was  $70 \mu\text{J}/\text{cm}^2$  and the focal spot diameter set to  $11.82 \mu\text{m}$  according to the butt-coupled passive fiber (SMF-28). The subsequent filter WDM and isolator were modeled with a passive fiber of 1.28 m (SM2000) and 0.5 m (PM1550), respectively. As the isolator is blocking one of the principal polarization axes, which is essential for the NPR mode-locking, a saturable absorber needed to be implemented after the isolator simulating the NPR mode-locking. The NPR was modeled as fast saturable absorber according to  $R(P) = R_0 + \Delta R - \Delta R / (1 + P^2/P_{\text{sat}})$  [Kär98] with an unsaturable reflectivity of  $R_0 = 50\%$ , a modulation depth of  $\Delta R = 20\%$ , and a saturation power of  $P_{\text{sat}} = 10 \text{ W}$ . Furthermore, the WDM, which was used to multiplex pump and signal radiation, was modeled with 0.6 m of passive fiber (SM2000). The final element in the simulation was the Ho-doped fiber with a length of 1.4 m. It was modeled with a gain coefficient of  $g_0 = 2.8/\text{m}$  exhibiting a Gaussian gain profile of 33 nm FWHM centered at 2052 nm to account for the spectral filter WDM transmission, while the gain follows  $g(E_p) = g_0 / (1 + E_p/E_{\text{sat}})$  with the saturation energy assumed to be  $E_{\text{sat}} = 0.3 \text{ nJ}$ . Simulations started from quantum noise until steady-state was reached. In Table A.1 the corresponding fiber parameters such as  $\beta_2$  and MFD at a given design wavelength of 2050 nm are summarized.

## B Nonlinear optical crystals for mid-infrared coherent sources

**Table B.1:** Mechanical and optical properties of different nonlinear optical crystals used in parametric conversion stages for the generation of mid-IR radiation (references see B.2). MC: Miller’s correction [Mil64]. The  $d_{\text{eff}}$  is calculated for an OPA process pumped at  $2.05\ \mu\text{m}$  to generate  $3\ \mu\text{m}$  signal radiation. The corresponding phase matching condition is given in brackets (type-I, type-II, or QPM). Note that transparency range for the nonlinear optical materials PPKTA, PPKTP, and PPLN is not covering the idler wavelength at  $\sim 6.5\ \mu\text{m}$ . (\*) Phase-matching under given conditions not possible.

Physical properties	orient. patt.	orient. patt.	ZnGeP <sub>2</sub>	CdSiP <sub>2</sub>	orient. patt.	GaSe
	GaAs	GaN			GaP	
acronym	OP-GaAs	OP-GaN	ZGP	CSP	OP-GaP	GaSe
space group	$\bar{4}3m$	P6 <sub>3</sub> mc	$\bar{4}2m$	$\bar{4}2m$	$\bar{4}3m$	$\bar{6}2m$
th. conductivity [W/(mK)]	46–52	260	36	13.6	100–110	16.2   c
refr. index at $3\ \mu\text{m}$	3.31	2.29(o)	3.13(o)	3.07(o)	3.02	2.73(o)
		2.28(e)	3.17(e)	3.02(e)		2.41(e)
transp. range [ $\mu\text{m}$ ]	0.9–17	0.36–7	0.74–12	0.52–9.5	0.57–12	0.62–20
bandgap [eV]	1.42–1.44	3.44	2–2.1	2.45	2.26(I)	2–2.1
$d_{\text{eff}}$ with MC [pm/V]	86 (QPM)	2.5 (QPM)	78.9 (I)	38 (I)	26.7 (QPM)	57.2 (I)
			80.3 (II)	74 (II)		40 (II)

Physical properties	AgGaSe <sub>2</sub>	AgGaS <sub>2</sub>	period. poled	period. poled	period. poled
			KTiOAsO <sub>4</sub>	KTiOPO <sub>4</sub>	LiNbO <sub>3</sub>
acronym	AGSe	AGS	PPKTA	PPKTP	PPLN
space group	$\bar{4}2m$	$\bar{4}2m$	mm2	mm2	3m
th. conductivity [W/(mK)]	1.1	1.5	1.8–2.1	2–3.3	3.9–4.6
refr. index at $3\ \mu\text{m}$	2.63(o)	2.41(o)	1.75( $\alpha$ )	1.70( $\alpha$ )	2.16(o)
	2.6(e)	2.36(e)	1.75( $\beta$ )	1.70( $\beta$ )	2.10(e)
			1.82( $\gamma$ )	1.78( $\gamma$ )	
transp. range [ $\mu\text{m}$ ]	0.71–19	0.47–13	0.35–5.2	0.35–4.5	0.4–5.5
bandgap [eV]	1.65–1.83	2.57–2.76	-	3.54–3.8	3.9–4.1
$d_{\text{eff}}$ with MC [pm/V]	26 (I)	7.97 (I)	8.9 (QPM*)	8.7 (QPM*)	13.4 (QPM)
	26.9 (II)	7.57 (II)			



**Table B.2:** References for the nonlinear optical crystal properties from Table B.1.

<b>Phys. properties</b>	<b>OP-GaAs</b>	<b>OP-GaN</b>	<b>ZGP</b>	<b>CSP</b>	<b>OP-GaP</b>	<b>GaSe</b>
acronym	-	-	-	-	-	-
space group	[Nik05]	[Bow14]	[Nik05]	[Sch16]	[Web03]	[Nik05]
th. conductivity	[Nik05; Sch05]	[Bow14]	[Bea94]	[Zaw10]	[Sch16; Web03]	[Nik05]
refr. index at 3 $\mu\text{m}$	[Ska03]	[Bar73]	[Zel01]	[Sch08]	[Bon65]	[Kat13]
transp. range	[Ska02]	[Rig18]	[Nik05]	[Pet09]	[Sor18]	[Nik05]
bandgap	[Nik05; Web03]	[Bow14]	[Nik05]	[Sch16]	[Sor18]	[Nik05]
$d_{\text{eff}}$ with MC	[Ska02]	[Irm16]	[Boy71]	[Sch08]	[Sho97]	[Nik05; Web03]

<b>Phys. properties</b>	<b>AGSe</b>	<b>AGS</b>	<b>PPKTA</b>	<b>PPKTP</b>	<b>PPLN</b>
acronym	-	-	-	-	-
space group	[Nik05]	[Nik05]	[Nik05]	[Nik05]	[Nik05]
th. conductivity	[Bea94]	[Bea94]	[Cas19]	[Nik05; Web03]	[Nik05]
refr. index at 3 $\mu\text{m}$	[Har97]	[Tak99]	[Fen95]	[Kat02]	[Zel97]
transp. range	[Nik05]	[Nik05]	[Nik05]	[Nik05; Web03]	[Nik05]
bandgap	[Nik05; Web03]	[Nik05; Web03]	-	[Nik05]	[Nik05]
$d_{\text{eff}}$ with MC	[Boy08]	[Zon97]	[Pac04]	[Pac04]	[Rob92; Sho97]



## C Thulium-fiber MOPA-based pump source

In this thesis, a self-developed Tm-fiber MOPA laser was used to pump the multipass amplifier as presented in Section 4.4. In the following, this pump laser system will be described.

The experimental setup of the Tm-fiber MOPA laser is schematically depicted in Figure C.1. The master oscillator consists of a 1.5 m long polarization maintaining thulium-doped fiber (PM-TSF-9/125, Nufern), which is pumped through a high reflective fiber Bragg grating. The pump source is a fiber-coupled diode laser (Princeton Lightwave) emitting at 1560 nm with an output power of 300 mW. An in-line polarizer (AFR) is used to force the laser to operate linearly polarized in only one principal axis. The cavity is terminated by a partial reflective fiber Bragg grating. Both high and partial reflective fiber Bragg gratings are designed for a narrowband operation at a wavelength of 1940 nm. At a launched pump power of about 250 mW into the Tm-doped fiber an output power of 16 mW at a wavelength of 1940 nm was achieved.

This generated signal was seeding a Tm-based amplifier. It was separated from the oscillator by a polarization maintaining isolator (AFR) to prevent instabilities due to back reflections. The low-power seed was amplified in a 3.3 m long polarization maintaining Tm-doped fiber (PM-TDF-10P/130, Nufern), which was cladding pumped via a multimode pump combiner by two identical high-power fiber-coupled laser diodes. The latter provided a maximum output power of 30 W each at an emission wavelength of 793 nm. Due to the expected large quantum defect in this pumping scheme and the resulting heat generated in the active fiber, the Tm-doped fiber was spooled on an aluminum block, which was actively temperature-stabilized by water cooling to room temperature.

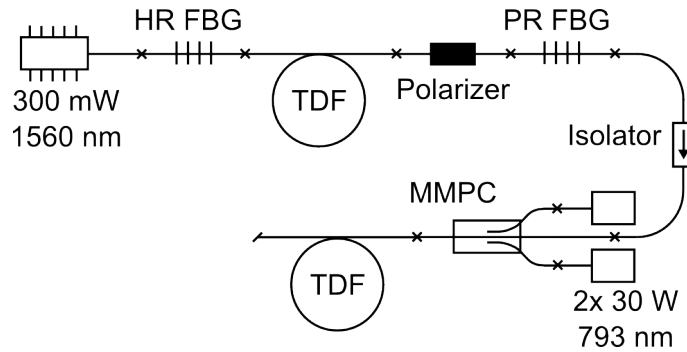


**Figure C.1:** Experimental setup of the thulium-doped fiber MOPA. HR: high reflective, FBG: fiber Bragg grating, PR: partial reflective, MMPC: multimode pump combiner, TDF: thulium-doped fiber.

The achieved output power of the amplifier stage was linearly scaling up to the highest value of 17.4 W with increasing pump power. This corresponds to an optical-to-optical efficiency of about 31 percent. The spectral characteristics are summarized in Figure C.2(a) showing the optical output spectrum at the maximum power level of 17.4 W. The amplified spontaneous emission, which has its maximum at a wavelength of 1975 nm, contains less than 5% of the output power. The polarization extinction ratio (PER) was measured to be  $> 20$  dB over the full output power tuning range. In Figure C.2(b) the long-term stability over a time period of 4 h is depicted, which was measured with a thermal power sensor. At an optical power level of 15.7 W the root mean square power noise amounts to  $< 0.44\%$ . Part of this power noise was originating from slow periodic fluctuations, which can be attributed to the water-based chiller cooling the pump diodes and the active thulium-doped fiber in the amplifier of the MOPA-based pump source.

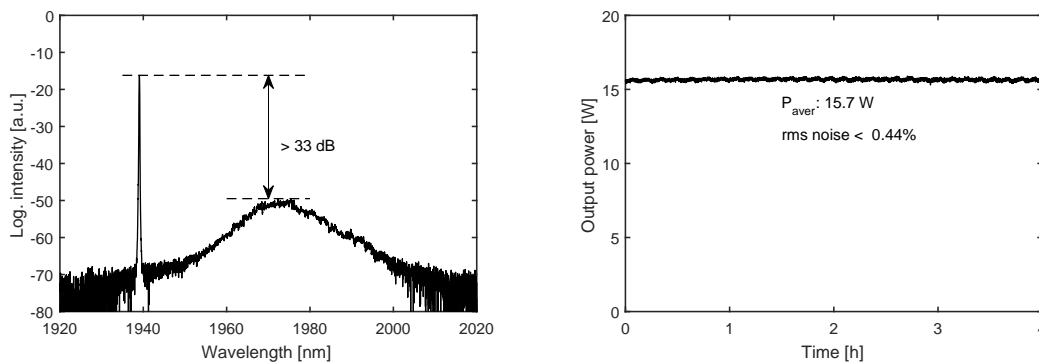


**Figure C.2:** (a) Optical output spectrum of the Tm: fiber MOPA system used for pumping the Ho:YLF crystals in the multipass amplifier at a power of 17.4 W. (b) Long-term stability of the 1939 nm pump source.

## Publications

### Peer reviewed publications

1. **Hinkelmann, Moritz**, MATTHIAS BAUDISCH, DIETER WANDT, UWE MORGNER, KEVIN ZAWILSKI, PETER SCHUNEMANN, INGO RIMKE, JÖRG NEUMANN, and DIETMAR KRACHT: ‘High-repetition rate, picosecond, mid-infrared laser systems based on nonlinear parametric processes in 2- $\mu\text{m}$ -pumped  $\text{ZnGeP}_2$ ’. *in preparation for publication in Optics Express* (2020), vol.
2. **Hinkelmann, Moritz**, BASTIAN SCHULZ, DIETER WANDT, UWE MORGNER, MAIK FREDE, JÖRG NEUMANN, and DIETMAR KRACHT: ‘Millijoule-level, kilohertz-rate, CPA-free linear amplifier for 2  $\mu\text{m}$  ultrashort laser pulses’. *Optics Letters* (2018), vol. 43(23): pp. 5857–5860.
3. **Hinkelmann, Moritz**, DIETER WANDT, UWE MORGNER, JÖRG NEUMANN, and DIETMAR KRACHT: ‘High repetition rate,  $\mu\text{J}$ -level, CPA-free ultrashort pulse multipass amplifier based on Ho:YLF’. *Optics Express* (2018), vol. 26(14): pp. 18125–18130.
4. **Hinkelmann, Moritz**, DIETER WANDT, UWE MORGNER, JÖRG NEUMANN, and DIETMAR KRACHT: ‘Mode-locked Ho-doped laser with subsequent diode-pumped amplifier in an all-fiber design operating at 2052 nm’. *Optics Express* (2017), vol. 25(17): pp. 20522–20529.
5. KELB, CHRISTIAN, RAIMUND ROTHER, ANNE-KATHRIN SCHULER, **Moritz Hinkelmann**, MAIK RAHLVES, OSWALD PRUCKER, CLAAS MÜLLER, JÜRGEN RÜHE, EDUARD REITHMEIER, and BERNHARD ROTH: ‘Manufacturing of embedded multimode waveguides by reactive lamination of cyclic olefin polymer and polymethylmethacrylate’. *Opt. Engineering* (2016), vol. 55(16): p. 037103.

### Conference contributions

1. BAUDISCH, MATTHIAS, **Moritz Hinkelmann**, DIETER WANDT, JÖRG NEUMANN, and INGO RIMKE: ‘2.4-18  $\mu\text{m}$  tunable, picosecond parametric source for the generation of narrowband,  $\mu\text{J}$ -level pulses with sub-8  $\text{cm}^{-1}$  spectral bandwidth and 20 kHz repetition rate’. *SPIE Photonics West, Nonlinear Frequency Generation and Conversion: Materials and Devices XIX*. 11264-17. 2020.
2. BAUDISCH, MATTHIAS, **Moritz Hinkelmann**, DIETER WANDT, KEVIN ZAWILSKI, PETER SCHUNEMANN, JÖRG NEUMANN, and INGO RIMKE: ‘2.5-12  $\mu\text{m}$  tunable, 2  $\mu\text{m}$  pumped,  $\text{ZnGeP}_2$  System for the generation of narrowband,  $\mu\text{J}$ -level pulses with sub-20  $\text{cm}^{-1}$  bandwidth’. *CLEO/Europe-EQEC*. IEEE, 2019: CF-7.3.

3. **Hinkelmann, Moritz**, BASTIAN SCHULZ, DIETER WANDT, UWE MORGNER, MAIK FREDE, JÖRG NEUMANN, and DIETMAR KRACHT: ‘CPA-free amplification of sub-10 ps pulses in Ho:YLF to the mJ-level at 2  $\mu\text{m}$  wavelength’. *Proc. SPIE 10896, Solid State Lasers XXVIII: Technology and Devices*. SPIE, 2019: 108960Q.
4. **Hinkelmann, Moritz**, DIETER WANDT, UWE MORGNER, JÖRG NEUMANN, and DIETMAR KRACHT: ‘Ultrafast mode-locked Ho-doped all-fiber laser operating at 2.05  $\mu\text{m}$ ’. *CLEO/Europe-EQEC*. IEEE, 2017.
5. **Hinkelmann, Moritz**, DIETER WANDT, UWE MORGNER, JÖRG NEUMANN, and DIETMAR KRACHT: ‘Ultrashort pulse CPA-free Ho:YLF linear amplifier’. *Proc. SPIE 10511, Solid State Lasers XXVII: Technology and Devices*. SPIE, 2018: p. 1051109.
6. **Hinkelmann, Moritz**, DIETER WANDT, UWE MORGNER, JÖRG NEUMANN, KEVIN ZAWILSKI, PETER SCHUNEMANN, and DIETMAR KRACHT: ‘High repetition rate, wavelength-tunable mid-IR source driven by ps-pulses from a Ho:YLF amplifier at 2  $\mu\text{m}$ ’. *CLEO/Europe-EQEC*. IEEE, 2019: CA–9.6.

## Curriculum Vitae

### Personal details

Name	Moritz Hinkelmann
Date of birth	07.11.1990
Place of birth	Lübeck
Nationality	German

### University education

10/2017 – present	PhD. student in Physics at the Leibniz Universität Hannover
04/2014 – 04/2016	Studies of Optical Technologies at the Leibniz Universität Hannover, degree: ‘Master of Science’ Master thesis title: ‘Amplification of Femtosecond Laser Pulses to mJ Level Based on Yb <sup>3+</sup> Thin-Disk Regenerative Amplifier’
09/2010 – 04/2014	Studies of Engineering Physics at the Technische Hochschule Lübeck, degree: ‘Bachelor of Science’ Bachelor thesis title: ‘Optically Pumped Semiconductor Laser with Vibration Desensitized Resonator’

### Education

06/2010	Abitur, Leibniz Gymnasium Bad Schwartau
---------	---

### Professional affiliations

05/2016 – present	Research scientist at Laser Zentrum Hannover e. V.
10/2015 – 03/2016	Engineering intern at Coherent Inc., Santa Clara, California
11/2014 – 07/2015	Scientific assistant in Laser Micromachining Group at Laser Zentrum Hannover e. V.
10/2013 – 03/2014	Scientific intern at Coherent LaserSystems GmbH & Co. KG, Lübeck





## Acknowledgements

Zunächst danke ich meinem Doktorvater Prof. Dr. Uwe Morgner für die Unterstützung in den letzten Jahren und die Betreuung während der Anfertigung dieser Dissertation.

Weiterer Dank gilt Prof. Dr. Detlev Ristau und Prof. Dr. Ömer Ilday für die Übernahme der Koreferate.

Dr. Dietmar Kracht und Dr. Jörg Neumann möchte ich für die interessante Aufgabenstellung danken sowie die Möglichkeit, diese Arbeit am Laser Zentrum Hannover e.V. durchzuführen. Die Abteilung Laserentwicklung am Laser Zentrum Hannover war mir zu jeder Zeit wie eine zweite Familie.

Neben all den Personen, die mich in dieser Abteilung auf dem Weg zur Promotion begleitet haben und deren Nennung hier den Rahmen sprengen würde, möchte ich zuletzt meinen Gruppenleiter Dr. Dieter Wandt hervorheben und ihm für die intensive Betreuung und Unterstützung danken.

